TECHNISCHE UNIVERSITÄT
MÜNCHEN
Physik Department
Lehrstuhl für Topologie Korrelierter Elektronensysteme

Preparation and Investigation of Intermetallic Magnetic Compounds with Disorder

Georg Alexander Benka, M. Sc.

Vollständiger Abdruck der von der
Fakultät der Physik der Technischen Universität München
zur Erlangung des akademischen Grades eines

Doktors der Naturwissenschaften (Dr. rer. nat.)

genehmigten Dissertation.

Vorsitzender:		Prof. Dr.	David Egger
Prüfer der Dissertation:	1.	Prof. Dr.	Christian Pfleiderer
	2.	Prof. Dr.	Sohyun Park

Die Dissertation wurde am 02.12.2020 an der Technischen Universität München
eingereicht und durch die Fakultät für Physik am 14.04.2021 angenommen.

Abstract

The preparation of large high-purity single crystals of ^{11}B-enriched CrB_x ($x = 1.90$, 2.00, 2.05, 2.10) and ErB_2 by optical float-zoning, as well as a series of polycrystalline Fe_xCr_{1-x} samples ($0 \leq x \leq 0.30$) by radio-frequency induction melting, is reported. Investigations of the nuclear structure by means of x-ray diffraction techniques as well as the bulk and transport properties with the help of measurements of the ac susceptibility, the magnetization, the electrical resistivity, and the specific heat at low temperatures in high magnetic fields are presented.

Kurzzusammenfassung

Die Herstellung von großen, hochreinen, mit ^{11}B angereicherten Einkristallen der Verbindung CrB_x ($x = 1.90$, 2.00, 2.05, 2.10) und der Verbindung ErB_2 mittels optischem Zonenschmelzen, sowie einer Reihe polykristalliner Fe_xCr_{1-x} Proben ($0 \leq x \leq 0.30$) mittels Radiofrequenz-Induktionsschmelzen wird berichtet. Untersuchungen der nuklearen Struktur mittels Röntgendiffraktionstechniken sowie der Volumen- und Transporteigenschaften mithilfe von Messungen der Wechselfeldsuszeptibilität, der Magnetisierung, des elektrischen Wiederstands, und der spezifischen Wärme bei niedrigen Temperaturen in hohen Magnetfeldern werden präsentiert.

Contents

CHAPTER 1

Magnetism and Disorder in Strongly Correlated Electron Systems

1.1 Motivation

In the field of experimental condensed matter physics, enormous scientific interest has been aroused in the last decades in exploring novel materials exhibiting exotic phenomena like high-T_c [1, 2] and unconventional superconductivity [3–5], quantum critical behaviour [6–8] often accompanied by non-Fermi liquid behaviour [9, 10], frustrated spin magnetism [11, 12], or complex spin textures with non-trivial topology [13–17]. The physics in these materials is governed by complex many-body interactions that cannot be described well in terms of non-interacting electrons and hence this class of materials is referred to as strongly correlated electron systems [18]. Consequently, their discovery brought about the need for novel theoretical approaches and revealed an enormous potential for technical applications.

Despite numerous experimental and theoretical endeavors, the underlying physics of strong electronic correlations are still far from being understood on a fundamental level. The complex interplay between electron-electron interactions, as well as spin, charge, orbital, and lattice degrees of freedom in those systems leads to a competition between distinct low-energy ground states mediated by strong fluctuations [19]. Frequently, this results in various forms of emergent order that can be driven through phase transitions by tuning the interaction strengths via experimental parameters such as temperature, magnetic field, pressure, or doping. Novel phases, for example unconventional superconductivity, are often discovered in the vicinity of quantum phase transitions, where conventional magnetic order can be suppressed to absolute zero temperature by a non-thermal tuning parameter [3].

Concerning the experimental investigation of strongly correlated electron systems, defects and disorder play an important role since many of the above mentioned phenomena are characterized by low-lying energy scales and are hence often sensitive to defects and sample impurities [4, 20–23]. Consequently, the exploration of systems with strong electronic correlations usually requires a well-controlled sample preparation, often aiming at large high-purity single crystals, containing the least possible amount of defects and impurities. In this context, the central subject of this thesis concerned the controlled preparation of the three intermetallic strongly correlated electron systems CrB_x, ErB_2, and $\mathrm{Fe}_{1-x}\mathrm{Cr}_x$ followed by the investigation of the interplay between magnetism and disorder in these compounds.

Two of the materials studied, namely CrB_x and ErB_2, are from the class of C32 diboride compounds, where the preparation of high-quality samples is very challenging due to the high melting points and vapour pressures of the starting elements as well as the high chemical reactivity of elemental B. A new high-pressure high-temperature optical floating zone furnace, which was set up and put into operation as a major part of this thesis, ultimately enabled the preparation of large single crystals of these refractory compounds.

Recent investigations on single-crystal CrB_2, carried out in the course of the Ph.D. theses of Andreas Bauer [24] and Alexander Regnat [25], identified CrB_2 as a weak itinerant antiferromagnet par excellence and suggested a complex magnetic structure with non-trivial topology that can be understood in terms of a $\mathbb{Z}_2$ vortex crystal. Furthermore, polarized neutron scattering measurements displayed a nuclear superstructure and a crystalline defect structure attributed to the ordering of B vacancies, indicating a subtle influence of disorder on the physical properties of CrB_2. As a consequence, single crystals of CrB_x with varying composition and therefore amounts of defects were carefully prepared and studied in order to shed light on the influence of disorder on the itinerant electronic properties of CrB_2, manifesting as a complex magnetic structure. The isostructural ErB_2 was reported to show a ferromagnetic transition and there are indications for more complex order in a rare-earth sibling compound, but conclusive research is scarce. The preparation of a high-quality single crystal of ErB_2 as part of this thesis enables the comprehensive investigation of this compound, in particular with regards to complex magnetic textures with non-trivial topology and the role of disorder paired with strong electronic correlations. With a view to the whole class of C32 diborides, the present study established a preparation route for rare-earth diborides in general, ultimately allowing for in-depth research on these elusive materials. The third material studied was polycrystalline $\mathrm{Fe}_{1-x}\mathrm{Cr}_x$, which originates by the isostructural substitution between the two archetypical itinerant elemental ferro- and antiferromagnets Fe and Cr. Displaying complex re-entrant spin glass behaviour while being regarded as a candidate for a quantum critical point, $\mathrm{Fe}_{1-x}\mathrm{Cr}_x$ is in particular interesting in the context of this thesis as it represents a well-studied model system for exploring the interplay between statistical disorder and the archetypical forms of itinerant magnetism.

Parts of the work reported below were conducted within the project "Single Crystal Growth of Metals with Complex Order", part of the DFG-funded research grant "Transregional Collaborative Research Center TRR80: From Electronic Correlations to Functionality", as well as the two ERC-funded research grants "Topological Spin Solitons for Information Technology" and "Extreme Quantum Matter in Solids".

1.2 Outline and Summary

The outline of the work reported below is as follows. Chap. 2 introduces the investigated materials CrB_x and ErB_2 from the class of C32 diborides as well as the re-entrant spin glass system $\mathrm{Fe}_x\mathrm{Cr}_{1-x}$, provides an overview on the physics in those materials, and motivates the work reported in this thesis.

Chap. 3 addresses the preparation and characterization of high-purity intermetallic compounds investigated in this thesis. Starting with an account on basic metallurgy and single crystal growth from the melt, a methodical description of preparation techniques ensues. This is followed by an introduction to the equipment and furnaces used, where the high-temperature high-pressure optical floating zone furnace is treated in detail. In particular, this furnace allowed the preparation of large single crystals of the diboride compounds CrB_x and ErB_2. The final paragraph of the chapter provides an overview of the sample characterization and measurements at low temperatures.

Chap. 4 reports studies of the influence of the boron portion on the low-temperature properties of CrB_x, motivated by a distinct defect structure and nuclear superstructure observed in neutron scattering on stoichiometric single-crystal CrB_2. These observations are reported in the Ph.D. thesis of Alexander Regnat [25] and have been attributed to the ordering of B vacancies. Four ^{11}B-enriched single crystals of CrB_x with the compositions $x = 1.90,\ 2.00,\ 2.05,\ 2.10$ were prepared in the high-pressure high-temperature optical floating zone furnace and the dependence of the lattice dimensions, the residual resistivity ratios (RRR), and the antiferromagnetic transition temperatures T_N on the starting composition are investigated by means of the electrical resistivity and specific heat. The lattice constants are in close agreement with the literature and are similar for all samples. In agreement with Refs. [24, 25, 31] our best samples show a RRR of about 30. The evolution of the RRR as a function of the composition x suggests that crystals with further increased B portion $x > 2.10$ may yield even higher RRR values. It is observed that samples with RRR $\gtrapprox 23$ display an antiferromagnetic transition temperature of $T_\mathrm{N} \approx 88.5\,\mathrm{K}$ and samples with RRR ≈ 11 display $T_\mathrm{N} < 88.5\,\mathrm{K}$. A reduced RRR is accompanied by decreased values of T_N.

Chap. 5 reports the preparation and investigation of a high-purity ^{11}B-enriched ErB_2 single crystal in the high-pressure high-temperature optical floating zone furnace. Detailed measurements of the susceptibility, magnetization, specific heat, and electrical resistivity at low temperatures under applied magnetic fields reveal a nontrivial magnetic state below $T_\mathrm{N} = 13.9\,\mathrm{K}$ with strong magnetocrystalline anisotropy between the easy in-plane directions $\langle 100\rangle \times \langle 210\rangle$ and the hard out-of-plane direction $\langle 001\rangle$, corroborated by a spin-flip transition at 4 K in a field of 11.8 T for field along the hard axis $\langle 001\rangle$. Our interpretation of the data points to a magnetic structure of an easy-plane antiferromagnet, characterized by strong ferromagnetic coupling within the easy plane $\langle 100\rangle \times \langle 210\rangle$ and weak antiferromagnetic coupling along the hard $\langle 001\rangle$ direction between alternating planes. This scenario is corroborated by indications for anisotropic spin fluctuations well above T_N in the bulk properties.

Chap. 6 reports investigations of polycrystalline $\mathrm{Fe}_x\mathrm{Cr}_{1-x}$ alloys in the concentration range $0 \leq x \leq 0.30$. Displaying behaviour reminiscent of quantum critical systems, the magnetic behaviour of $\mathrm{Fe}_x\mathrm{Cr}_{1-x}$ is tuned by the concentration x from antiferromagnetic to ferromagnetic, where a dome of re-entrant spin glass behaviour emerges at low temperatures in the intermediate concentration range. A comprehensive study of the magnetic phase diagram of $\mathrm{Fe}_x\mathrm{Cr}_{1-x}$, revealing indications for the existence of an additional novel precursor regime, is presented, and the evolution of the nature of the spin glass state over the concentration range is investigated with the help of the Mydosh parameter, a Vogel-Fulcher analysis, and power-law fits.

To conclude, Chap. 7 summarizes the reported work and provides an outlook on future studies.

CHAPTER 2

Introduction to CrB_x, ErB_2, and Fe_xCr_{1-x}

This chapter introduces the material systems investigated as part of this thesis and provides basic information about the physics observed in these systems. The chapter serves as a basis for defining the research problems and understanding of the work reported in subsequent chapters.

2.1 Introduction to the C32 Diboride Compounds

The investigation of complex ordering phenomena such as superconductivity or itinerant (anti-)ferromagnetism in materials with strong electronic correlations often stands and falls by the availability of high-purity single-crystal samples. One class of materials, where the lack of high-purity single-crystal samples frequently prevented detailed investigations, are the C32 diborides with structure formula MB_2, where M is a transition-metal or rare-earth element. These compounds crystallize in the hexagonal $P6/mmm$ structure (space group 191), as depicted in Fig. 2.1.

Those systems were first investigated due to their unique combination of properties such as high melting points, chemical and mechanical stability, and high thermal and electrical conductivity [26–28]. In recent years, the class of C32 diborides has come into focus of scientific interest due to a wide range of intriguing electronic and magnetic properties hosted by a high symmetry crystal structure comprising only two elements. Perhaps the most famous example is MgB_2 which was discovered in 2001 to be a conventional superconductor below a record-high temperature of 39 K [29]. Other examples reach from non-trivial antiferromagnetism in CrB_2 [30, 31], YbB_2 [32], and MnB_2 [33], over the rare-earth diborides TbB_2 [26, 34, 35], DyB_2 [26, 36], HoB_2 [26], ErB_2 [26], and TmB_2 [37], where ferromagnetic behaviour has been reported, to superconductivity in ZrB_2 [38] and in off-stoichiometric Nb_xB_2 ($0.67 \leq$

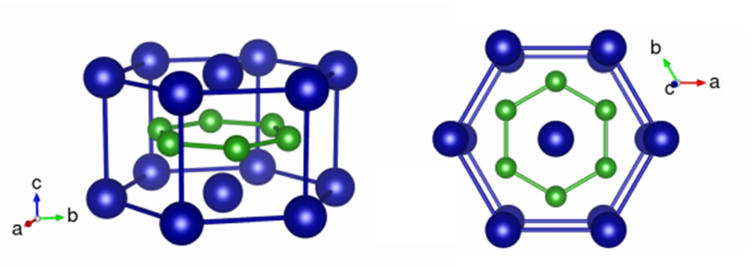

Figure 2.1: Depiction of the hexagonal $P6/mmm$ structure (space group 191) of the C32 diborides. Metal and B atoms are depicted in blue and green, respectively. Fig. from Ref. [25].

$x \leq 1.11$) [39]. The fact that the representatives of this material class crystallize in the same structure opens up further possibilities for investigations by tuning the physical properties, either by varying the stoichiometry of the system, e.g. in Nb_xB_2, or by doping the system with a third constituent. For example, early experiments indicated a decrease of the antiferromagnetic transition temperature in $V_xCr_{1-x}B_2$ for increasing V concentration x, followed by its disappearance around $x = 0.23$ [40]. This behaviour suggests a quantum critical point located around $x = 0.23$, where the antiferromagnetic order is suppressed by V doping as a non-thermal control parameter [6, 41].

Despite this variety of intriguing phenomena, many of the C32 diborides have not been explored in any detail yet. One of the main reasons for this lack of information is that the growth of phase pure single crystals of C32 diborides is very challenging. First, many compounds, in particular the rare-earth diborides, are reported to melt incongruently [42]. Second, the preparation from the melt requires very high temperatures of approximately 2000 °C and above. Third, the high vapor pressures of many of the starting elements can lead to considerable evaporation losses. Yet, high-purity single crystals are an essential prerequisite in order to clarify the nature of the wide range of ground states in the C32 diborides. Using a new high-pressure high-temperature optical floating zone furnace, large high-purity single crystals of the refractory diborides could be successfully prepared in the course of this thesis. The work reported below comprised the preparation of single crystals of congruently melting CrB_x with B portion $x = 1.90, 2.00, 2.05, 2.10$ as well as incongruently melting ErB_2 with stoichiometric composition. The following two sections separately introduce the two systems in detail and motivate the conducted research.

2.1.1 The Transition-Metal Diboride CrB_2

Being one of the known C32 diborides displaying antiferromagnetic order, the transition-metal diboride CrB_2 has been the subject of numerous experimental and theoretical research. Several theoretical studies addressed the band structure and hinted towards strong electronic correlations [43–47]. Early high-temperature susceptibility measurements on polycrystalline samples revealed a large negative Curie-Weiss temperature of $\Theta_{\mathrm{CW}} = 1550\,\mathrm{K}$ with a fluctuating moment of $\mu_{\mathrm{eff}} = 2.07\,\mu_{\mathrm{B}}$ implying antiferromagnetic interactions [48]. Later, NMR studies indicated an itinerant antiferromagnetic transition at $T_{\mathrm{N}} \approx 88\,\mathrm{K}$ [30], but were questioned in further NMR experiments which suggested that the order in $\mathrm{CrB_2}$ is intermediate between local-moment and itinerant magnetism [49, 50].

Several studies of the zero-field ac susceptibility consistently report a distinct maximum at $T_{\mathrm{N}} \approx 88\,\mathrm{K}$ and a Curie-Weiss behaviour at high temperatures with a large negative Curie-Weiss temperature [40, 48, 51–56]. Measurements of the specific heat exhibit a lambda anomaly at $T_{\mathrm{N}} \approx 88\,\mathrm{K}$, suggesting a second order phase transition to long-range order. Typical for d-metals with moderate correlations, a relatively large Sommerfeld coefficient of $\gamma = 13.6\,\mathrm{mJ\,mol^{-1}\,K^{-2}}$ is reported [51, 57]. Concerning the electrical transport properties, low residual resistivities indicate a good metallic state. With decreasing temperature, the resistivity drops monotonically and displays a pronounced kink at T_{N} [53, 57].

Since $\mathrm{CrB_2}$ is congruently melting, single crystals can be prepared from the melt in a straightforward approach provided that the high melting temperature of about 2200 °C can be reached. Bulk property measurements on single-crystal $\mathrm{CrB_2}$ corroborate previous results on polycrystalline samples, suggesting a combination of incommensurate and commensurate spin order [58]. Furthermore, the crystalline anisotropy was investigated by means of susceptibility, electrical resistivity, and magnetization measurements [54, 55].

Comprehensive studies of the low-temperature properties of $^{11}\mathrm{B}$-enriched high-quality single crystals were carried out during the Ph.D. theses of Andreas Bauer and Alexander Regnat [24, 25, 31]. Bulk property and transport measurements identified $\mathrm{CrB_2}$ as a weak itinerant antiferromagnet par excellence with a transition temperature of $T_{\mathrm{N}} \approx 88.5\,\mathrm{K}$. Above T_{N}, additional magnetic contributions observed in the specific heat point to very strong antiferromagnetic spin fluctuations. The large ratio of the Curie-Weiss to the antiferromangetic transition temperature $f = -\Theta_{\mathrm{CW}}/T_{\mathrm{N}} \approx 8.5$ implies strong geometric frustration. The dependence of the magnetic order on applied pressure showed that the electronic and magnetic properties of $\mathrm{CrB_2}$ are widely determined by the ratio of the hexagonal lattice constants and that the antiferromagnetic transition temperature T_{N} decreases with increasing pressure. Furthermore, the electrical resistivity under pressure displayed an abrupt drop at low temperatures strongly reminiscent of incipient superconductivity, as depicted in Fig. 2.2.

Based on neutron powder diffraction on $\mathrm{CrB_2}$ [40], the formation of a spin density wave due to Fermi surface nesting has been proposed [43]. Later neutron diffraction experiments on a single crystal disagreed with this scenario and suggested a cycloidal magnetic order with a small magnetic moment of $0.5\,\mu_{\mathrm{B}}$ on the basis of the available data [59]. Problematically, neutron scattering experiments on $\mathrm{CrB_2}$ comprising natural boron with isotope composition 80.1 % $^{11}\mathrm{B}$ and 19.9 % $^{10}\mathrm{B}$ are subject to a considerable reduction of the scattering signal due to the large neutron absorption of $^{10}\mathrm{B}$. Recently, spherical neutron polarimetry has been carried out on $^{11}\mathrm{B}$-enriched

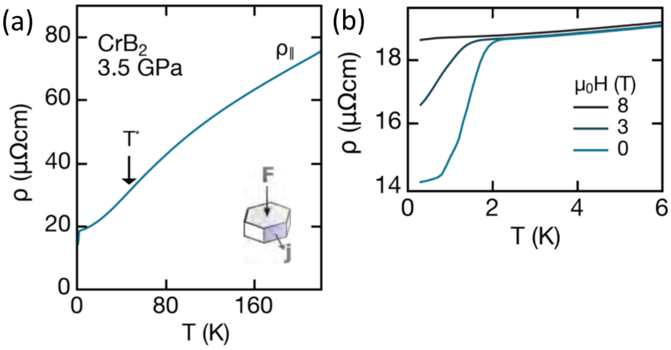

Figure 2.2: Electrical resistivity of CrB_2 under a pressure of 3.5 GPa. (a) Temperature dependence in zero field. (b) Detailed view of the low-temperature region in fields up to 8 T. Fig. adapted from Ref. [25].

single-crystal CrB_2, permitting detailed neutron scattering experiments. The reported data corroborate the cycloidal character of the long-range antiferromagnetic order in this compound [60].

As part of the Ph.D. thesis of Alexander Regnat [25], extensive neutron diffraction and scattering was carried on a ^{11}B-enriched high-quality CrB_2 single crystal, where bulk property investigations are summarized above. A refinement of the magnetic structure based on the neutron diffraction data confirmed the existence of incommensurate antiferromagnetic order as suggested in Ref. [59]. Moreover, the magnetic structure might be regarded as a $\mathbb{Z}_2$ vortex crystal with highly non-trivial topology [25]. In particular, the polarized neutron scattering data suggested the formation of a crystalline defect structure and a nuclear superstructure, observed through diffuse scattering. This is illustrated by Fig. 2.3, which depicts neutron scattering and single crystal diffraction data from Ref. [25]. Fig. 2.3(a) shows the non spin-flip channel of polarized neutron scattering on CrB_2 at 3.6 K. Diffuse streaks between the Bragg peaks point to the formation of a crystalline defect structure. Moreover, the investigation of a second sample revealed faint maxima of intensity along the lines of diffuse scattering, as depicted in Fig. 2.3(b). The diffuse streaks are corroborated by room temperature single crystal x-ray diffraction data, as shown in Fig. 2.3(c). According to Ref. [25], the diffuse streaks point to the formation of a crystalline defect structure and the additional faint maxima indicate a nuclear superstructure. Based on theoretical investigations suggesting vacancy ordering in elemental B as well as two-dimensional B layers [61–63], the ordering of B vacancies is proposed as a microscopic mechanism leading to the observed diffuse scattering in CrB_2.

The work presented as part of this thesis was motivated in particular by the observed diffuse scattering pointing to a defect structure and nuclear superstructure as well as the resistivity anomaly under pressure. The former observation is especially intriguing since a recent theoretical study suggested destabilization of the C32

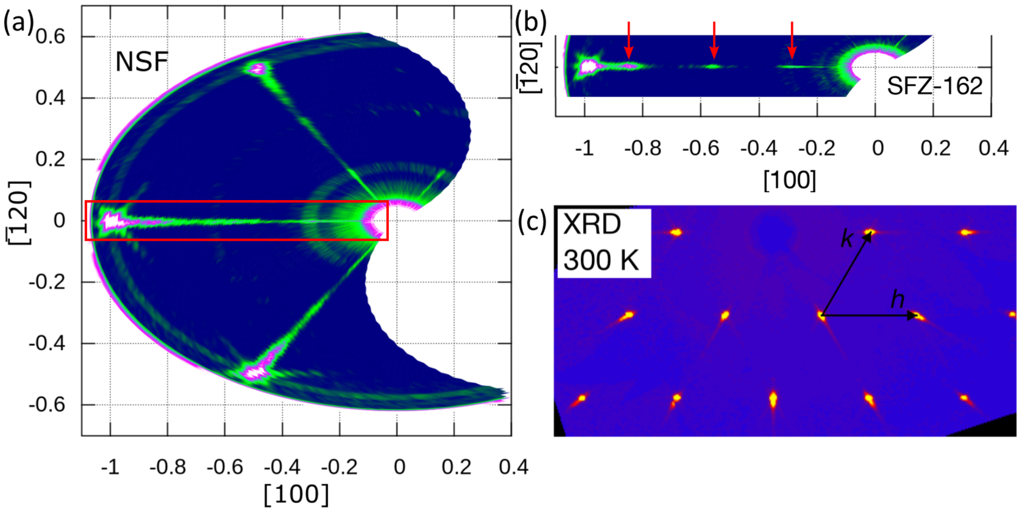

Figure 2.3: Diffuse scattering in the (hk0) reciprocal space plane of CrB_2. (a) Diffuse streaks (red box) between the Bragg peaks are observed in the non spin-flip channel of a polarized neutron scattering experiment at 3.6 K. (b) A second sample shows faint maxima of intensity (red arrows) along the diffuse streaks. (c) Single crystal x-ray diffraction at room temperature corroborates the neutron data. Fig. adapted from Ref. [25].

crystal structure in the whole class of C32 diborides by B vacancies [64]. Such a destabilization might in fact induce diffuse scattering, as observed in the neutron experiments reported.

As part of this thesis we investigated the influence of the boron portion x on the low-temperature properties of CrB_x in the light of the following two aspects. First, a variation of x is expected to change the amount of B vacancies, which were proposed to cause the defect structure and superstructure. Second, a variation of x is expected to change the lattice dimensions and thereby inducing similar effects as the application of pressure. We prepared four ^{11}B-enriched single crystals of congruently melting CrB_x with nominal compositions $x = 1.90, 2.00, 2.05, 2.10$ with the optical floating zone technique in the high-pressure high-temperature optical floating zone furnace and investigated their low-temperature properties. The work on CrB_x is reported in Chap. 4.

2.1.2 The Rare-Earth Diboride ErB_2

Another C32 diboride investigated as part of this thesis is ErB_2, which belongs to the group of rare-earth diborides together with TbB_2, TmB_2, DyB_2, and HoB_2, in which ferromagnetic order has been reported. Presumably due to the fact that these compounds melt incongruently, detailed studies are scarce and limited to polycrystalline samples often comprising small amounts of parasitic phases. Early investigations report ferromagnetic behaviour in TbB_2, DyB_2, HoB_2, and ErB_2 below temperatures of 151 K, 55 K, 15 K, and 16 K, respectively [26]. Furthermore, TbB_2 was investigated by means of neutron diffraction suggesting more complex magnetic order below the transition temperature [34, 65]. In the last decade, a two-step preparation route for improved polycrystalline samples, involving high-temperature high-pressure elemental synthesis followed by argon annealing has been reported [66]. Samples prepared with this method and other solid state synthesis techniques have been investigated mainly by means of calorimetric techniques. Specific heat measurements on TbB_2 displayed a broad Schottky anomaly near 100 K and a sharp peak at 143.3 K in agreement with ferromagnetic order [35]. In DyB_2, two anomalies at 47.8 K and 178.8 K were observed in the specific heat, the former was interpreted as a ferromagnetic transition [36].

The thermal expansion near the phase transition was studied on polycrystalline samples of TbB_2, TmB_2 DyB_2, HoB_2, and ErB_2, revealing anomalies in the vicinity of the ferromagnetic transition temperatures in agreement with the specific heat [67, 68]. Moreover, the electrical resistivity of polycrystalline samples of TmB_2, HoB_2, and ErB_2 indicates magnetic ordering temperatures of 7.5 K, 9 K, and 13.8 K, respectively [69]. More detailed studies are reported for polycrystalline TmB_2, where measurements of the susceptibility, magnetization, and specific heat combined with electronic structure calculations report long-range ferromagnetic order below 7.2 K and an effective magnetic moment of $\mu_{\text{eff}} = 7.49\,\mu_{\text{B}}/\text{f.u.}$ [37].

In contrast to the congruently melting CrB_2, ErB_2 melts incongruently and therefore it is very challenging to prepare high-quality phase pure single crystals. Yet, TmB_2 and ErB_2 have been prepared with a flux technique [70], but there are no reports of investigations on single-crystal samples in the literature.

Work on ErB_2 in the course of this thesis was motivated by the wide range of open questions in the group of rare-earth diborides, concerning the electronic and magnetic structure, the origin and character of the magnetic order, and the role of geometric frustration. In particular, regarding the whole series of rare-earth diborides, it is intriguing that YbB_2 hosts antiferromagnetic order [32], whereas the other representatives of this series are reported to order ferromagnetically. Therefore, exploring the whole group of rare-earth diborides by means of isostructural substitution and doping allows for tracking the evolution from ferromagnetic to antiferromagnetic behaviour, thereby yielding a deeper understanding of their physical and metallurgical properties. Both the fact that the magnetic structure of isostructural CrB_2 in the literature is described as incommensurate spin-density wave [25] and that neutron diffraction points to a more complex magnetic structure in the sibling rare-earth diboride TbB_2 [34, 65], raises the questions whether ErB_2 might host complex magnetic textures and to what degree disorder influences the physical properties.

To address these scientific problems, we prepared a high-purity ErB_2 single crystal with the optical floating zone technique in the high-pressure high-temperature optical floating zone furnace and present detailed investigations of the ac susceptibility, magnetization, specific heat, and electrical resistivity at low temperatures under applied magnetic fields. The work on ErB_2 is reported in Chap. 5.

2.2 Introduction to the Reentrant Spin Glass $\mathrm{Fe}_x\mathrm{Cr}_{1-x}$

The unique characteristic of Cr is the itinerant spin-density wave order below $T_\mathrm{N} = 311\,\mathrm{K}$ which establishes this element as the archetypical itinerant antiferromagnet. [71, 72]. Interestingly, Cr shares its body-centered cubic crystal structure $Im\bar{3}m$ with the archetypical itinerant ferromagnet α-Fe and all compositions of $\mathrm{Fe}_x\mathrm{Cr}_{1-x}$ at the melting temperature [42]. Consequently, the Cr–Fe system offers the possibility to study the interplay between these fundamental forms of magnetic order under isostructural substitution.

In particular $\mathrm{Fe}_x\mathrm{Cr}_{1-x}$ alloys in the range $0 \leq x \leq 0.30$ are of scientific interest due to two observations. First, starting at $x = 0$ in elemental Cr and increasing the iron concentration x in small steps leads to a gradual decrease of the antiferromagnetic transition temperature T_N until it disappears at $x \approx 0.15$. In the vicinity of this concentration, a ferromagnetic transition temperature T_C emerges which increases gradually with x. Second, spin glass behaviour (introduced in Sec. 2.2.2) is observed at low temperatures in the intermediate concentration range around $x = 0.15$ where T_N and T_C are at their lowest values. This overall behaviour is reminiscent of quantum critical systems under pressure, where the suppression of long-range magnetic order towards zero temperature is often accompanied by the emergence of a dome hosting a novel phase that covers the quantum critical point [6, 10, 41, 73]. Such a scenario is depicted in Fig. 2.4(a), which shows the schematic phase diagram of a system including a quantum critical point. For comparison, Fig. 2.4(b) depicts the phase diagram of $\mathrm{Fe}_x\mathrm{Cr}_{1-x}$ including the data from Refs. [74–76]. In $\mathrm{Fe}_x\mathrm{Cr}_{1-x}$, the putative quantum critical point is located between the antiferromagnetic and ferromagnetic phases and is surrounded by spin glass behaviour. As a control parameter, increasing the Fe content x suppresses the antiferromagnetic transition temperature T_N until spin-glass behaviour emerges and covers the putative quantum critical point. In particular, $\mathrm{Fe}_x\mathrm{Cr}_{1-x}$ enables the investigation of a system comprising two archetypical magnetic properties with complex spin glass behaviour in the vicinity of a putative quantum critical point.

2.2.1 State of the Art in $\mathrm{Fe}_x\mathrm{Cr}_{1-x}$

The $\mathrm{Fe}_x\mathrm{Cr}_{1-x}$ system crystallizes over the whole composition range in the body-centered cubic structure $Im\bar{3}m$ (space group 229), which is adopted by both elemental Cr and α-Fe. However, within the investigated concentration range $0.05 \leq x \leq 0.30$, an exsolution of the compound into two phases upon cooling is reported at temperatures of $\approx 350\,°\mathrm{C}$ and $\approx 700\,°\mathrm{C}$ for concentrations of $x = 0.05$ and $x = 0.30$, respectively [42]. Doping of Cr with Fe also leads to a decrease of the unit cell volume and hence corresponds to the application of hydrostatic pressure [77].

With decreasing temperature, elemental chromium exhibits transverse spin-density wave order below a Néel temperature $T_\mathrm{N} = 311$ K and longitudinal spin-density wave order below $T_\mathrm{SF} = 123$ K [71]. The longitudinal spin-density wave order becomes commensurate under substitutional doping with iron at $x = 0.02$ and for $0.04 < x$,

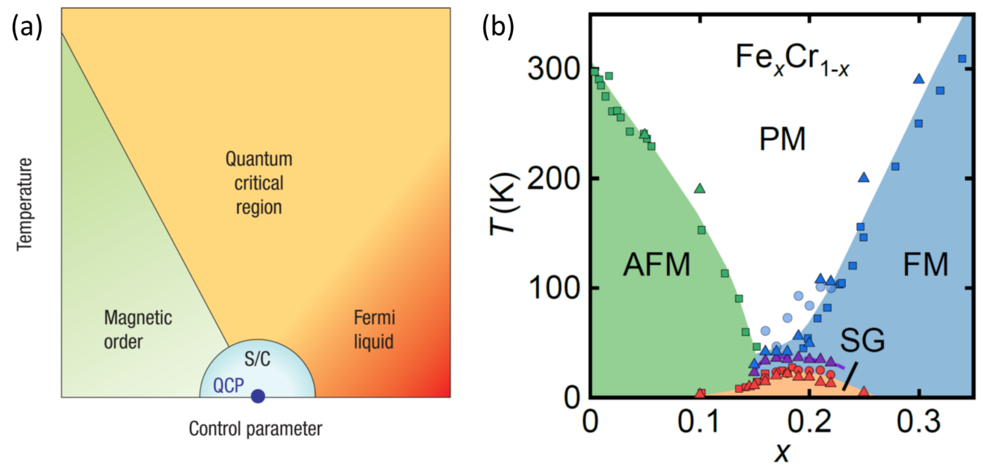

Figure 2.4: Phase diagram of a system including a quantum critical point and phase diagram of Fe_xCr_{1-x}. (a) Schematic phase diagram of a system including a quantum critical point. By tuning a control parameter, magnetic order can be suppressed with the ordering temperature decreasing to zero at a quantum critical point (QCP), often accompanied by the emergence of a dome of a novel phase, e.g. superconductivity (S/C). Fig. from Ref. [41]. (b) Phase diagram of Fe_xCr_{1-x} including data from bulk property and neutron depolarization measurements as well as data from Refs. [74–76]. We find evidence for four different regimes, namely antiferromagnetic (AFM, green), ferromagnetic (FM, blue), spin glass (SG, red), and a precursor regime (purple line). By tuning the Fe concentration x, T_N decreases towards zero temperature until a dome of spin glass (SG) behaviour emerges.

only commensurate antiferromagnetic order is observed [74, 78, 79]. With increasing x, the Néel temperature decreases and vanishes around $x \approx 0.15$, as determined by means of neutron scattering [74, 78, 80], magnetometry [79], and specific heat [81] measurements.

With further increasing x, a putative lack of long-range magnetic order was reported for intermediate concentrations [80]. This is followed by the onset of ferromagnetic order at $x \approx 0.18$ with an increase of the Curie temperature up to $T_C = 1041$ K in pure α-iron [75, 76, 82–85]. For concentrations in the intermediate range $0.14 \lessapprox x \lessapprox 0.19$, spin glass behavior is observed at low temperatures in bulk property and neutron measurements [74–76, 79, 85, 86]. Moreover, bulk property investigations reveal superparamagnetic behavior in the composition range $0.20 \leq x \leq 0.29$ [83] similar to the Au-Fe system [87] and from $0.09 \leq x \leq 0.23$ mictomagnetic behaviour[1] with a gradual change to ferromagnetism was reported [89].

A recent study by Säubert [90] applied neutron spin-echo techniques to directly access the dynamics of the spin relaxation in $\mathrm{Fe}_x\mathrm{Cr}_{1-x}$ on the samples $x = 0.145, 0.175, 0.21$ from Shapiro [85] and Motoya [91]. Fitting with stretched exponential functions yielded a broad distribution of relaxation times which suggests the presence of differently sized clusters and single spins in $\mathrm{Fe}_x\mathrm{Cr}_{1-x}$, matching previous assumptions based on neutron and bulk investigations [74–76, 80, 85]. At the same time, Säubert measured the magnetic transition temperatures with neutron diffraction and surprisingly finds no antiferromagnetic transition but ferromagnetic intensity for $x = 0.145$ as well as a ferromagnetic transition for $x = 0.175$, in contrast to previous investigations.

Despite $\mathrm{Fe}_x\mathrm{Cr}_{1-x}$ enables the investigation of a metallic spin glass emerging at the border of both itinerant antiferromagnetic and ferromagnetic order, comprehensive studies addressing the characterization of the spin-glass state, in particular by means of ac susceptibility measurements, are lacking.

In this thesis polycrystalline samples of $\mathrm{Fe}_x\mathrm{Cr}_{1-x}$ in the concentration range $0.05 \leq x \leq 0.30$, i.e., from antiferromagnetic doped chromium well into the ferromagnetically ordered state of doped iron, were investigated. Overall, the compositional phase diagram inferred from magnetization and ac susceptibility data is in good agreement with previous reports [74–76]. However, a novel crossover phenomenon preceding the onset of spin-glass behavior is observed in the imaginary part of the ac susceptibility. The spin-glass state is characterized by analysis of ac susceptibility data recorded at different excitation frequencies by means of the Mydosh parameter, power-law fits, and a Vogel–Fulcher ansatz establishing a crossover from cluster-glass to superparamagnetic behavior with increasing x. Neutron depolarization measurements provide microscopic evidence for this evolution, indicating an increase of the size of ferromagnetic clusters with x. The work on $\mathrm{Fe}_x\mathrm{Cr}_{1-x}$ is reported in Chap. 6.

2.2.2 Complex Magnetic Disorder in Spin Glasses

Spin glasses are complex magnetic systems that are characterized by randomness in the site occupancy of magnetic moments, competing interactions, and frustration. This leads to a collective freezing of spins into a metastable and irreversible state below a certain freezing temperature T_g. This section will give a brief introduction on the topic following Refs. [92–95]. The term "spin glass" derives from the structural freezing mechanism of magnetic moments, which is observed analogously for atoms in glass transitions. Fig. 2.5(a) illustrates the similarities between a glass and a spin glass. A crystal is characterized by a long range order of atoms, which is absent in a glass. Similarly, a ferromagnet exhibits long range order of magnetic moments, while in a spin glass, the latter are frozen in a random configuration.

The classical physical realization of a spin glass is a nonmagnetic host in which few magnetic impurities are randomly distributed on the lattice sites. The random dis-

---

[1] In mictomagnetic materials, the virgin magnetic curves recorded in magnetization measurements as a function of field lie outside of the hysteresis loops recorded when starting from high field [88].

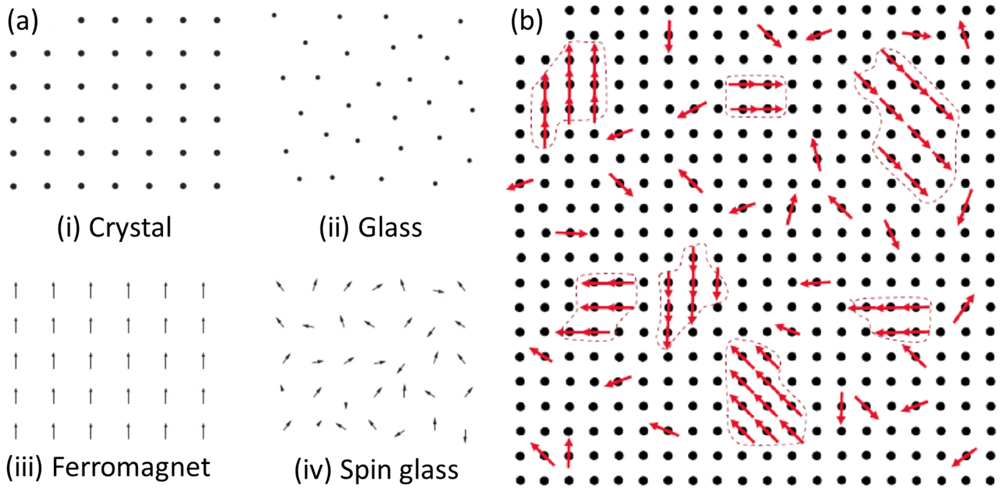

Figure 2.5: Schematic illustration of a spin glass in two dimensions. (a) Illustration of the similarities between a (i) crystal compared to a (ii) glass and a (iii) ferromagnet compared to a (iv) spin glass. (b) Illustration of a cluster glass in two dimensions. The red arrows represent magnetic moments in a nonmagnetic square lattice. Fig. from Ref. [95].

tance between the magnetic moments leads to mixed magnetic interactions, mainly mediated by the RKKY (Ruderman–Kittel–Kasuya–Yosida) interaction. The latter oscillates with the distance of the moments between ferromagnetic and antiferromagnetic coupling, as depicted in Fig. 2.6(a). The various resulting interactions compete with each other, often leading to magnetic frustration. Such a scenario is illustrated in Fig. 2.6(b), which shows four magnetic moments with coupling constants J_{12}, J_{23}, J_{34}, and J_{41} between moment one and two, two and three, three and four, and four and one, respectively. In this case, the coupling constant J_{34} is positive, favouring ferromagnetic coupling between moment three and four, while the coupling constant J_{41} is negative, favouring antiferromagnetic coupling between moment one and four. This leads to the magnetic frustration of the magnetic moment number four, indicated by the question mark symbol. On the scale of a whole system, the magnetic frustration of several magnetic moments leads to a multitude ground states which are very similar in their energy. A resulting energy landscape is schematically depicted in one dimension in Fig. 2.7. When lowering the temperature, the system will randomly choose one of these energetically very similar ground states. Hence, the freezing in a certain random configuration below T_g, with neither ferromagnetic nor antiferromagnetic long-range order, is observed. Such a system with a perfectly random distribution of magnetic moments is also called a canonical spin glass. At higher impurity concentrations, there is a greater chance that an impurity is nearest or second nearest-neighbour to another impurity. Consequently, this may lead to the formation of clusters of magnetic moments, which are internally ferromagnetically or antiferromagnetically ordered. Such a cluster glass is depicted in Fig. 2.5(b), where several ferromagnetic clusters and single impurities are present. Further increasing the number of impurities beyond the percolation limit usually leads to long-range magnetic order. The so-called reentrant spin glass may occur for concentrations around the percolation limit. This means that the spin glass state is entered from a previously ordered phase when lowering the temperature, which is the case for some concentrations of the investigated $\mathrm{Fe}_x\mathrm{Cr}_{1-x}$ system.

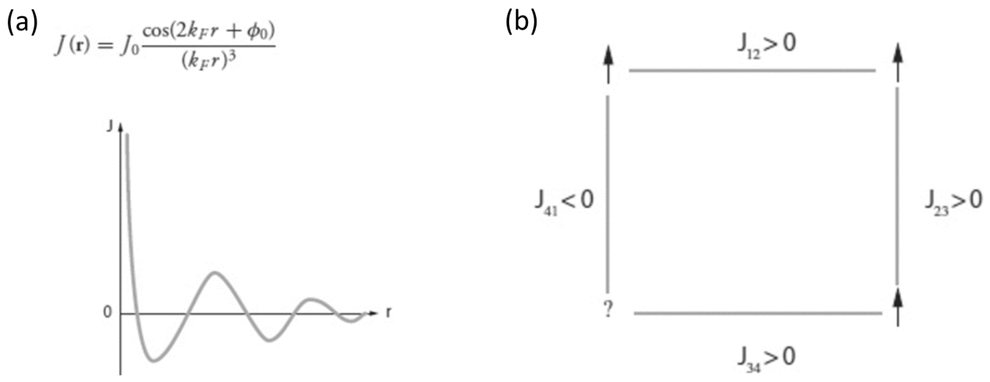

Figure 2.6: Illustration of the RKKY interaction and magnetic frustration. (a) Coupling constant of the RKKY interaction is oscillating with the distance between magnetic moments. (b) Emergence of magnetic frustration between four magnetic moments. Fig. from Ref. [92].

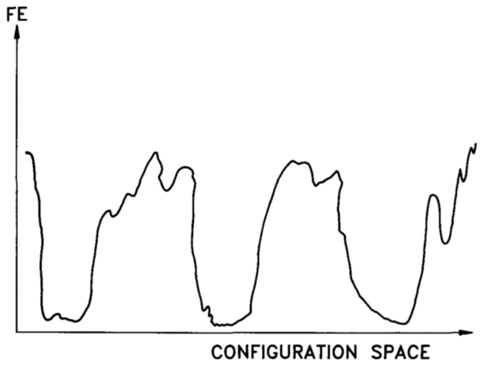

Figure 2.7: Schematic depiction of the energy landscape in a spin glass. Upon lowering the temperature, the system randomly freezes in one of the multitude of energetically similar ground states. Fig. from Ref. [93].

Experimentally, the first spin glasses were realized by doping magnetic moments into a nonmagnetic metallic host, also referred to as dilute magnetic alloys. These materials are canonical spin glasses and prominent examples include $\mathrm{Fe}_x\mathrm{Au}_{1-x}$ [87]

and $\mathrm{Mn}_x\mathrm{Cu}_{1-x}$ [96]. Today, a large number of material classes is known to show spin glass behaviour [95], for example nanoparticle systems [97, 98], uranium and cerium based heavy-fermion systems [99, 100], oxide compounds [101, 102], and insulators [103]. Spin glass behaviour can be identified by four experimental properties [95]: (i) a cusp in the ac susceptibility whose temperature T_g is shifting with frequency, (ii) a branching between the zero-field-cooled and field-cooled magnetization below approximately T_g, (iii) a specific heat without a discontinuity or cusp, and (iv) time and waiting time dependencies.

CHAPTER 3

Preparation and Characterization of High-Purity Intermetallic Compounds

A central part of this thesis concerned the preparation and characterization of metallic bulk samples and single crystals of highest achievable quality. In this chapter, we introduce single crystal growth and summarize the techniques and equipment of sample preparation and characterization.

The scientific projects pursued in this thesis were born out of the complex metallurgy exhibited by many investigated materials posing big challenges in the preparation. This issue is illustrated in Sec. 3.1 by an introduction to single crystal growth and basic metallurgy in the context of growing crystals from the molten state. The next section, Sec. 3.2, comprises a methodological description of the techniques of sample preparation applied in this thesis. Sec. 3.3 focusses on the technical aspects of sample preparation and introduces the furnaces and equipment. The high-temperature and high-pressure floating zone furnace which was set up and put into operation in the course of this thesis is described in Sec. 3.3.2. Finally, Sec. 3.4 provides an overview of the sample characterization and measurement techniques at low temperatures, notably methods of x-ray powder and Laue diffraction, magnetization and ac susceptibility, specific heat, as well as measurements of the electrical transport properties.

3.1 Introduction to Single Crystal Growth and Metallurgy

Since the middle of the 20th century, the growth of single crystals gained enormous importance in both technical applications and academic research. In an ideal single crystal the building blocks (atoms, ions, molecules) are periodically ordered in a three-dimensional arrangement throughout the whole volume without any disorder or grain boundaries. In particular, an ideal single crystal consists of only one crystalline grain. In comparison, materials which consist of a significant amount of small single crystals, separated by grain boundaries, are referred to as polycrystalline. These differences are illustrated schematically for two dimensions in Fig. 3.1.

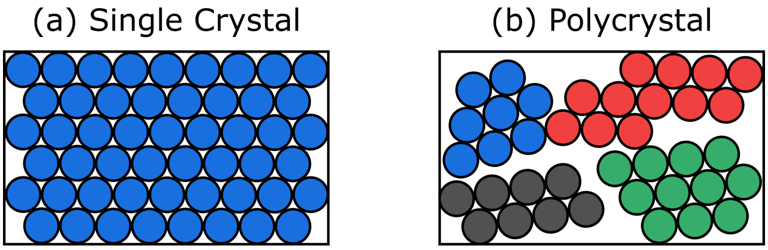

Figure 3.1: Illustration of the difference between a single-crystal and a polycrystalline material in two dimensions. The volume of the sample is represented by the black box, the atoms by spheres. (a) A single crystal, here with hexagonal lattice, is periodic across the whole specimen. (b) A polycrystalline material, here consisting of four grains coloured in blue, red, grey, and green, is periodic across each grain, but not across the entire specimen.

For a broad range of applications, single crystals are required because of two distinct features. First, real single crystals possess effectively no grain boundaries as compared to a polycrystalline material of the same purity. Since grain boundaries can act as impediments and affect the intrinsic physical properties, the quality of a single-crystal sample is most often superior to a polycrystalline sample when considered from a researchers point of view. The second important feature of single crystals is the possibility to measure properties with respect to crystallographic directions, i.e. directions of high symmetry. Many materials display big differences in physical properties with respect to crystallographic directions. Overall, single crystals are a necessity when exploring novel materials in basic research and identifying promising candidates for technological applications.

By far the most important example in the context of technology may be the field of semiconductor electronics where large single crystals are an indispensable prerequisite. Other widespread applications may be their use as detector materials in radiation and particle physics [104, 105] as well as in laser technology [106]. On the other hand, basic research is concerned with the investigation of materials properties on a fundamental level. Within the scope of strongly correlated systems, pioneering investigations in recent years revealed, for example, superconductivity in various forms [1–5, 29], quantum criticality, in particular quantum phase transitions [6, 7], heavy fermion systems featuring very strong correlations [7, 8] and non-Fermi liquid behaviour [9, 10] as well as novel magnetic and electronic structures such as complex spin textures [13–17] and topological insulators [107, 108].

Many of the above-mentioned effects and phenomena may be suppressed by impurities or grain boundaries and were found to be absent in samples with inferior quality [4, 20–23]. Therefore, a lot of effort and ingenuity is being spent on preparing very pure samples most often in the single-crystal state, and their characterization. An important tool in this field are metallurgical phase diagrams as introduced in the next section.

3.1.1 Phase Diagrams and Metallurgy

In material science, the term "phase diagram" mostly refers to a plot of temperature versus composition, showing the structural phase transitions in a system of two or more constituents in equilibrium. This information is of great help when choosing the preparation technique and parameters to prepare a desired compound. A comprehensive introduction to metallurgy and phase diagrams may be found in Ref. [109]. In the following we focus on binary phase diagrams and congruently and incongruently melting compounds.

As an example, Fig. 3.2 shows the phase diagram of the B-Cr-system. In the following we refer to the solid lines that represent data from Ref. [110]. The y-axis shows the temperature and the x-axis the composition in at. % B. The melting points of elemental B at 2092 °C and Cr at 1863 °C are marked in red.

Binary phase diagrams consist of different regions that depict the thermodynamic phases in equilibrium. In the uppermost part, denoted with L, the system is in the liquid phase for all compositions. When the temperature falls below the first solid line, the so-called liquidus, the system starts to partially or completely solidify, depending on the composition. The temperature coordinate of the liquidus is strongly dependent on the composition and shows large differences, e.g. $T_1 = 2157\,°\mathrm{C}$ for CrB_2, marked in blue, and $T_2 = 1605\,°\mathrm{C}$ for 83 % B at point D, marked in orange. Phases having compositional fields narrower than 1 at. % appear as lines with a label stating the stoichiometry. In the B-Cr-system these are from low to high Cr content CrB_4, CrB_2, Cr_3B_4, CrB, Cr_5B_3 and Cr_2B. For all other compositions apart from 0 % and 100 % the system will form a mixture of different phases below the liquidus line.

The challenge in single crystal growth is to prepare a single phase in the form of a single-crystal specimen. In particular when growing crystals from the melt, the terms congruently and incongruently melting are of importance.

Congruently and Incongruently Melting Compounds

The compound CrB_2, marked in blue in Fig. 3.2, is congruently melting, i.e., it is in equilibrium with the melt. A liquid with this composition solidifies at 2157 °C and may form a single phase that is stable down to the lowest temperatures. Single crystals of congruently melting compounds may be grown fairly straightforwardly from the melt by means of standard techniques such as float-zoning or the Bridgman-Stockbarger process (see Sec. 3.2).

The compound Cr_5B_3, marked in green in Fig. 3.2, is incongruently melting, i.e., it is in equilibrium with the liquid and a solid phase (CrB). A liquid with this

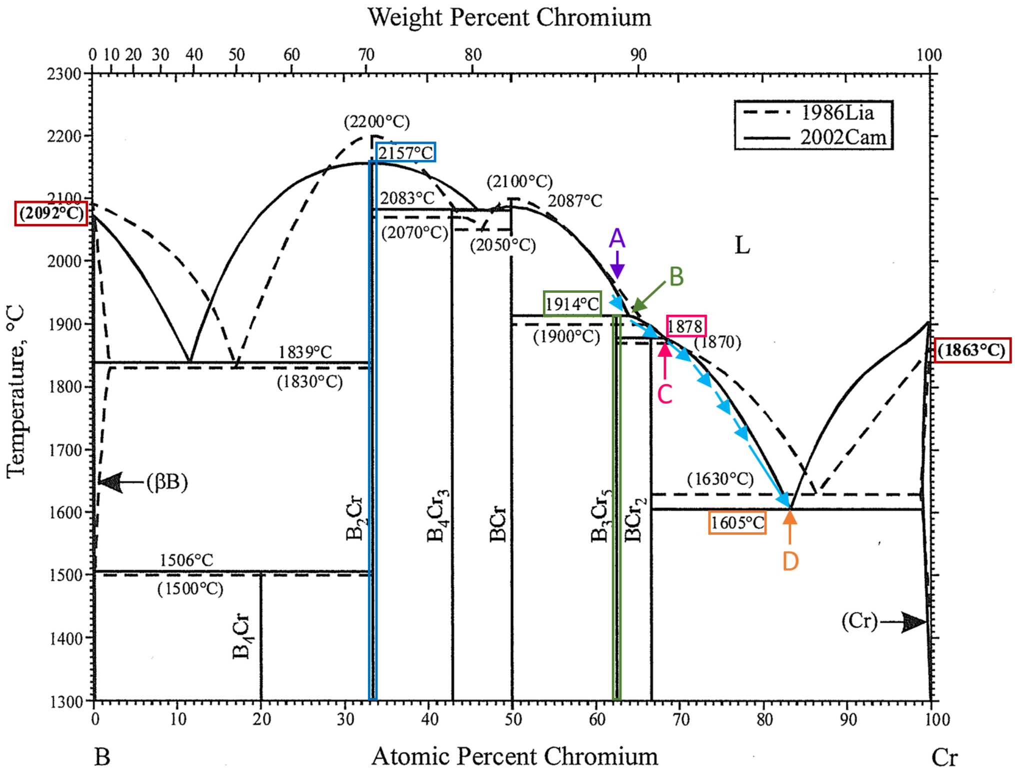

Figure 3.2: Binary phase diagram of the B-Cr-system. In the text we refer to the solid lines that represent data from Ref. [110]. The melting points of elemental B and Cr are marked in red. The congruently melting phase CrB_2, studied in this thesis, and the incongruently melting phase Cr_5B_3 are marked in blue and green, respectively. A, B, C and D are points of interest in the process of solidification of a melt with overall composition Cr_5B_3 and are referred to in the text. Figure adapted from Ref. [42].

composition may consecutively form the phases CrB (from A to B), Cr_5B_3 (from B to C), Cr_2B (from C to D) and elemental Cr when solidifying. This means, that the cooling of a melt with the composition Cr_5B_3 results in four solid phases. Single crystals of incongruently melting compounds may be prepared with advanced techniques such as the travelling solvent floating zone method (see Sec. 3.2).

3.2 Techniques of Sample Preparation

In the following the techniques for sample preparation will be presented. First, the basic concepts and ideas when dealing with intermetallic compounds are reviewed. After a description of the preparation of polycrystalline samples and the starting material, the single crystal growth technique used in this thesis will be described, namely optical float-zoning.

3.2.1 Basic Prerequisites and Remarks

The highest possible purity of the starting elements and the cleanest possible apparatus used for the synthesis are the two basic requirements when preparing high-quality material. Pure starting elements may be purchased from several specialized companies. For the synthesis, the first step is usually the precise weighing of the starting material in desired portions and stoichiometry. Next, the preparation is generally carried out by heating in a furnace under vacuum or an atmosphere of inert gas. Particular attention should be paid to the choice of crucible, the atmosphere and the composition:

- To avoid contamination, crucible-free techniques such as float-zoning are preferable. If that is impossible, water-cooled crucibles may be used. A third choice are hot crucibles made of refractory inert material.
- To minimize contamination by oxygen or moisture, all furnaces are pumped to a vacuum as high as possible prior to synthesis.
- To minimize evaporation losses, the synthesis is frequently carried out under a high-purity inert gas atmosphere.

3.2.2 Preparation of Polycrystalline Material

To prepare polycrystalline ingots, the starting elements are heated in a suitably shaped crucible until they melt. After cooling, a polycrystalline specimen is obtained which may be used for the preparation of a single crystal. For the studies reported in this thesis, the following three methods were used.

Whenever possible, the heating was realized by means of radio-frequency induction (RF) in a Rod Casting Furnace (RCF, see Sec. 3.3.3) under a high-purity argon atmosphere. The advantages of the RCF are minimal evaporative losses because of gentle heating by RF, mixing of the melt driven by eddy currents, and a minimal risk of contamination as the furnace employs a water-cooled crucible. However, RF is usually only feasible when at least one starting element is metallic and exceeds dimensions of at least 1 mm. Furthermore, the RCF is limited to typical maximum temperatures of approximately 2200 °C.

Another route for the preparation of the initial ingots is heating by argon plasma in a high-purity argon atmosphere in an Arc Melting Furnace (AMF, see Sec. 3.3.3), which also uses a water-cooled crucible. This technique works for every type and geometry of material and may reach temperatures exceeding 3500 °C, but entails larger evaporative losses.

A third option is the synthesis in a hot crucible made of refractory non-reactive materials. The ampoule containing the starting elements is evacuated, optionally flooded with inert gas, and finally sealed or welded leak tight. Heating is generated indirectly by means of a resistively heated tube or muffle furnace or, in the case of a metallic crucible, using RF induction. This method is chosen when the compound of interest comprises elements with high vapour pressures, since the evaporative losses may be reduced by the small volume in the sealed ampoule. Second, with the PID-controlled heating of a tube or muffle furnace, well-defined temperature profiles may be generated and compounds featuring a more complex metallurgy may be made. The disadvantage of this technique represents a higher risk of contamination due to the contact of the melt with the hot ampoule.

Depending on the compound, we used the RCF and the AMF to prepare either polycrystalline samples or the starting material for single crystal growth by means of float-zoning.

3.2.3 Single Crystal Growth Techniques

A large number of single crystal growth techniques has been reported in the literature. Comprehensive overviews may be found in Refs. [109, 111]. In general, four categories of single crystal growth techniques may be distinguished [109]:

- growth from the gaseous phase, for example by chemical transport reactions
- growth from the melt, for example by optical float-zoning or the Bridgman-Stockbarger technique
- growth from the solid state, for example by annealing
- growth from the solution, for example by flux growth

In the following paragraphs the optical floating zone technique is introduced, as used in this thesis.

Optical Float-Zoning

Optical float-zoning plays an important role in fundamental research. Large single crystals with typical diameters between 5 mm and 10 mm and a length of several 10 mm's of a variety of intermetallic compounds and oxides have been grown by this method [112, 113]. Moreover, so-called travelling solvent optical float-zoning allows for the preparation of carefully selected incongruently melting systems. In the course of this thesis, optical float-zoning was used and the major part of the crystals were prepared with this technique using a novel high-pressure high-temperature optical floating zone furnace (HKZ, see Sec. 3.3.2).

Fig. 3.3 shows a schematic illustration of the technique. Prerequisites are two pure, homogeneous polycrystalline rods of the starting material. The top and bottom rods are referred to as feed and seed, respectively. A zone of molten material, created by optical heating, is passed in the vertical direction along the rods, which are counter rotating at typical speeds of about ten rotations per minute. Typical growth rates in the HKZ are between $0.1\,\mathrm{mm\,h^{-1}}$ for incongruently melting systems and up to $10\,\mathrm{mm\,h^{-1}}$ for congruently melting systems. Empirically, the molten zone

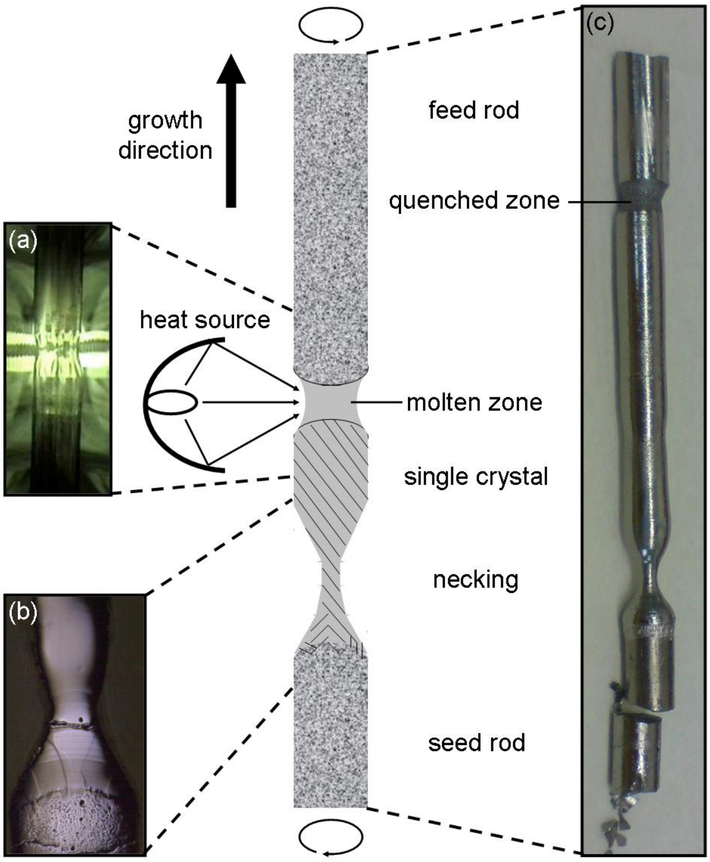

Figure 3.3: Schematic of the floating zone technique. A molten zone, created by a heat source, is passed in vertical direction through two counter rotating polycrystalline rods. (a) Photograph of the molten zone while float-zoning. (b) Polished cross-section of the beginning of a $Mn_{0.96}Co_{0.04}Si$ single crystal. (c) Float-zoned $Mn_{0.78}Fe_{0.22}Si$ single crystal. Figure from Ref. [24].

approximately has a height of the diameter of the starting rod to ensure stable growth. Under optimal conditions, this leads to the growth of a single crystal at the liquid-solid interface.

When using a polycrystalline seed rod, the single crystal grows starting with a grain selection of random orientation as schematically depicted in Fig. 3.4. This process may be accelerated by so-called necking, which represents a narrowing of the diameter of the zone at the start of the growth. Using this, grain selection is favoured and the chance for parallel growth of multiple grains is reduced. After growing a length of approximately one starting rod diameter, the zone diameter is increased again and the single crystal grows with a large diameter.

A crystal with a desired crystallographic orientation may be prepared by means of a suitable seed crystal. In this case, the molten zone is first moved downwards into the seed by 1 mm to 2 mm. Following this, the growth direction is reversed and the single crystal grows with the same orientation as the seed.

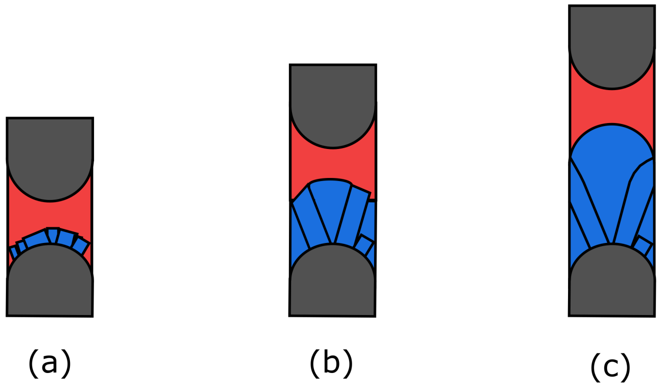

Figure 3.4: Grain selection during float-zoning. The polycrystalline starting rods are coloured in grey, the molten zone is coloured in red, single-crystal material is coloured in blue. From (a) to (c) the molten zone is moved from bottom to top. (a) First, multiple grains grow simultaneously. (b) Due to the convex shape of the bottom interface between melt and solid the grains are growing outwards. (c) Finally one grain, supersedes the other grains and grows over the whole diameter.

A big advantage of optical float-zoning is the absence of a crucible ruling out contamination by any crucible material. Second, most types of impurities have a higher solubility in the melt than in the solid. This leads to an additional purification of the material during the passage of the molten zone. A third advantage is the optical heating. This allows for metallic and insulating compounds to be grown and entails increased stability of the zone as compared to heating by radio-frequency induction. Finally, in comparison with other methods of crystal growth, optical floating zone produces large single crystals, which represents a precondition for certain experimental techniques.

The biggest disadvantage of optical float-zoning is a limited control of evaporative losses when preparing materials with high vapour pressures. In general, crystal growth by means of optical float-zoning is realised in a growth chamber in a quartz tube under an inert gas pressure of a few bar. By applying higher pressures, evaporation may be minimized, however, limited by the mechanical stability of the growth chamber. Moreover, the comparatively large volume of the growth chamber impedes the saturation of the atmosphere by the evaporating elements. Generally, the elements in a compound have different evaporation rates resulting in off-stoichiometry and the formation of defects in the crystal. Furthermore, the evaporated material may condense at the inner wall of the growth chamber and may block the optical path between light source and crystal. A need for a constant increase of heating power and the risk of damage to the growth chamber by excessive heat may result. Another drawback is the need for homogeneous polycrystalline rods of starting material which requires additional preparative steps usually involving heating or melting of the starting materials accompanied by a potential contamination or losses of stoichiometry due to evaporation.

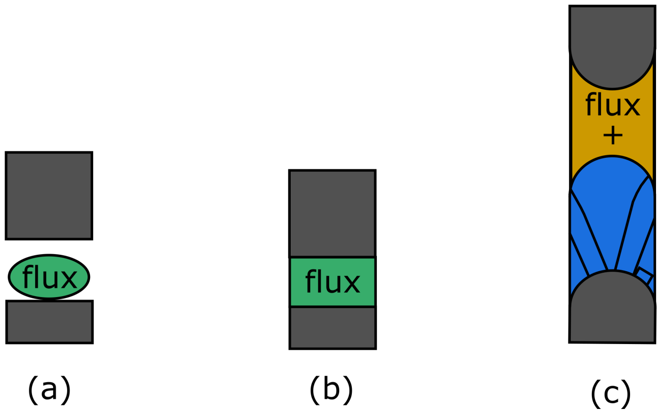

Figure 3.5: Travelling-solvent floating zone technique. The polycrystalline starting rods are coloured in grey, single-crystal material is coloured in blue, the flux is coloured in green. From (a) to (c) the molten zone is moved from bottom to top. (a) The bole of flux is deposited on the bottom rod. (b) First, the molten zone is formed from the flux only and the growth is started. (c) During the growth, the feed rod dissolves into the flux and the molten zone, coloured in yellow, consists of the flux and the desired compound. A single crystal of the desired compound grows by grain selection.

Travelling Solvent Floating Zone The travelling solvent floating zone technique (TSFZ) permits the preparation of compounds that exhibit a complex metallurgy, in particular incongruently melting near peritectic reactions [113, 114].

Fig. 3.5 shows a schematic illustration of the TSFZ. Prerequisites are besides two homogeneous, polycrystalline starting rods, a bole of flux, which consists of another low melting element (for example Sn, Pb, Zn, Al) or a different composition of the starting elements. In the latter case, the composition of the bole is chosen such that it is in equilibrium with the desired compound. At the beginning of the growth, the molten zone is created from the bole of flux and the growth in vertical direction is started immediately. Provided that the volume and the composition of the molten zone are constant during the process, the amount of the desired compound that crystallizes at the bottom equals to the amount of compound which is dissolved into the zone at the top, since seed and feed have the same composition. After successful grain selection, a single crystal of the desired composition grows at the bottom.

If an equilibrium composition and the desired composition differ by a few at. %, it is feasible to perform TSFZ without the bole of flux and the system will find the equilibrium by itself quickly during growth. This is also known as self-adjusted flux TSFZ. As part of this thesis it was used, e.g., to prepare the ErB_2 single crystal (see Chap. 5).

Besides the possibility to prepare materials systems with complex metallurgy, another advantage of the TSFZ is that the flux leads to a decrease of the melting temperature and hence the evaporation of material is reduced. Drawbacks of this method are that the flux is a source of potential contamination and that the speed of growth is often reduced significantly.

3.3 Crystal Growth Environment and Equipment

This section introduces equipment and furnaces used in this thesis. Most of the work related to sample preparation was conducted in the crystal growth laboratory at the chair for Topology of Correlated Systems, depicted in Fig. 3.6 and described in Sec. 3.3.1. A large part of this equipment was developed and/or improved in the course of the Ph.D. theses of Andreas Neubauer [115] and Andreas Bauer [24], as well as during the diploma thesis of Wolfgang Münzer [116] and the author's master's thesis [117]. As part of this thesis, a high-pressure high-temperature optical floating zone furnace was installed, commissioned and used for the preparation of several materials. The installation and adjustment process as well as first operations are described in Sec. 3.3.2. Further furnaces and equipment that have been used are described in Sec. 3.3.3.

3.3.1 Crystal Growth Laboratory and Infrastructure

Fig. 3.6 shows a photograph of the crystal growth laboratory at the chair for Topology of Correlated Systems at the Technical University of Munich. Following the principles introduced in Sec. 3.2, most of the apparatus in the crystal growth laboratory is designed to prepare high-purity intermetallic compounds. In particular, most furnaces are all-metal sealed and bakeable to reach pressures as low as 10^{-8} mbar in the ultra-high vacuum range using turbopumps backed by scroll pumps. Some furnaces are additionally equipped with ion-getter pumps to reach pressures as low as 10^{-10} mbar. All pumps are oil-free to avoid contamination by back diffusion.

For use as an inert atmosphere, 6N (99.9999 % purity) argon is available via a central gas supply. It may be purified additionally to 9N by point-of-use room temperature purifiers (SAES MicroTorr MC190). Furthermore, 4N5 oxygen and 5N nitrogen are available for preparing oxides or nitrides.

Where possible, the ultra-clean atmosphere is used for the materials synthesis by means of crucible-free techniques or in combination with water-cooled crucibles. A

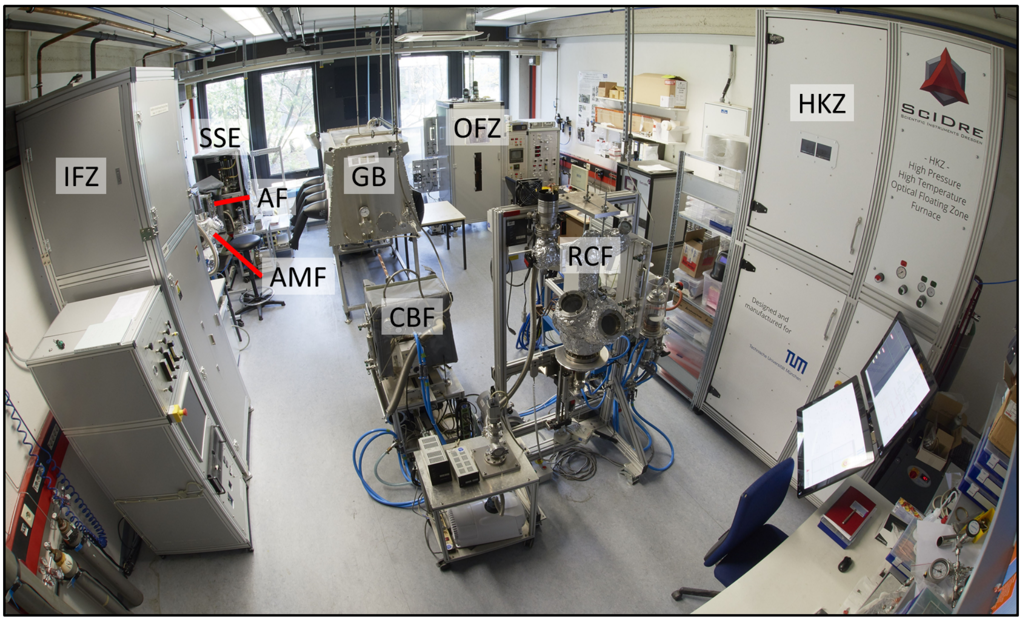

Figure 3.6: Photograph of the crystal growth laboratory at the chair for Topology of Correlated Systems at the Technical University of Munich. Apparatus: four mirror optical floating zone furnace (OFZ), four mirror inclined optical floating zone furnace (IFZ), glovebox (GB), horizontal cold boat furnace (CBF), rod casting furnace (RCF), arc melting furnace (AMF), resistive annealing furnace (AF), and solid state electrotransport furnace (SSE). The high-pressure high-temperature optical floating zone furnace (HKZ) was setup and put into operation in the course of this thesis.

CELES MP 50kW radio-frequency generator may be used for induction melting in several furnaces at frequencies between 100 kHz and 400 kHz.

High-purity starting elements are purchased from specialized companies such as Alfa Aesar, Ames Laboratory, MaTecK, or smart-elements with typical purities between 4N and 7N depending on availability. Usually, starting materials are obtained in small quantities (granules, pellets, shots) of a site of a few mm's or in powders of varying grain sizes. Insensitive elements, packaged in clean containers, are stored in a clean environment in air, whereas oxygen and/or water-sensitive elements, packaged in sealed metal or quartz ampoules under inert gas, are stored and processed in a bespoke glovebox under an argon atmosphere of approximately 1 ppm oxygen and water.

For the preparation of materials the elements are weighed in stoichiometric portions with an accuracy of 10 µg. For sensitive elements, this is done in the glovebox. The subsequent approach taken in the preparation is strongly dependent on the specific properties of the compound and the desired quality. For each material, an account of the particular preparation route will be given as part of the chapter reporting the entire study. Detailed information on the laboratory and equipment as well as examples for growth and preparation may be found in Refs. [24, 115–119]. In the following sections, only the facilities that were used or developed in the context of this thesis are described in detail.

3.3.2 High-Pressure High-Temperature Optical Floating Zone Furnace

The Hochdruck-Kristallzüchtungsanlage (HKZ), Scientific Instruments Dresden GmbH is a high-pressure high-temperature optical floating zone furnace. Its key feature is a double ellipsoid mirror vertical setup, which offers certain advantages on the focussing as compared to other commercially available two mirror or four mirror horizontal furnaces [120, 121]. As a part of this thesis, the HKZ was installed and put into operation followed by several hardware and software updates as well as recurrent adjustments of the optical configuration until reliable preparation of high quality single crystals became possible.

The tests ensued by creating a molten zone and assessing its shape and stability for Al_2O_3, Cu, and Zr as test materials . In addition, large single crystals of Zr, FeSi, CoSi, $PrNi_5$, and $CeAl_2$ were prepared and subsequently characterized with the help of x-ray Laue diffraction and the bulk properties studied. Furthermore, single crystals of CrB_x with $x = 1.90$, 2.00, 2.05, 2.10, and ErB_2 were successfully prepared in the HKZ and investigated as part of this thesis.

Setup and Geometry

Fig. 3.7(a) shows a photograph of the high-pressure high-temperature optical floating zone furnace (HKZ), Scientific Instruments Dresden GmbH. The furnace consists of an upper section that contains the upper elliptical mirror (1), the upper and lower linear and rotation drives (2), which permit linear speeds from $0.1\,\mathrm{mm\,h^{-1}}$ to $150\,\mathrm{mm\,h^{-1}}$ and rotational speeds from $1\,\mathrm{min^{-1}}$ to $30\,\mathrm{min^{-1}}$, as well as the sample chamber (3). The latter is sealed by FKM O-rings and consists of fused silica or sapphire for working pressures of 20 bar or 50 bar, respectively. A smaller quartz tube is attached inside with the help of O-rings and protects the main chamber from pollution by evaporation of processed material. Although the vacuum chamber of the HKZ is not bakeable, pressures down to 10^{-7} mbar may be reached with a turbo pump.

A manual gas handling system (4) is used to limit the maximum pressure, whereas the software (6) maintains the process pressure at adjustable constant gas flows between $0.1\,\mathrm{l\,min^{-1}}$ and $1\,\mathrm{l\,min^{-1}}$. The furnace is supplied with 6N argon that may be cleaned by a hot gas purifier achieving nominal oxygen concentrations below 10^{-11} ppm. A mechanical power shutter (5) that may be opened in 0.1 % steps separates the upper from the lower section and is used to control the amount of heating power reaching the upper mirror.

An air-cooled Xenon arc lamp (7) is positioned at the focal point of the lower mirror (9) generating maximum temperatures of up to approximately 3000 °C in the sample

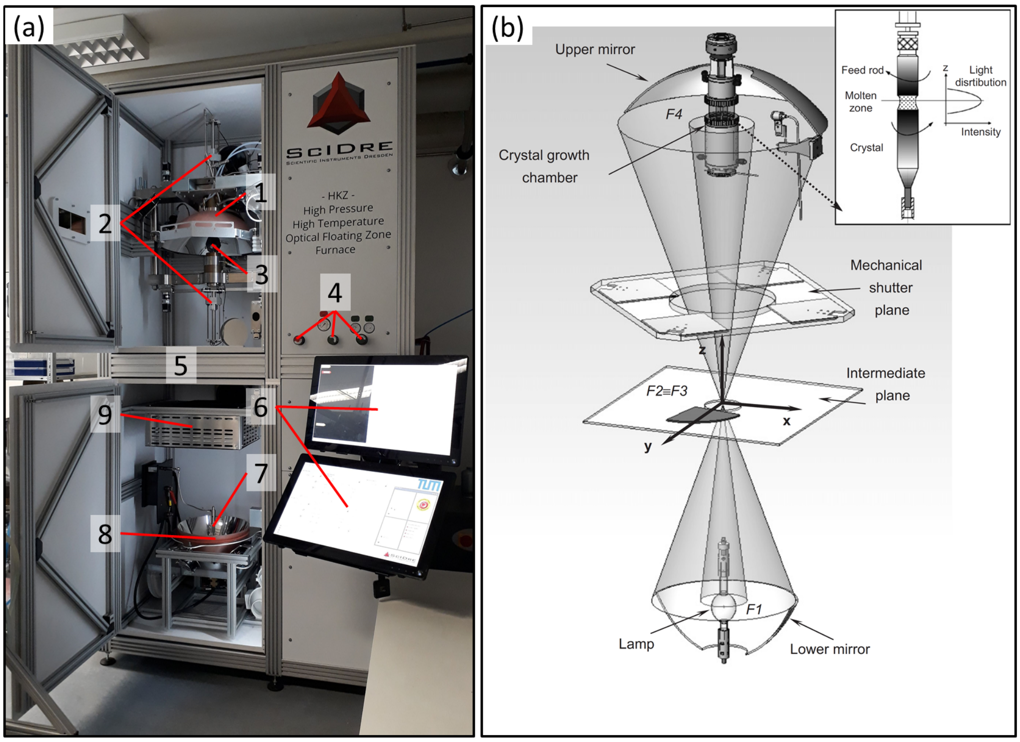

Figure 3.7: The high-pressure high-temperature optical floating zone furnace (HKZ), Scientific Instruments Dresden GmbH: (1) upper elliptical mirror, (2) linear and rotation drives, (3) sample chamber, (4) manual gas controls, (5) plain of the mechanical power shutter (the actual shutter is located inside, behind the frame), (6) touch-screens for software control, (7) xenon short arc lamp, (8) lower elliptical mirror, (9) chopper system for measurement of the sample temperature by pyrometer. (b) Scheme of the optical configuration in the two-mirror vertical setup. Figure taken from Ref. [120].

chamber. Lamps are available with powers of 3 kW, 5 kW, or 6.5 kW. The position of the lamp may be adjusted by the operating software using a XYZ-table with a precision of 0.1 mm, which permits the exact control of the radiation distribution on the sample surface. Especially for growing materials sensitive to thermal shock, this may be exploited to apply a broad distribution of light in z-direction resulting in more continuous and gentle heating.

Furthermore, the HKZ permits in-situ temperature measurements during the growth process. This feature is realized by interrupting the optical path for a few milliseconds with a chopper system (9) while simultaneously measuring the unbiased sample radiation with a two-colour pyrometer located in the upper section of the facility.

The optical configuration is depicted in Fig. 3.7(b), showing a double ellipsoid-mirror vertical setup where the Xenon arc lamp is located at the focal point of the lower mirror. F1, F2 and F3, F4 are focal points of lower and upper ellipsoids, respectively; in the present case F2 and F3 coincide. The inset shows a sketch of the resulting profile of illumionation on the crystal surface.

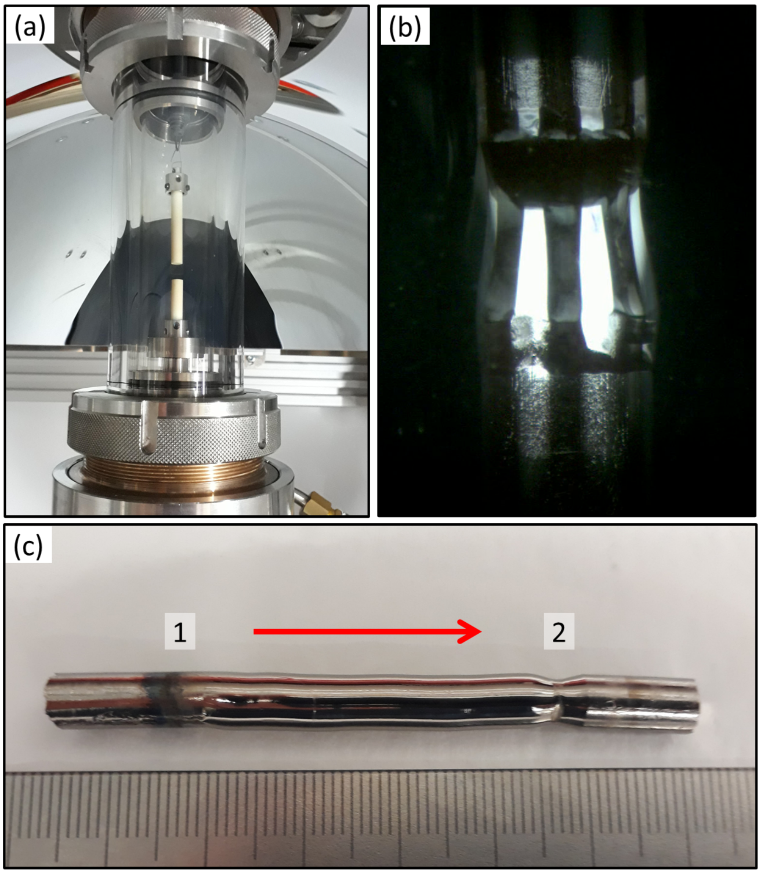

Figure 3.8: Sample chamber and crystal growth in the HKZ. (a) Photograph of the sample chamber with an Al_2O_3 test sample. (b) Molten zone during the single crytal growth of CoSi. (c) CoSi single crystal with a length of 35 mm from (1) the beginning of the growth to (2) the end of the growth, where the solidified zone may be discerned. The growth direction is indicated by the red arrow.

A water-water heat exchanger provides cooling water for parts that are subject to strong radiation, such as the power shutter or the support structure of the sample chamber, which are depicted in Fig. 3.8(a) at the top and bottom.

The crystal growth is monitored with the help of a CCD camera, where the software permits to record the process as well as the assessment of the shape of the zone and its size. Fig. 3.8(b) shows a photograph of the molten zone of CoSi. Here, excellent adjustment of the optical configuration results in the high symmetry of the molten zone and the two bright vertical stripes, representing the reflections of the lamp. The CoSi single crystal with a length of 35 mm, grown in the HKZ, is depicted in Fig. 3.8(c).

Advantages of the Vertical Setup

The advantages of the double ellipsoid mirror vertical setup may be summarized as follows (see also Refs. [120, 121]).

- The axial symmetry provides excellent uniform azimuthal heating of the molten zone. The irradiation power can be controlled by a mechanical shutter as well as by the electric power of the arc lamp.
- The large upper mirror and the narrow bundle of light irradiating the molten zone permit easy access to the sample chamber as well as sufficient room for mounting additional auxiliary equipment.
- The shallow solid angle of light irradiating the sample permits the use of shorter sample chambers (double mirror: 60 mm vs. four mirror: 350 mm) and hence the application of higher pressures up to 150 bar.
- Refractory materials with melting temperatures of up to 3000 °C may be grown due to the very high efficiency of the focussing of the radiation.

Adjustment of the Optical Configuration

Despite its advantages in radiation focussing compared to two and four mirror furnaces, the biggest drawback of the HKZ is the need for a tedious adjustment process of the optical path to permit the growth of high-quality single crystals. In the HKZ, the distance between lamp and sample is approximately 2000 mm, compared to approximately 50 mm in the horizontal four mirror setup. Therefore, a small displacement in the position of the arc of the lamp in the HKZ setup leads to a considerably larger displacement of the irradiated area on the sample than in the horizontal case.

For the adjustment of the HKZ, two reference LED setups, a measuring tape, a sheet of paper with a printed target and an Al_2O_3 rod are used. Assuming that the furnace and all fixed parts are perpendicular to the ground, the following steps are taken:

1. The lower mirror is aligned perpendicular to the ground. For this, the lower reference LED setup is mounted at the position of the arc of the xenon lamp. With the help of a measuring tape, the lower mirror is positioned in its socket such that the distance from the edge of the mirror to the socket is the same everywhere. Next, the tilt of the lower mirror socket is aligned with three adjustment screws. The correct position is verified with the help of the image

of the reference LED on the target paper, which is consecutively checked at the bottom of the pyrometer shutter, on top of the pyrometer shutter, and on top of the power shutter. This image must be symmetric and concentric while the vertical position of the LED is moved through its whole range.

2. The upper mirror is aligned perpendicular to the ground. For this, the upper reference LED setup is mounted at the position of the sample. The tilt of the upper mirror is adjusted with three screws and the correct position is consecutively checked by placing the target paper on the same three levels described above. The image must be symmetric and concentric while the vertical position of the LED is moved through its whole range.

3. The horizontal position of the upper mirror is adjusted. Instead of the upper reference LED setup, the Al_2O_3 rod is mounted at the position of the sample. The reflection of the lower reference LED setup can be observed on the surface of the Al_2O_3 rod. The upper mirror is moved in its socket by hand until the image on the Al_2O_3 rod is symmetric. While the vertical position of the lower reference LED is moved through its whole range, the image must stay symmetric. (However, the vertical position of the image on the Al_2O_3 rod and its height is changing with the vertical position of the lower LED.)

Growth and Characterization of Test Materials

Over the course of several iterations the optical configuration of the HKZ was adjusted such that high-quality single crystals could be prepared. During this process, single crystals of FeSi, CoSi, $PrNi_5$ and $CeAl_2$ were grown and subsequently characterized by x-ray Laue diffraction (see Sec. 3.4.2).

For example, photographs and x-ray Laue patterns of two CoSi single crystals prepared in the HKZ are depicted in Fig. 3.9. Figs. 3.9(a) and (b) show photographs of HKZ7, which was grown with a seed along $\langle 110 \rangle$, and HKZ11, which was grown by grain selection, respectively. For each crystal three Laue patterns were recorded at the positions labelled (1), (2), and (3) at an interval of approximately 5 mm along the growth axis. These Laue patterns are depicted in Figs. 3.9(a)-1, (a)-2, and (a)-3 for the crystal HKZ7 and in Figs. 3.9(b)-1, (b)-2, and (b)-3 for the crystal HKZ11. Nevertheless HKZ7 was grown with a seed, a clear rotation of the Laue pattern from Fig. 3.9(a)-1 to (a)-3 indicates a change of the crystallographic orientation. Furthermore, the observation of double peaks in Fig. 3.9(a)-1 suggests two crystalline grains that are misaligned by a few degrees. Such a rotation of the main crystallographic directions as a function of the growth direction or the parallel growth of several big grains indicate an asymmetric alignment of the optical configuration. Both effects were observed in the first crystals prepared in the HKZ.

Following a gradual improvement of the optical configuration the test crystals reproducibly featured a high crystalline quality. This may be illustrated with the help of HKZ11, which was grown by grain selection following several adjustment cycles of the HKZ. In Figs. 3.9(b)-1), (b)-2, and (b)-3 there is no noticeable change of the Laue pattern indicating high crystalline quality of the entire specimen.

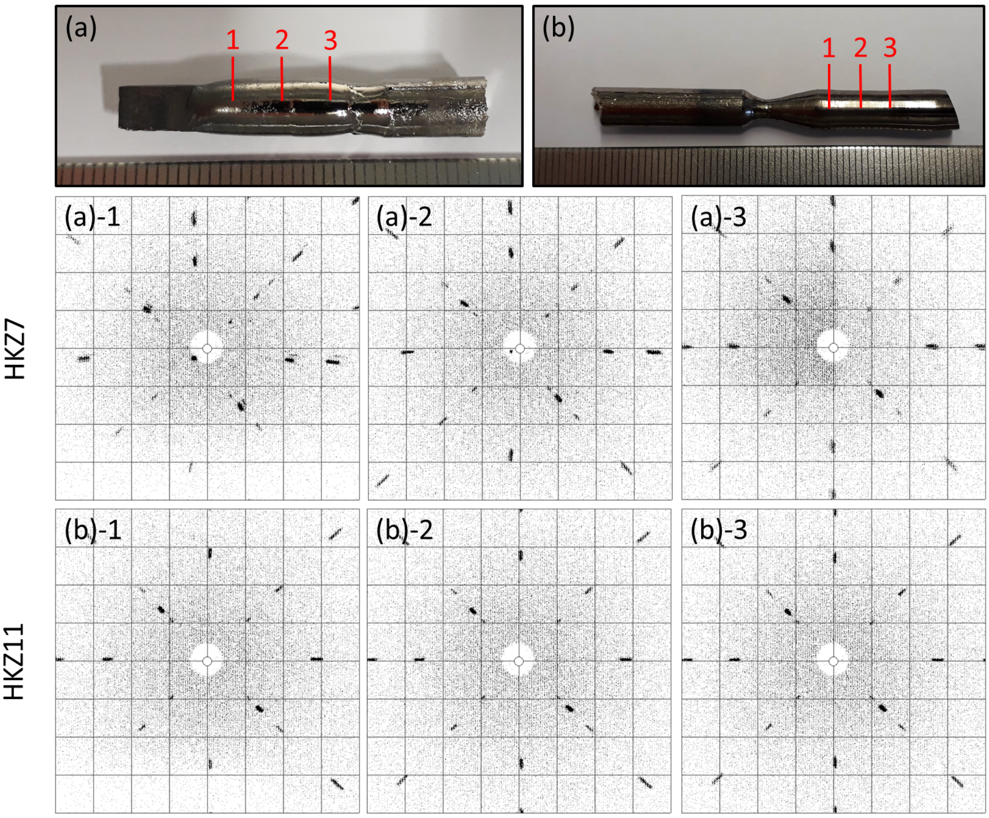

Figure 3.9: Two CoSi single crystals prepared in the HKZ. (a) HKZ7, grown with a seed along ⟨110⟩. (b) HKZ11, grown by grain selection. For each crystal, three Laue patterns along ⟨100⟩ were recorded at an interval of 5 mm along the growth axis. Those spots are labelled with (1), (2), and (3) in red. (a)-1, (a)-2, and (a)-3 show the Laue patterns at position (1), (2), and (3) of HKZ7, respectively. (b)-1, (b)-2, and (b)-3 show the Laue patterns at position (1), (2), and (3) of HKZ11, respectively.

3.3.3 Furnaces and Apparatus

This section provides basic information on further apparatus operated in the crystal growth laboratory and, in particular, the furnaces that were regularly used, namely the rod casting furnace (RCF) and the arc melting furnace (AMF).

Rod Casting Furnace (RCF)

The rod casting furnace is designed to prepare cylindrically shaped, high-purity polycrystalline material by means of radio-frequency induction melting in an ultra-clean atmosphere.

Fig. 3.10(a) shows a CAD rendering of the central parts of the furnace. The starting elements are placed in a water-cooled Hukin crucible (see Fig. 3.10(b)), the system is evacuated to UHV and subsequently 1.4 bar 9N argon gas is applied. Synthesis of the educts is realized by radio-frequency induction melting where temperatures of about 2200 °C can be reached. After homogenization in the liquid state, the melt may be cast into a homogeneous starting rod. Water-cooled casting moulds with various dimensions permit the fabrication of ingots with diameters between 6 mm and 10 mm and a maximum length of 90 mm (see Fig. 3.10(c) and (d)). In the RCF at least one starting element has to be metallic with a site of at least 1 mm, otherwise the induction heating is insufficient.

In the context of this thesis, the RCF was used to prepare starting rods of CrB_x with $x = 1.90$, 2.00, 2.05, 2.10 for single crystal growth as well as polycrystalline $\mathrm{Fe_{1-x}Cr_x}$ samples. A comprehensive account on the RCF may be found in Ref. [118].

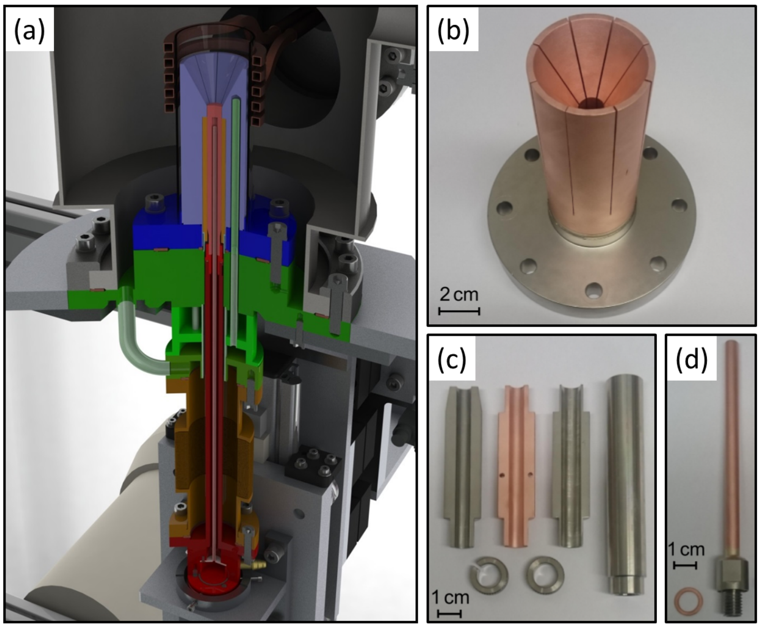

Figure 3.10: The rod casting furnace (RCF). (a) Coloured-shaded CAD depiction of the central parts of the RCF. Hukin crucible (blue), mounting flange (green), casting mould located inside the crucible (orange), bellows (brown), and casting rod (red). (b) Photograph of a Hukin crucible. (c) Photographs of various casting moulds. (d) Photograph of a casting rod with copper seal. Figures adapted after Refs. [24, 118].

Arc Melting Furnace (AMF)

The arc melting furnace uses an argon plasma torch to prepare polycrystalline starting material or samples as well as to weld-shut metallic ampoules in a high-purity argon atmosphere.

A photograph of the furnace is shown in Fig. 3.11(a). A rendered CAD-figure is depicted in Fig. 3.11(b). The furnace reaches temperatures exceeding 3500 °C. The starting elements are not required to be metallic or of a certain minimum size. The bakeable vacuum chamber reaches UHV pressures, where 9N argon gas is used during the process. Water-cooled casting moulds of various shapes permit the preparation of ingots and rods. In addition, the AMF may be connected to the glovebox such that starting elements sensitive to oxygen or water may be readily processed. Furthermore, metallic ampoules of varying sizes may be welded shut with the help of a bespoke holder (see Fig. 3.11(c) and (d)).

In this thesis, the AMF was used to prepare the starting material for CrB_x with $x = 1.90$, 2.00, 2.05, 2.00, and ErB_2. Detailed information about the furnace may be found in Refs. [117, 119].

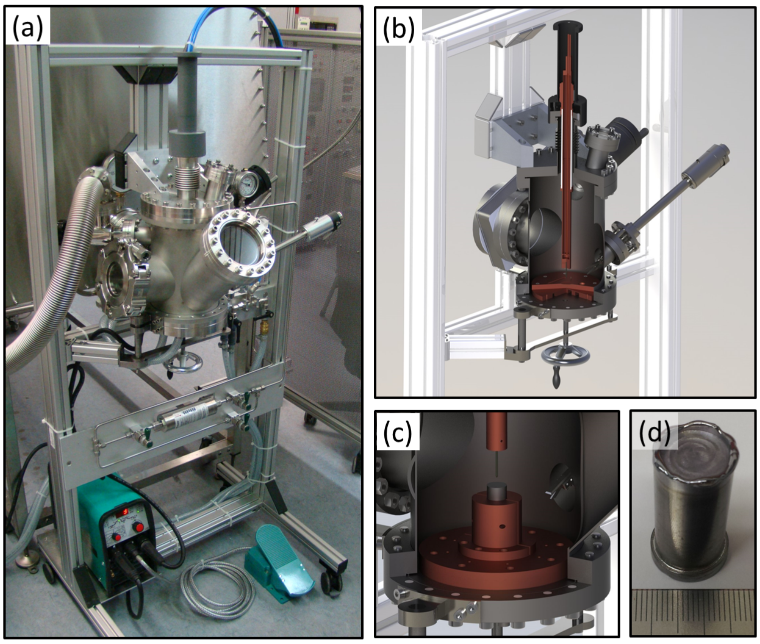

Figure 3.11: The arc melting furnace (AMF). (a) Photograph of the AMF. (b) Cut-away CAD-view of the vacuum chamber. (c) A rendered view of a metallic ampoule to be welded shut as mounted in the AMF. (d) Photograph of a tantalum ampoule as prepared in the AMF.

3.4 Methods for Characterization and Physical Properties

The following section presents the methods and the apparatus used for the characterization. In this thesis, we used x-ray powder diffraction, x-ray Laue diffraction, extraction and vibrating sample magnetometry, ac magnetometry, specific heat calorimetry and measurements of the electrical transport properties in a broad range of temperatures and magnetic fields.

The characterization laboratory at the chair for Topology of Correlated Systems at the Technical University of Munich is depicted in Fig. 3.12. It contains a large part of the apparatus listed above. Further facilities such as the x-ray Laue diffractometer are located in the central crystal growth laboratory of the Physik Department of the Technische Universität München. A wire bonder is located at the Zentrum für Nanotechnologie und Nanomaterialien of the Technical University of Munich.

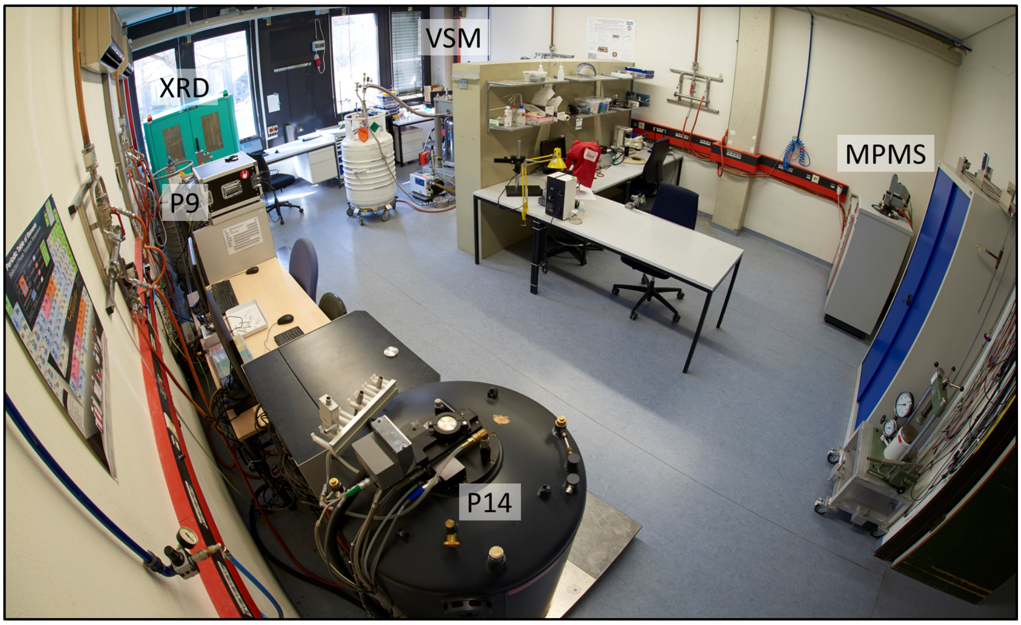

Figure 3.12: Photograph of the characterization laboratory at the chair for Topology of Correlated Systems at the Technical University of Munich. Apparatus: XRD: X-ray Guinier diffractometer G670 (Huber Diffraktionstechnik), P9: 9 T Physical Property Measurement System (Quantum Design), P14: 14 T Physical Property Measurement System (Quantum Design), VSM: 9 T Vibrating sample magnetometer (Oxford Instruments), MPMS: 5 T Magnetic Property Measurement System (Quantum Design).

3.4.1 Cryogenic Apparatus

Physical Property Measurement System (PPMS)

The two physical property measurement systems (Quantum Design, Inc.) in the characterization laboratory represent versatile measurement platforms comprising helium-4 cryostats, electronics and software, that are designed for the determination of various bulk properties at temperatures from 1.8 K to 400 K. The P9 is equipped with a 9 T superconducting magnet where the extraction magnetization, ac susceptibility for frequencies from 10 Hz to 10 000 Hz and ac electrical transport may be measured. The P14 is equipped with a 14 T superconducting magnet. It was used for measurements of vibrating sample magnetization, ac susceptibility at frequencies from 10 Hz to 10 000 Hz, ac electrical transport, and the specific heat. In this thesis, both PPMS were extensively used for materials analysis and determination of magnetic phase diagrams.

Vibrating Sample Magnetometer (VSM)

The vibrating sample magnetometer (Oxford Instruments) consists of a continuous flow helium-4 cryostat accessing temperatures between 2.3 K and 300 K and a 9 T superconducting magnet. Electronic panels and software is used to control the experimental parameters and a lock-in amplifier (Stanford Research Systems 830) is used to record the magnetization data, measured with the vibrating sample technique. During this work, the VSM was used to measure the magnetization of diboride compounds.

3.4.2 X-Ray Diffraction Techniques

X-Ray Powder Diffraction in Transmission Guinier Geometry

In this thesis, x-ray powder diffraction was measured in a Huber G670 (Huber Diffraktionstechnik GmbH & Co. KG) in transmission Guinier geometry [122]. Fig. 3.13(a) shows a photograph of the diffractometer, which comprises a Mo x-ray tube (1) with a characteristic wavelength of $\lambda = 0.7107\,\text{Å}$, a Ge monochromator (2), a sample holder (3), and a curved imaging-plate Guinier camera (4). The measurement geometry in the G670 is schematically illustrated in Fig. 3.13(b). The primary beam is focussed on a Ge monochromator crystal, is reflected and transmits the powder sample before it is absorbed by a beam stop. The scattered intensity is collected with the curved imaging-plate Guinier camera in an angular range from 4° to 100°.

Fine powders were prepared by hand grinding in an agate mortar, or, in the case of hard and tough materials, with the help of a fully automatic cryo mill (CryoMill, Retsch GmbH). For a standard measurement at room temperature, the powder is spread on a mylar foil sample support. Depending on the grain size of the powder and the scattering factors of the material, sufficient data to perform a phase analysis may be measured within 5 min to 30 min.

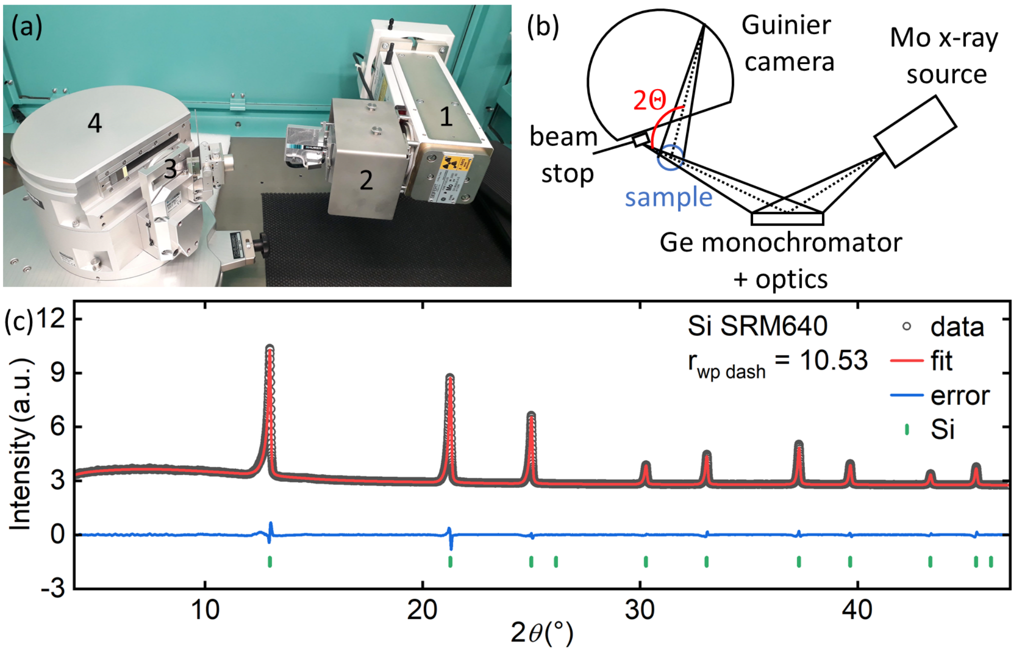

Figure 3.13: X-ray powder diffraction in Guinier geometry. (a) Photograph of the Huber Guinier G670. (1) Mo x-ray source, (2) Ge monochromator, (3) sample holder, (4) Guinier camera. (b) Top view schematic illustration of powder diffraction in Guinier transmission geometry. (c) Diffraction pattern with Rietveld refinement of silicon standard SRM640e [123] recorded with the Huber G670.

To analyze the diffraction data Rietveld refinements with the program Topas Academic [124] were performed. Crystallographic information was collected from the inorganic crystal structure database [125]. The quality of the Rietveld refinement was assessed by the so-called R-factors, where smaller values indicate a better fit of the model to the data. To distinguish between a good and a bad refinement, it is also necessary to view the observed and calculated patterns graphically and to ensure that the model is chemically plausible [126]. As an example, Fig. 3.13(c) shows the pattern of silicon standard SRM640e [123] with a Rietveld refinement. The asymmetric form of the peaks and the higher background for small angles are artefacts of the Guinier geometry and have to be accounted for in the refinement. The analysis yields a $r_{\mathrm{wp\ dash}} = 10.53$ and the absence of additional peaks as well as the optical appearance are characteristic of a meaningful refinement.

During this thesis, the Huber G670 was set up and used for powder diffraction of CrB_x with $x = 1.90$, 2.00, 2.05, 2.10, and ErB_2 as well as the series of $\mathrm{Fe}_x\mathrm{Cr}_{1-x}$ polycrystalline samples.

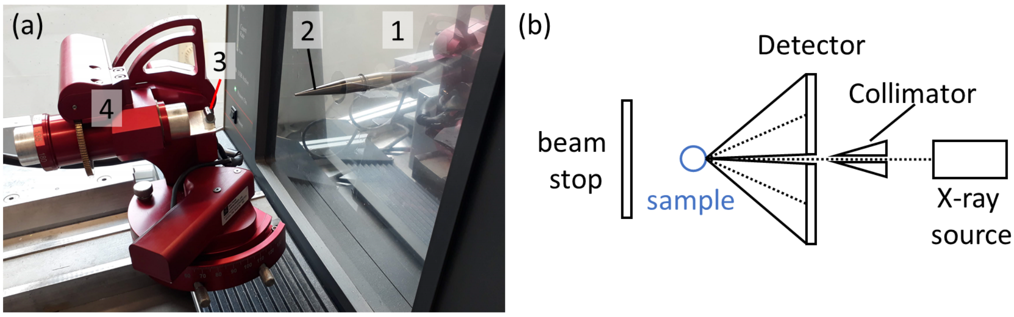

Figure 3.14: Real-time x-ray Laue diffraction. (a) Photograph of the diffractometer. (1) Detector, (2) collimator and polychromatic x-ray source, (3) single-crystal ingot, (4) Goniometer. (b) Schematic illustration of back-reflection Laue diffraction.

Real-Time X-Ray Laue Diffraction

In this thesis, real-time back-reflection Laue patterns were collected by means of a MWL 120 (Multiwire Laboratories Ltd.) x-ray Laue Diffractometer located at the central crystal growth laboratory of the Physik Department of the Technical University of Munich. Fig. 3.14(a) shows a photograph of the diffractometer. The sample (3) is mounted on a Goniometer (4) and irradiated by a collimated polychromatic x-ray beam (2). The back-reflected intensity is collected by the planar detector (1). A schematic illustration is depicted in Fig. 3.14(b). In this thesis the Laue diffractometer was used to check the crystalline quality of the single crystals prepared, as presented in Sec. 3.3.2. Moreover, the diffractometer was used in the process of cutting smaller oriented samples from the ingots.

3.4.3 Magnetometry

Magnetization Measurements

In this thesis, the magnetization was measured with a single-shot extraction technique in the PPMS (see Sec. 3.4.1) and a vibrating sample technique in the PPMS and the VSM (see Sec. 3.4.1). The sample was mounted with VGE-7031 varnish on a PEEK sample holder and additionally secured with PTFE tape. In the following the calibration procedure used in the PPMS is summarized.

Calibration of the PPMS Magnetometer Fig. 3.15 shows the magnetization M of 4N7 palladium in magnetic fields from $-14\,\mathrm{T}$ to $14\,\mathrm{T}$, measured at a constant temperature of $298\,\mathrm{K}$ in the PPMS. The sample was provided by Quantum Design for the purpose of the calibration of the magnetometer [127, 128]. As expected from the paramagnetic character of Pd, a linear behaviour over the entire field range is observed. In this case, the relation between the magnetization M and the external magnetic field H_{ext} may be written as

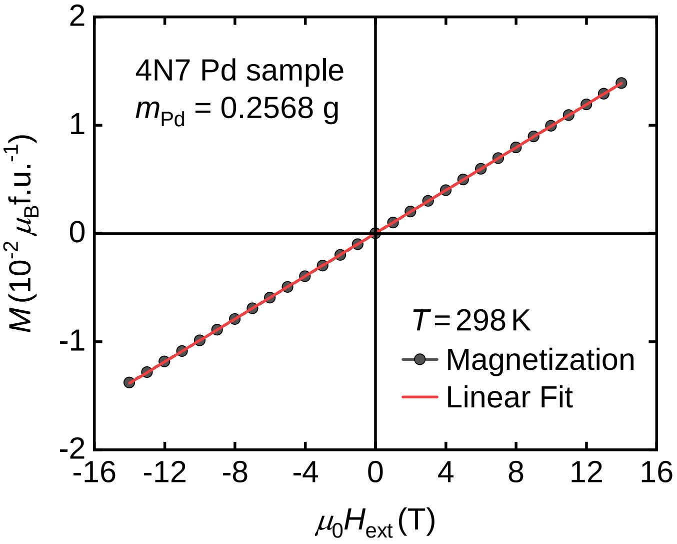

Figure 3.15: Magnetization of a 4N7 palladium sample in magnetic fields from −14 T to 14 T at a temperature of 298 K. The sample with a mass of $m_{\mathrm{Pd}} =$ 0.2568 g is used for calibration of the PPMS magnetometer.

$$M = \chi_{\mathrm{dc}} \cdot H_{\mathrm{ext}} \tag{3.1}$$

with χ_{dc} being the magnetic dc susceptibility. A linear fit to the curve in the field range −1 T to 1 T yields $\chi_{\mathrm{dc,measured}} = 9.9907 \times 10^{-4} \mu_{\mathrm{B}}/\mathrm{f.u.} \cdot \mathrm{T}$. Compared to the theoretical value of $\chi_{\mathrm{dc,theoretical}} = 1.0004 \times 10^{-3} \mu_{\mathrm{B}}/\mathrm{f.u.} \cdot \mathrm{T}$, this corresponds to a difference of 0.13 %. The presumed systematic errors due to ferromagnetic impurities in the Pd sample as well as the accuracy of the magnetometer amount to 1 %. Hence the difference of 0.13 % indicates a successful calibration.

AC Susceptibility Measurements

In this thesis ac susceptibility measurements were conducted in the PPMS (see Sec. 3.4.1). The sample was mounted with VGE-7031 varnish on a PEEK sample holder and additionally secured with PTFE tape. In the ac magnetic measurements, an ac field

$$H_{\mathrm{ac}}(\omega, t) = H_{\mathrm{ac}} \sin(\omega t) \tag{3.2}$$

was applied to a sample and the resulting ac moment

$$M_{\mathrm{ac}}(\omega, t) = M^{'} \sin(\omega, t) + M^{''} \cos(\omega, t) = H_{\mathrm{ac}}(\chi^{'} \sin(\omega, t) + \chi^{''} \cos(\omega, t)) \tag{3.3}$$

was measured, with $\chi^{'}$ being the real or in-phase component, and $\chi^{''}$ the imaginary or out-of-phase component of the complex susceptibility $\chi_{ac} = \chi^{'} + \mathrm{i}\chi^{''}$.

In the low frequency limit, $\chi^{'}$ corresponds to the differential susceptibility $\mathrm{d}M/\mathrm{d}H$, i.e. the slope of the magnetization $M(H)$. At higher frequencies, dynamic effects lead to a phase shift and differences between $\mathrm{d}M/\mathrm{d}H$ and $\chi^{'}$, where $\chi^{''}$ indicates dissipative processes such as eddy currents, relaxation processes or domain wall movements.

3.4.4 Specific Heat

In this thesis the specific heat was measured in the PPMS (see Sec. 3.4.1) by means of two techniques, namely a conventional small pulse technique and a quasi-adiabatic large pulse technique. In both cases the sample was coated with Apezion N grease and mounted on an $\mathrm{Al_2O_3}$ platform which supported also a resistive heater and a thermometer. Small platinum wires provided the electrical connection to the heater and the thermometer. They also provided the thermal link and structural support of the platform. The measurement was conducted under high vacuum such that the thermal link between the sample platform and the thermal bath was dominated by the wires. For the measurements, a heat pulse was applied with the heater and the temperature dependence, consisting of a heating and a cooling period, was measured as a function of time.

Fig. 3.16(a) shows a schematic illustration of the setup. The sample with a heat capacity C_s was coupled to a platform with a heat capacity C_p by means of a link with thermal conductance $\mathrm{K_s}$. The platform was coupled to the thermal bath at temperature $\mathrm{T_{bath}}$ by means of a link with thermal conductance $\mathrm{K_p}$. A heat pulse $P(t)$, shown in Fig. 3.16(c), was applied to the platform and the temperature response $\Delta T_\mathrm{p}(t)$ measured. Fig. 3.16(b) shows the simulated response of the temperature for the heat pulse shown in Fig. 3.16(c). The curve recorded was fitted with a model accounting for a relaxation between sample and platform as well as platform and bath, depending on the sample.

For the small pulse technique, a heat pulse between 0.1 % and 2 % of the sample temperature was applied. With the PPMS software the temperature response may be fitted by the one-tau model or the two-tau model. In the case of a perfect thermal link between sample and platform, the one-tau model yields the best fit results. The two-tau model is employed if the thermal link between sample and platform is finite. The specific heat of the sample is obtained by subtracting the specific heat of the empty setup, measured separately, from the total specific heat as determined from the fitting routine. Many small pulses are consecutively applied in order to determine the temperature dependence of the specific heat over a certain range.

For the quasi-adiabatic large pulse technique, a heat pulse of 30 % of the sample temperature is applied for a longer time. A perfect thermal link between the sample and the platform is assumed and the heating curve and the cooling curve are treated separately by the PPMS software with the one-tau model. Thereby it is possible to obtain directly a section of the $C(T)$ curve and hence the accuracy of the data and the speed of measurement was improved, as compared to the small pulse method. Unfortunately, analysis of large pulse data with the two-tau model is not implemented in the PPMS software.

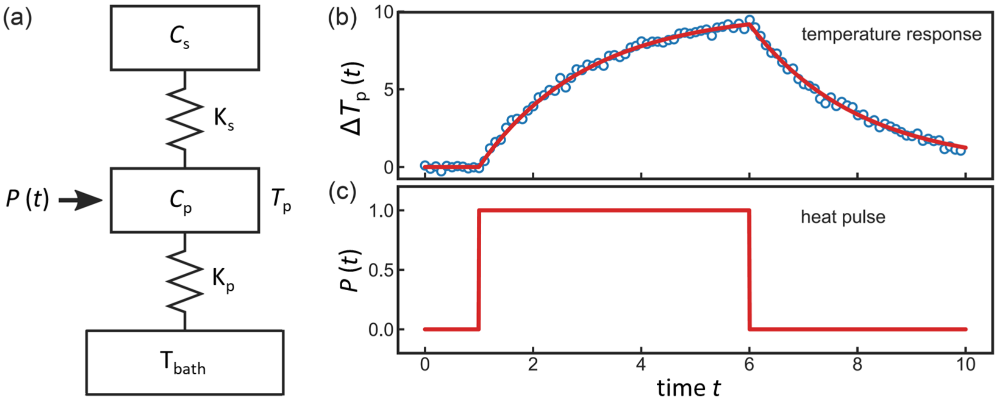

Figure 3.16: Specific heat measurement in the PPMS. (a) Schematic depiction of the setup. Sample with heat capacity C_s, thermal link $\mathrm{K_s}$, platform with heat capacity C_p, thermal link $\mathrm{K_p}$, bath with temperature $\mathrm{T_{bath}}$, heating pulse $P(t)$, platform temperature T_p. (b) Simulated temperature response $\Delta T_\mathrm{p}(t)$ (blue circles) and fit (red line). (c) Applied heat pulse $P(t)$. Figure from Ref. [129].

3.4.5 Electrical Transport

In this thesis, electrical resistivity and Hall effect measurements were conducted with a four-terminal or a six-terminal AC technique in the PPMS (see Sec. 3.4.1). The sample was mounted on a copper support with VGE-7031 varnish as insulated electrically by means of cigarette paper. Electrical contacts are realized by bonding $\mathrm{Al}_{99}\mathrm{Si}_1$ wires with a diameter of 25 µm connecting the sample with the terminals of a sample holder with a 53xx BDA-Ball-Deep-Access bonder (F & K Delvotec). Copper twisted pairs connect the terminals to the electrical wiring of the PPMS where the signals are detected with a setup involving lock-in amplifiers (Stanford Research Systems 830 or Signal Recovery 7230) combined with low-noise impedance-matching transformers (Signal Recovery Model 1900) with an amplification factor of $a = 100$. Excitation currents between 0.1 mA and 10 mA with a typical frequency of 22.08 Hz were applied by means of a current source (Keithley 6221). Alternatively, the built-in PPMS electrical transport option was used to generate the excitation currents and for signal detection.

The signal was converted to µΩ cm by multiplication with a geometry factor $(w \cdot d)/(\Delta_L \cdot a \cdot I)$ where w is the width, d the thickness, Δ_L the distance between the longitudinal contacts (see Fig. 3.17), a the amplification factor, and I the excitation current.

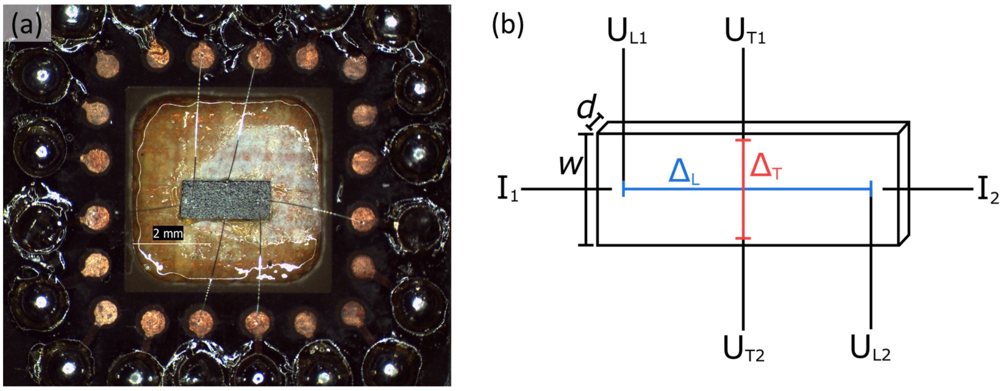

Figure 3.17: Sample contacts in an electrical transport measurement. (a) Photograph of an ErB_2 single-crystal with six $\mathrm{Al}_{99}\mathrm{Si}_1$ contacts. (b) Schematic depiction of sample geometry and nomenclature. The current is passed between I_1 and I_2, the longitudinal voltage is measured between contacts $\mathrm{U}_{\mathrm{L}1}$ and $\mathrm{U}_{\mathrm{L}2}$, the transverse voltage is measured between contacts $\mathrm{U}_{\mathrm{T}1}$ and $\mathrm{U}_{\mathrm{T}2}$.

If several independent scattering mechanisms are present, their contributions to the total resistivity may be summed up according to Matthiessens rule:

$$\rho(T) = \rho_0 + \rho_{\mathrm{phonon}} + \rho_{\mathrm{electron}} \tag{3.4}$$

where ρ_0, ρ_{phonon}, and ρ_{electron} are the resistivities induced by electron impurity and defect scattering, electron phonon scattering, and electron electron scattering, respectively. For $T \to 0$, the residual resistivity ρ_0 provides information on the quality and purity of the samples. The residual resistivity ratio RRR $= \rho_{\mathrm{highT}}/\rho_{\mathrm{lowT}}$, representing the ratio of the resistivity at high and low temperature, was determined. If not stated otherwise RRR $= \rho_{300\,\mathrm{K}}/\rho_{4.2\,\mathrm{K}}$ is given in this thesis.

CHAPTER 4

Low-Temperature Properties of CrB$_x$

This chapter reports the preparation of four ^{11}B-enriched CrB$_x$ single crystals with compositions $x = 1.90, 2.00, 2.05, 2.10$ with the optical floating zone method, followed by a characterization with x-ray Laue and powder diffraction and an investigation of the low-temperature properties by means of electrical resistivity and specific heat measurements. By varying the starting composition, the amount of B vacancies and the lattice parameters are expected to change. This addresses the influence of a defect structure and potential nuclear superstructure as well as the resistivity anomaly under pressure as discussed in Ref. [25].

The chapter is organized as follows. Sec. 4.1 reports the preparation of single crystals with different starting compositions in the high-pressure high-temperature optical floating zone furnace. The characterization by x-ray Laue and powder diffraction confirmed the formation of large single crystals with the space group $P6/mmm$ in all four float-zoned ingots and indicated lattice constants in close agreement with the literature. Sec. 4.2 presents electrical transport and specific heat measurements and reports the evolution of the residual resistivity ratios RRR and the antiferromagnetic transition temperatures $T_{\mathrm{N},\rho}$, as inferred from the resistivity, and $T_{\mathrm{N},C}$, as inferred from the specific heat, with the starting composition. Finally, Sec. 4.3 summarizes the results and gives an outlook on future studies of CrB$_x$.

4.1 Experimental Methods

This section describes the sample preparation and gives an overview on the methods used to determine the physical properties. First, the preparation of polycrystalline material is presented, followed by a description of the single crystal growth. Next, the post-growth characterization by x-ray Laue and powder diffraction is presented and an overview on the samples, the bulk properties, and the transport measurements, is given. We refer to Chap. 3 for details on the techniques and setups.

4.1.1 Preparation of Polycrystalline Material

Polycrystalline material of CrB_x with $x = 1.90$, 2.00, 2.05, 2.10 was prepared from 5N Cr granules (Alfa Aesar) and 5N B coarse powder (Alfa Aesar, 98 % ^{11}B enriched). Appropriate amounts of starting elements were weighed in and loaded into the arc melting furnace. After pumping down to 1×10^{-6} mbar, the synthesis was carried out by arc melting in a 9N argon atmosphere at ambient pressure. Each batch from the arc melting furnace weighed about 3 g and was homogenized by repeated cycles of melting, cooling and turning around.

Next, several of the 3 g ingots were loaded into the rod casting furnace. After pumping down to 5×10^{-7} mbar and subsequently flooding with 9N argon to 1.4 bar, the ingots were melted together and cast as starting rods with a diameter of 6 mm. With this procedure, we prepared two starting rods for each of the compositions studied, namely $x = 1.90$, 2.00, 2.05, 2.10.

4.1.2 Single Crystal Growth

The phase diagram of the B-Cr-system is depicted in Fig. 4.1. CrB_2, as marked in blue, melts congruently at a temperature of 2157 °C.

In this thesis, four single crystals of CrB_x with the compositions $x = 1.90$, 2.00, 2.05, 2.10 were prepared by means of the high-pressure high-temperature optical floating zone furnace (see Chap. 3).

As starting material rods with a diameter of 6 mm were prepared in the arc melting furnace and the rod casting furnace as described above. Each single crystal was prepared from two rods of the same composition under a high-purity argon atmosphere of 18 bar for $x = 1.90$, 2.00, 2.10, and 15 bar for $x = 2.05$. The growth speed in vertical direction was $5\,\mathrm{mm\,h^{-1}}$ and the flow rate of the argon atmosphere was $0.1\,\mathrm{l\,min^{-1}}$. Necking was applied at the beginning of the growth except for $x = 2.05$. Evaporation was observed during float-zoning but each growth could be conducted successfully. The float-zoned ingots for $x = 1.90$, 2.00, 2.05, 2.10 are depicted in Figs. 4.2(a) through (d).

Using x-ray Laue diffraction large single crystals with a length between 10 mm to 20 mm were confirmed in the float-zoned part of all four ingots. For instance, Figs. 4.2(e) and (f), show the Laue patterns of the ZA sample with $x = 2.00$ (see Sec 4.1.5 for an overview on the samples) along the crystallographic directions $\langle 100 \rangle$ and $\langle 001 \rangle$, respectively. The single crystal with $x = 2.05$ (HKZ6) was one of the first crystals prepared in the high-pressure high-temperature optical floating zone furnace. Similarly to the CoSi single crystal (HKZ7), described in Chap. 3, HKZ6 displayed a twisting of the crystallographic orientation by a few degrees along the length of the crystal. The crystals with $x = 1.90$ (HKZ14), 2.00 (HKZ15), 2.10 (HKZ17) were prepared after the optical configuration of the HKZ furnace had been significantly

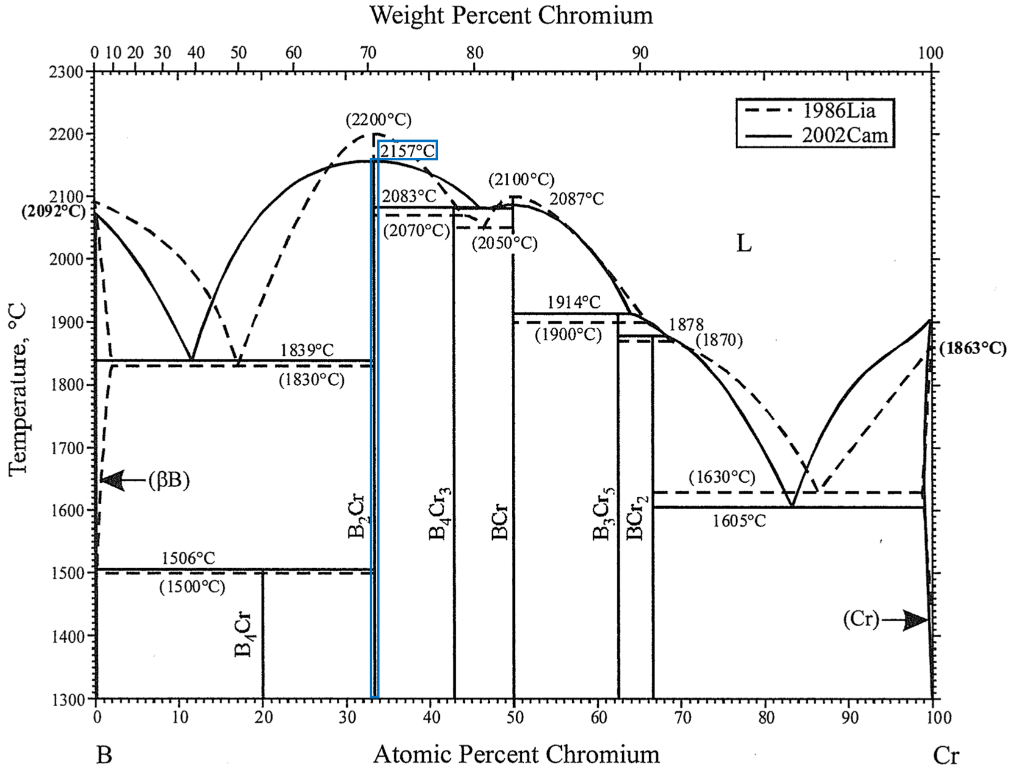

Figure 4.1: Binary phase diagram of the B-Cr-system. Congruently melting CrB_2 melts at 2157 °C and is marked in blue. Figure adapted from Ref. [42].

improved. They did not show a noticable change of the Laue patterns and their crystallographic orientation along the length of the single-crystal ingots.

4.1.3 Evaporation Losses

It has to be taken into account that both Cr and B exhibit evaporation at the melting temperature of 2157 °C of CrB_2, and it is very likely that the amounts of evaporated material differ for each element. In practice, it is very complicated to come up with an exact number since the amount of evaporated material at a certain temperature depends on many parameters including the time, the surface of the melt, the ambient pressure, the vapour pressures of the elements, as well as metallurgical and chemical processes.

Based on experience gained from the preparation of other diboride compounds, we estimate evaporation losses of about 5 % of the total mass during the preparation of polycrystalline material under inert gas pressures of about 1 bar. By applying significantly higher inert gas pressures of about 15 bar during the optical float-zoning, evaporation losses during the crystal growth were decreased to a minimum.

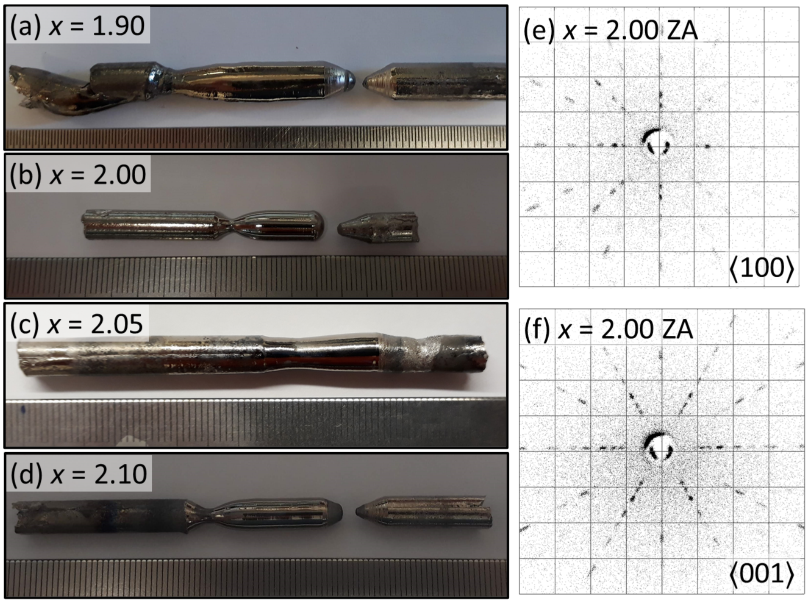

Figure 4.2: Float-zoned ingots and x-ray Laue patterns of CrB$_x$. (a) $x = 1.90$. (b) $x = 2.00$. (c) $x = 2.05$. (d) $x = 2.10$. The growth direction is from left to right. Note the absence of a pronounced neck in (c). (e), (f) Laue patterns of the ZA sample with $x = 2.00$ along the $\langle 100 \rangle$ and $\langle 001 \rangle$ direction, respectively.

4.1.4 X-Ray Powder Diffraction

Fine powders with 20 µm particle size were prepared by hand-grinding in an agate mortar and subsequent sieving. For each crystal, we prepared and investigated a powder sample made from a single-crystal piece from the beginning and the end of the ingot, labelled "ZA" and "ZE", respectively.

As an example, Fig. 4.3(a) shows the x-ray powder diffraction pattern of the ZA sample with $x = 2.00$ from the beginning of the stoichiometric crystal, recorded at room temperature in the Huber G670. A single phase Rietveld refinement with an R-factor $\mathrm{r}_{\mathrm{wp\ dash}} = 14$ confirms the hexagonal space group $P6/mmm$ and yields lattice constants of $a = 2.973\,\text{Å}$ and $c = 3.071\,\text{Å}$ in close agreement with the literature [31, 45].

Similar to the ZA sample with $x = 2.00$, we recorded diffraction patterns and performed Rietveld refinements for the other ZA and ZE samples with $x = 1.90$, 2.00, 2.05, 2.10. For all samples, the diffraction data show no indications for parasitic phases and the refinements confirm the space group $P6/mmm$. Figs. 4.3(b) and (c) show the dependence of the hexagonal lattice constants a and c on the B portion x in the studied range $1.90 \leq x \leq 2.10$ in CrB$_x$. Within the estimated margin of error of approximately 2×10^{-3} Å, denoted by the error bars, all samples show similar lattice constants and we detect no dependence on the boron portion x.

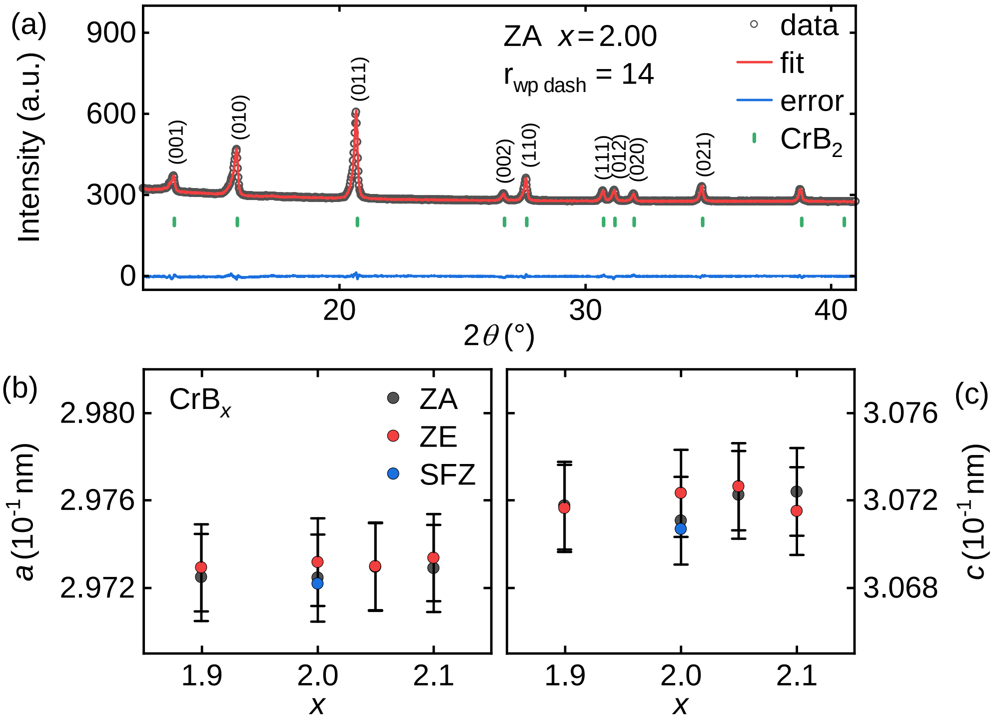

Figure 4.3: X-ray powder diffraction on CrB_x. (a) Pattern of the ZA sample with $x = 2.00$ with single phase Rietveld refinement. (b), (c) Lattice constants a and c of all CrB_x samples studied and of a single-crystal sample from Ref. [25], denoted with "SFZ", as a function of the B portion x.

In comparison, the application of pressure on stoichiometric CrB_2 has a significant influence on the lattice parameters [25]. As determined by x-ray powder diffraction, the lattice constants of the single-crystal sample "SFZ" are $a = 2.9722$ Å and $c = 3.0707$ Å at ambient pressure, in close agreement with our samples, as depicted in Figs. 4.3(b) and (c). The application of a pressure of 2.2 GPa leads to a decrease to $a = 2.9630$ Å and $c = 3.0154$ Å, corresponding to changes of $\Delta a \approx 9 \times 10^{-3}$ Å and $\Delta c \approx 6 \times 10^{-2}$ Å. These changes are accompanied by an anomaly in the electrical resistivity reminiscent of incipient superconductivity, observed for pressures above 2.2 GPa [25].

In this context, another system to consider is off-stoichiometric Nb_xB_2 [39]. Interestingly, in this compound, a metastable superconducting phase was reported for $0.67 \leq x \leq 1.11$ in samples prepared by combustion synthesis. The lattice dimensions of those samples vary by $\Delta a \approx 1 \times 10^{-2}$ Å and $\Delta c \approx 3 \times 10^{-2}$ Å in the range $0.95 \leq x \leq 1.05$. Since these compositions are equivalent to the compositional range of $1.90 \leq x \leq 2.10$ in CrB_x, a similar change of the lattice dimensions may be expected. The lack of a measurable change is probably due to the preparation by the floating zone method, which promotes the crystallization of stoichiometric CrB_2

independent from off-stoichiometric starting compositions that deviate from CrB_2 by a comparably small margin. To resolve this issue we propose the preparation of CrB_x with $1.90 \leq x \leq 2.10$ using e.g. high-temperature high-pressure elemental synthesis combined with argon annealing [66], followed by a determination of the lattice constants.

4.1.5 Samples for Physical Properties

For the measurements of the physical properties small pieces were cut with a diamond wire saw and the orientation confirmed with x-ray Laue diffraction. From each of the four crystals with $x = 1.90$, 2.00, 2.05, 2.10, a set of samples was cut from the beginning and the end, labelled "ZA" and "ZE", respectively. Each set consisted of three samples, namely:

1. A small cuboid measuring $2.5 \times 2.2 \times 1$ mm^3 with orientation along $\langle 001\rangle \times \langle 100\rangle \times \langle 210\rangle$ for specific heat measurements.
2. A thin platelet measuring $2 \times 1 \times 0.2$ mm^3 with orientation along $\langle 001\rangle \times \langle 210\rangle \times \langle 100\rangle$ for measurements of the electrical resistivity.
3. A cube with a mass of approximately 30 mg that was ground to fine powder for the diffraction studies presented above.

The temperature dependence of both the electrical resistivity and the specific heat was recorded in a Quantum Design PPMS in the temperature range from 2 K to 350 K in zero magnetic field.

4.2 Low-Temperature Properties

This section is organized as follows. We start with the zero-field electrical resistivity data for current along the $\langle 001\rangle$ direction of ZA and ZE samples for all compositions. The data show qualitatively similar behaviour and a good agreement with the SFZ samples from Refs. [24, 25, 31]. A distinct kink indicates the transition to antiferromagnetic order at $T_{\mathrm{N},\rho}$. For the crystals with $x = 1.90$, 2.05, 2.10, RRR and $T_{\mathrm{N},\rho}$ values from the ZA and ZE sample are in agreement within experimental uncertainty. For the stoichiometric composition $x = 2.00$, the values of the RRR and $T_{\mathrm{N},\rho}$ of the ZA sample are both smaller than the corresponding values of the ZE sample.

Next we present the zero-field heat capacity measurements of ZA and ZE samples for all four compositions. In agreement with the electrical resistivity, all data show qualitatively similar behaviour and a good agreement with the properties of the SFZ samples reported in Refs. [24, 25, 31]. A clear lambda anomaly at $T_{\mathrm{N},C}$ indicates the onset of long-range antiferromagnetic order. Within experimental uncertainty, values of $T_{\mathrm{N},C}$ and $T_{\mathrm{N},\rho}$ are in agreement for each sample. We refer to Tab. 4.1 for an overview on the parameters inferred from the bulk property measurements.

4.2.1 Electrical Resistivity of CrB$_x$

Figs. 4.4(a) and (b) show the temperature dependence of the zero-field electrical resistivity for current along the $\langle 001 \rangle$ direction of CrB$_x$ samples ZA and ZE, of the beginning and the end of the crystals, respectively. Typical for a metallic state, the residual resistivities are in the $\mu\Omega\,\mathrm{cm}$ range. For the crystals with $x = 1.90$, 2.05, 2.10, the residual resistivity ratios RRR=$\rho_{300\,\mathrm{K}}/\rho_{4.2\,\mathrm{K}}$ of the ZA and ZE samples are in good agreement, corroborating the results from the x-ray diffraction characteristic of a uniform crystalline quality of the float-zoned ingots. The crystal with $x = 2.05$ displays the lowest RRR of about 11 consistent with the problems observed during growth, i.e. the rotation of the crystallographic orientation by a few degree along the length of the crystal. Such a rotation would be consistent with reduced crystalline quality. For the stoichiometric crystal with $x = 2.00$, the RRR of the ZE sample is approximately three times larger than the RRR of the ZA sample, pointing to a higher quality and purity of the ZE sample. Our best samples display RRR values of about 30, similar to the stoichiometric SFZ samples from Refs. [24, 25, 31].

All curves in Figs. 4.4(a) and (b) display qualitatively similar behaviour. With increasing temperature, the resistivity increases monotonically with a positive curvature up to a kink indicating the antiferromagnetic transition temperature $T_{\mathrm{N},\rho}$, as denoted by the black arrow. Above $T_{\mathrm{N},\rho}$, the resistivity increases further with a negative curvature up to the highest temperatures measured.

Figs. 4.4(c) and (d) show a close-up view of the temperature dependence of the derivative of the electrical resistivity with respect to the temperature $\mathrm{d}\rho/\mathrm{d}T$ in the regime of the antiferromagnetic transition. With increasing temperature, $\mathrm{d}\rho/\mathrm{d}T$ exhibits a maximum, followed by an abrupt decrease indicating the transition, before flattening out for further increasing temperatures. We ascribe $T_{\mathrm{N},\rho}$ to the midpoint of the decrease in the spirit of the entropy-conserving construction used in the specific heat data presented below. The transition temperatures are marked with coloured arrows where we estimate an uncertainty $\Delta T_{\mathrm{N},\rho} \approx 0.5\,\mathrm{K}$.

For the crystals with $x = 1.90$, 2.05, 2.10, the values of $T_{\mathrm{N},\rho}$ of the ZA and ZE samples are in good agreement. In contrast, for $x = 2.00$ $T_{\mathrm{N},\rho}$ of the ZA sample is smaller than $T_{\mathrm{N},\rho}$ of the ZE sample. This behaviour of the transition temperatures $T_{\mathrm{N},\rho}$ is similar to the behaviour of the RRR discussed above. Overall, we observe that a RRR $\gtrapprox 23$ indicates a $T_{\mathrm{N},\rho}$ close to 88.5 K in agreement with the SFZ samples that display similarly high RRR and transition temperatures. In contrast, the samples with RRR ≈ 11 show $T_{\mathrm{N},\rho} < 88.5\,\mathrm{K}$. We refer to Tab. 4.1 for an overview on the parameters inferred from the resistivity measurements.

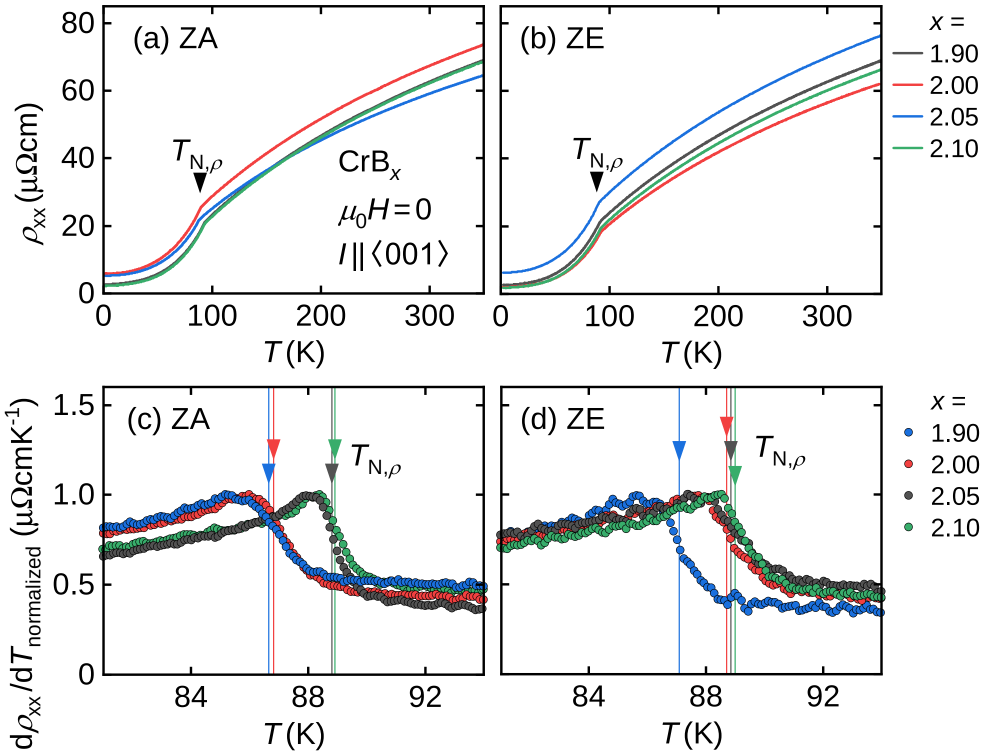

Figure 4.4: Temperature dependence of the electrical resistivity of CrB$_x$ in zero field. (a), (b) Zero-field resistivity of the ZA and ZE samples from the beginning and the end of the float-zoned ingots, respectively. A kink indicates the antiferromagnetic transition temperatures $T_{N,\rho}$, marked with the black arrow. (c), (d) Close-up view of the derivative of the electrical resistivity by the temperature for ZA and ZE samples in the regime of the phase transition, respectively. The coloured arrows mark the transition temperatures $T_{N,\rho}$ for each sample.

4.2.2 Specific Heat of CrB$_x$

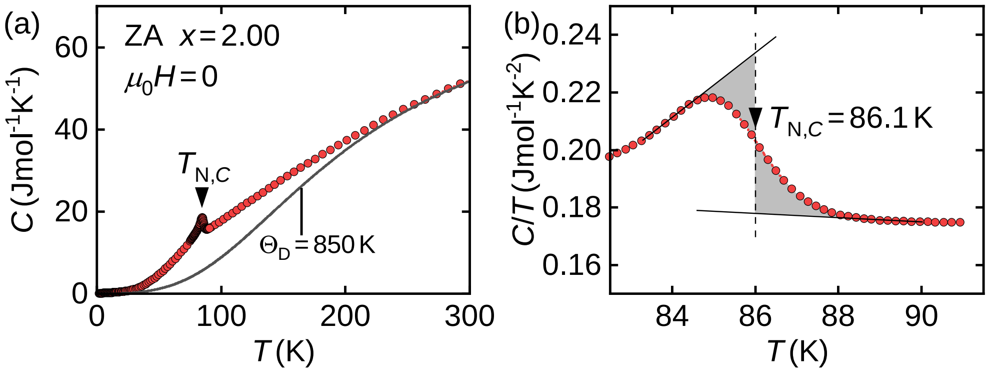

Figure 4.5: Temperature dependence of the specific heat of the ZA sample with $x = 2.00$ in zero field. (a) Specific heat of the ZA sample with $x = 2.00$ (red dots) and Debye model (grey line). A clear lambda anomaly indicates the antiferromagnetic transition $T_{\mathrm{N},C}$, marked with the black arrow. (b) Close-up view of the specific heat divided by the temperature. An entropy-conserving construction yields the transition temperature $T_{\mathrm{N},C} = 86.1\,\mathrm{K}$.

Fig. 4.5(a) shows the temperature dependence of the specific heat of the ZA sample with $x = 2.00$ measured in zero magnetic field. At high temperatures, the Dulong-Petit limit of $74.83\,\mathrm{J\,mol^{-1}\,K^{-1}}$ is approached. A numeric evaluation of the Debye model with $\Theta_{\mathrm{Debye}} = 850\,\mathrm{K}$, depicted by the grey line, shows deviations from the specific heat at low temperatures but approaches the measured curve with increasing temperature. This agrees with Refs. [24, 25, 31] which report that a simple Debye fit is not suitable to treat the lattice dynamics in CrB$_2$, similar to other transition-metal and rare-earth diborides [31, 35, 37]. Marked by the black arrow is the lambda anomaly at $T_{\mathrm{N},C} = 86.1\,\mathrm{K}$, at the onset of long-range antiferromagnetic order. The transition temperature may be extracted with the help of an entropy-conserving construction, as depicted in Fig. 4.5(b) which shows a detailed view of the specific heat divided by temperature in the region of the phase transition. An uncertainty of $\Delta T_{\mathrm{N},C} \approx 0.5\,\mathrm{K}$ in the determination of the transition temperature is estimated.

Similar to the ZA sample with $x = 2.00$, the specific heat of the other ZA and ZE samples with $x = 1.90, 2.00, 2.05, 2.10$ was measured. The data show qualitatively similar behaviour and agree with the SFZ samples from Refs. [24, 25, 31]. Figs. 4.6(a) and (b) show a close-up view of the temperature dependence of the specific heat divided by the temperature for the ZA and ZE samples, respectively. As depicted in Fig. 4.5(b) for the ZA sample with $x = 2.00$, $T_{\mathrm{N},C}$ is extracted with an entropy-conserving construction. The transition temperatures are marked with coloured arrows and we estimate an uncertainty of $\Delta T_{\mathrm{N},C} \approx 0.5\,\mathrm{K}$ in determining $T_{\mathrm{N},C}$. For all samples, the values of $T_{\mathrm{N},C}$ and $T_{\mathrm{N},\rho}$ coincide within experimental uncertainty.

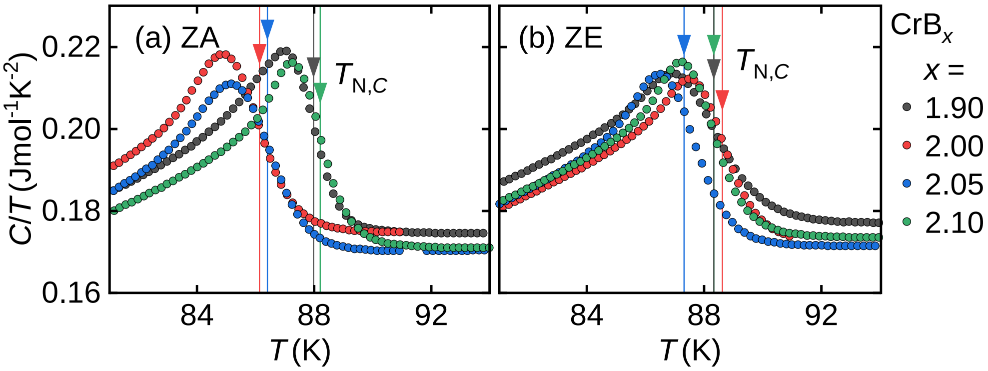

Figure 4.6: Close-up view of the temperature dependence of the specific heat divided by the temperature in CrB$_x$. (a), (b) ZA and ZE samples from the beginning and the end of the float-zoned ingots, respectively. The coloured arrows mark the transition temperatures $T_{N,C}$ for each sample.

We refer to Tab. 4.1 for an overview on the transition temperatures extracted from the specific heat.

Table 4.1: Residual resistivity ratios (RRR) and transition temperatures of CrB$_x$ as observed in the electrical resistivity and the specific heat, denoted with $T_{N,\rho}$ and $T_{N,C}$, respectively. RRR denotes the resistivity at 300 K, $\rho_{300\,K}$, divided by the resistivity at 4.2 K, $\rho_{4.2\,K}$. Only for the SFZ162 sample, the RRR denotes the resistivity at 294 K divided by the resistivity at 5 K. We estimate an uncertainty of 0.5 K for both $T_{N,\rho}$ and $T_{N,C}$.

Sample	$\rho_{300(294)\,K}$ (μΩ cm)	$\rho_{4.2(5)\,K}$ (μΩ cm)	RRR	$T_{N,\rho}$ (K)	$T_{N,C}$ (K)
CrB$_2$-SFZ162	63.2	2.0	32.0	88.9	
CrB$_{1.9}$-ZA	62.7	2.7	23.2	88.8	88.0
CrB$_{1.9}$-ZE	62.6	2.6	24.1	88.9	88.3
CrB$_2$-ZA	67.4	5.9	11.4	86.8	86.1
CrB$_2$-ZE	56.5	2.0	28.3	88.7	88.6
CrB$_{2.05}$-ZA	59.1	5.3	11.2	86.6	86.4
CrB$_{2.05}$-ZE	70.0	6.3	11.1	87.1	87.3
CrB$_{2.1}$-ZA	62.2	2.3	27.0	88.9	88.2
CrB$_{2.1}$-ZE	60.1	1.8	33.4	89.0	88.3

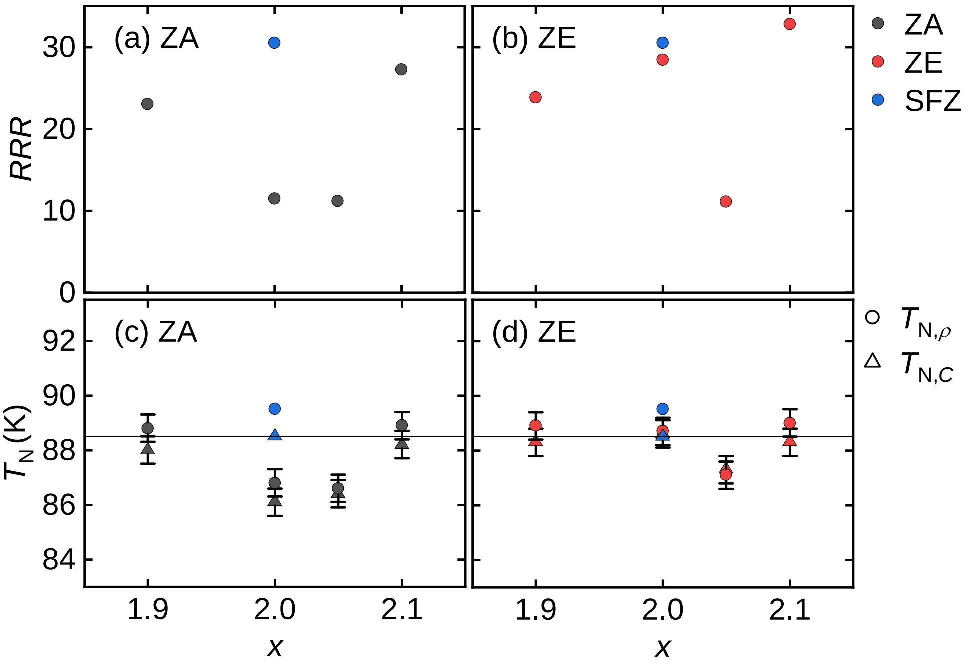

Figure 4.7: RRR and transition temperatures as a function of the B portion x in CrB_x. (a), (b) Values of the RRR for ZA and ZE samples, respectively. (c), (d) Values of the transition temperatures $T_{N,\rho}$ and $T_{N,C}$ for the ZA and ZE samples, respectively. The temperature of 88.5 K is marked by the horizontal black line. Data for the single crystal SFZ118 were extracted from Refs. [24, 25, 31].

4.3 Conclusions

In summary, four ^{11}B-enriched single crystals of CrB$_x$ with compositions $x = 1.90$, 2.00, 2.05, 2.10 were prepared using the high-pressure high-temperature optical floating zone furnace that was set-up and commissioned as part of this thesis. X-ray Laue diffraction confirms the presence of large single-crystal grains consistent with the hexagonal space group $P6/mmm$. Rietveld refinements of x-ray powder diffraction patterns from the beginning and the end of each crystal indicate single-phase samples with lattice constants in close agreement to the literature, and similar lattice constants for all samples.

Measurements of the electrical resistivity display metallic behaviour with small residual resistivities. Apart from the stoichiometric crystal with $x = 2.00$, ZA and ZE samples show similar values of the RRR, pointing to a uniform crystalline quality of the ingots. The ZA and ZE samples from the stoichiometric crystal with $x = 2.00$ display RRR values of 11.4 and 28.3, respectively, indicating a reduced quality of the ZA sample from the beginning of the crystal. In agreement with Refs. [24, 25, 31] our best samples show a RRR of about 30.

Starting at $x = 1.90$, with increasing x, the RRR of the ZA samples display a decrease followed by an increase to the highest RRR of 33.4 in the sample with $x = 2.10$. When regarding the same for the ZE samples, the RRR display a slight increase, followed by a decrease, followed by an increase to the highest RRR of 27.0 in the sample with $x = 2.10$. This observation suggests that crystals with further increased B portion $x > 2.10$ might yield even higher RRR values.

The transition to antiferromagnetic order exhibits a kink in the electrical resistivity at $T_{\mathrm{N},\rho}$. Values of $T_{\mathrm{N},\rho}$ were determined from the derivative of the electrical resistivity with respect to the temperature. The specific heat exhibits a lambda anomaly at the antiferromagnetic transition in all samples studied. The exact values of $T_{\mathrm{N},C}$ were determined using an entropy-conserving construction. Regardless of whether the samples were cut from the beginning or the end of the crystals, we observe that the samples with RRR $\gtrapprox 23$ display $T_{\mathrm{N},\rho} \approx T_{\mathrm{N},C} \approx 88.5\,\mathrm{K}$, whereas the samples with RRR ≈ 11 show $T_{\mathrm{N},\rho} \approx T_{\mathrm{N},C} < 88.5\,\mathrm{K}$. A reduced RRR is accompanied by decreased values of the transition temperatures.

The reported work serves as a basis for further investigations of the four prepared crystals by neutron scattering in pursuit of the defect structure and nuclear superstructure. Beam time at the diffractometer RESI at the Heinz Maier-Leibnitz Zentrum (MLZ) in Garching has been allocated and neutron diffraction measurements will be carried out in the near future. The use of neutrons as a microscopic probe will yield a deeper understanding of the metallurgical nature of CrB$_2$ and the hexagonal diborides in general. Furthermore, the preparation of crystals with further increased boron portion might result in even higher RRR values, potentially indicating a lower amount of B vacancies. In turn, neutron studies on the four crystals presented above as well as future crystals with $x > 2.10$ might reveal the influence of a defect structure and potential nuclear superstructure on the magnetic properties of CrB$_2$.

CHAPTER 5

Easy-Plane Antiferromagnetism in Single-Crystal ErB_2

This chapter reports the preparation of a high-purity ^{11}B-enriched ErB_2 single crystal by means of self-adjusted flux travelling solvent float-zoning in the high-pressure high-temperature floating zone furnace. The preparation route established here for large single crystals of ErB_2 may be applied to prepare rare-earth sibling compounds (e.g. DyB_2, HoB_2) and ultimately allows for a comprehensive characterization of the magnetic properties at low temperatures in this insufficiently studied class of materials. In particular, detailed investigations with regards to complex magnetic textures with non-trivial topology and the role of disorder paired with strong electronic correlations are now made possible.

This chapter is organized as follows. Sec. 5.1 comprises information on the metallurgy of incongruently melting ErB_2 and reports the preparation of polycrystalline material and a high-purity single crystal with the optical floating zone technique. Subsequently, the characterization by x-ray Laue and powder diffraction is presented, followed by an overview about samples and experimental methods. Next, Sec. 5.2 reports the measurements of the ac susceptibility, magnetization, specific heat, and electrical resistivity that identify easy-plane antiferromagnetic order below $T_N = 13.9\,\mathrm{K}$. We observe a strong ferromagnetic coupling along the easy in-plane directions $\langle 100 \rangle$ and $\langle 210 \rangle$ and a weak antiferromagnetic coupling along the hard out-of-plane direction $\langle 001 \rangle$. The strong magnetocrystalline anisotropy is corroborated by a spin-flip transition at $4\,\mathrm{K}$ under an applied field of $B_s = 11.8\,\mathrm{T}$ along the hard magnetic axis $\langle 001 \rangle$. Based on the magnetization and ac susceptibility measurements magnetic phase diagrams for field along the easy axis $\langle 100 \rangle$ and hard axis $\langle 001 \rangle$ are presented. We extract residual resistivity ratios of $\mathrm{RRR}_{\langle 100 \rangle} = 6$ and $\mathrm{RRR}_{\langle 001 \rangle} = 5.5$ and a charge carrier concentration of $n = 2.41 \times 10^{32}\,\mathrm{m}^{-3}$, a value typical for electron conduction in a good metal. Finally, Sec. 5.3 summarizes the results and gives an outlook on future studies of ErB_2 and other rare-earth diborides.

5.1 Experimental Methods

The following section describes the sample preparation and presents the experimental methods. First, the preparation of polycrystalline ErB_2 and a high-purity single crystal by means of self-adjusted flux travelling solvent float-zoning is described. Subsequently, the characterization by x-ray Laue and powder diffraction is presented, followed by an overview about the samples. Finally demagnetization and remanent field effects are discussed. For details on the applied techniques and setups we refer to Chap. 3.

5.1.1 Preparation of Polycrystalline Material

Small, polycrystalline samples of TmB_2, DyB_2, HoB_2, and ErB_2 were prepared from 4N Tm, Dy, Ho, and Er pieces (Smart Elements) and 5N B coarse powder (Alfa Aesar, 98 % ^{11}B enriched). Stoichiometric amounts of rare-earth metals were prepared for further processing in the argon glovebox. Stoichiometric amounts of B were weighed and transferred into the glovebox. The arc melting furnace was docked to the glovebox and the starting material was loaded into the furnace. After pumping to 1×10^{-6} mbar, the synthesis was carried out by arc melting in a 9N argon atmosphere at ambient pressure. Several cycles of melting, cooling, and turning around the ingots to improve their homogeneity were repeated.

By means of x-ray powder diffraction, we identified a target phase percentage of approximately 95 % in the DyB_2, HoB_2, and ErB_2, and of approximately 70 % in the TmB_2 sample, the latter being presumably linked to large evaporative losses during preparation. To check for magnetic transitions, the temperature dependence of the real part of the ac susceptibility of the arc-melted samples of DyB_2, HoB_2, and ErB_2 was recorded in zero magnetic field, as displayed in Figs. 5.1(a) through (c). The DyB_2 sample in Fig. 5.1(a) shows anomalies at $T_{c1} \approx 47\,\mathrm{K}$ and $T_{c2} \approx 180\,\mathrm{K}$, in agreement with the literature [26, 36]. Two additional anomalies, probably due to parasitic phases, are indicated by red arrows. The samples of both HoB_2 and ErB_2 shown in Fig. 5.1 (b) and (c) displayed one anomaly at $T_c \approx 12\,\mathrm{K}$ and $T_c \approx 14\,\mathrm{K}$, respectively, in agreement with the literature [26, 67, 68].

Taken together, we established the three compounds DyB_2, HoB_2, and ErB_2 as the most suitable candidates for the preparation of single crystals by optical float-zoning. In the next section, we give an account on the preparation of the ErB_2 single crystal.

5.1.2 Single Crystal Growth

In a first attempt to grow a single crystal, ErB_2 was chosen due to its favourable metallurgical properties as described in the following. All three compounds DyB_2, HoB_2, and ErB_2 are reported to melt incongruently [42, 130], but for ErB_2, the difference in composition between a composition of equilibrium and the stoichiometric composition of ErB_2 is the smallest. Hence, ErB_2 entails the best chances for preparing a single crystal with the self-adjusted flux travelling solvent optical floating

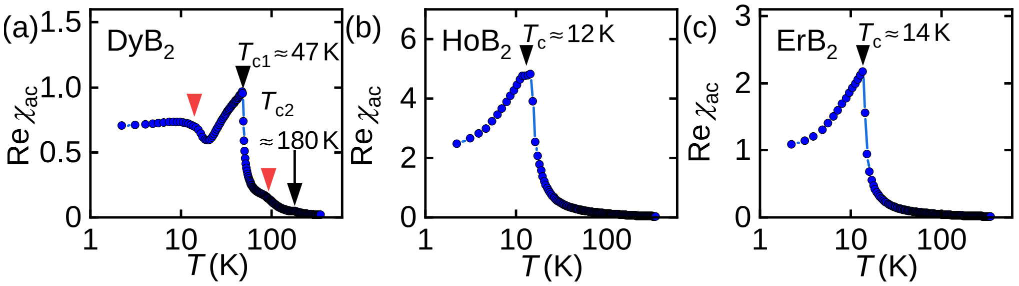

Figure 5.1: Temperature dependence of the real part of the zero-field ac susceptibility of arc-melted polycrystalline samples of rare-earth diborides. Anomalies indicating phase transitions are labelled and marked with coloured arrows. (a) - (c) DyB_2, HoB_2, and ErB_2.

zone technique.

The phase diagram of the B-Er-system is depicted in Fig. 5.2. The incongruently melting phase ErB_2, marked in blue, is in equilibrium with the liquid at a temperature of 2185 °C. When lowering the temperature of a melt with composition ErB_2, ErB_4 starts to solidify at approximately 2200 °C at point A, marked in purple. When further lowering the temperature, the concentration of the melt changes along the cyan-coloured arrow to 65 % Er at point B, marked in green, where ErB_2 starts to crystallize. Due to the small difference in concentration between point A and B, the self-adjusted flux travelling solvent floating zone (TSFZ) method was applied to prepare a single crystal of ErB_2 in the high-pressure high-temperature optical floating zone furnace (see Chap. 3).

As starting material for the single crystal several small ingots each consisting of approximately 3 g of polycrystalline stoichiometric ErB_2 were prepared as described above. In the next step several of these ingots were combined to form rod-like ingots by welding them together in the arc melting furnace. The single crystal was prepared from two of these rod-like ingots as depicted in Fig. 5.3(a). The growth was conducted in the high-pressure high-temperature optical floating zone furnace under 18 bar of high-purity argon and a continuous flow of $0.1\,\mathrm{l\,min^{-1}}$. The seed and the feed rod were counter rotated with $10\,\mathrm{min^{-1}}$. In order to keep the volume of the molten zone as constant as possible no necking was applied. The growth was started immediately with a speed of $3\,\mathrm{mm\,h^{-1}}$ in vertical direction after forming the molten zone. After a growth length of approximately 20 mm the zone was quenched. The float-zoned ingot was checked with x-ray Laue diffraction. Although evaporation was observed during the float-zoning, this first attempt resulted in a successful grain selection and the growth of single-crystal ErB_2.

The float-zoned ingot is depicted in Fig. 5.3(b), the single crystal is marked by the red box and labelled with "ZE". Figs. 5.3(c) and (d) show x-ray Laue diffraction patterns of the $\langle 100 \rangle$ and $\langle 001 \rangle$ direction, respectively, taken on different sides of the ingot, confirming the single-crystal quality consistent with the hexagonal space

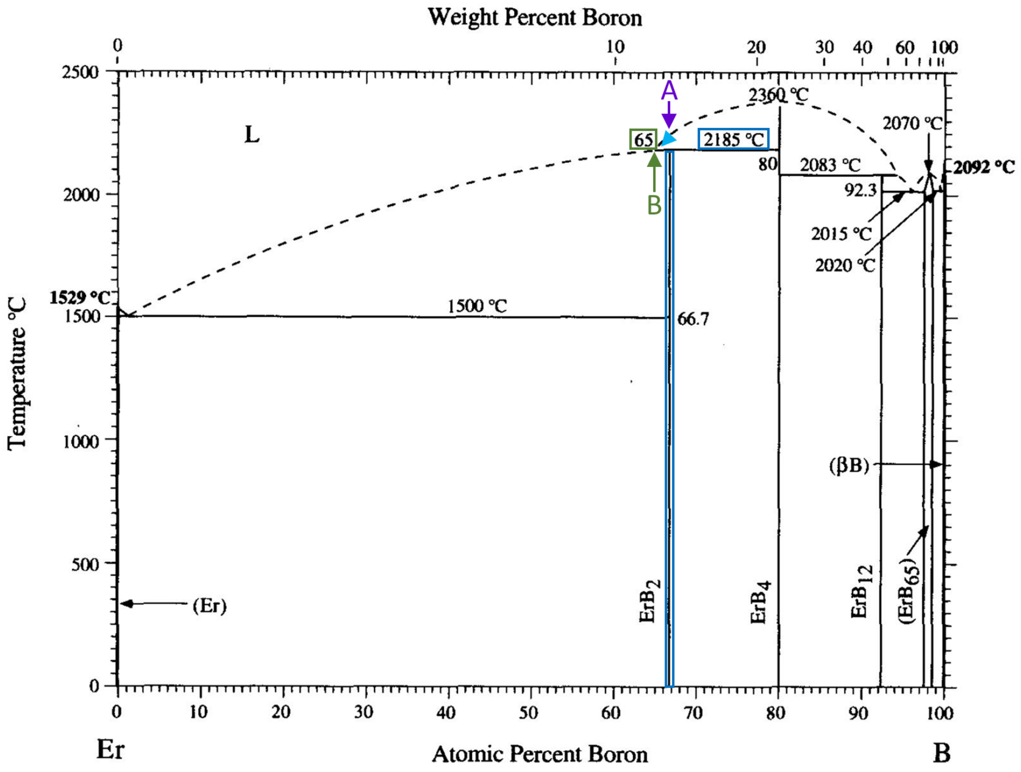

Figure 5.2: Binary phase diagram of the B-Er-system. The incongruently melting compound ErB_2 with a melting temperature of 2185 °C is marked in blue. At point A, marked in purple, ErB_4 starts to solidify from a melt with a composition of ErB_2. Point B in green marks the crystallization of ErB_2 from a melt with a concentration of 65 % Er. Figure adapted from Ref. [130].

group $P6/mmm$ of ErB_2.

Fig. 5.3(e) shows an x-ray powder diffraction pattern of single-crystal ErB_2 recorded at room temperature in the Huber G670. The powder was prepared by hand-grinding in an agate mortar from a single-crystal piece and subsequently sieved to 20 µm particle size. The diffraction data are well fitted by a Rietveld refinement with space group $P6/mmm$ yielding lattice constants $a = 3.275$ Å and $c = 3.784$ Å in good agreement with the literature [130].

5.1.3 Samples for Physical Properties

From the single-crystal ingot, smaller samples were cut with a diamond wire saw. The crystallographic orientation of the samples was determined by means of x-ray Laue diffraction. A small cuboid of $2.5 \times 1.4 \times 1\ \text{mm}^3$ orientated along $\langle 001\rangle \times \langle 100\rangle \times \langle 210\rangle$ was cut for ac susceptibility, magnetization, and specific heat measurements. Adjacent

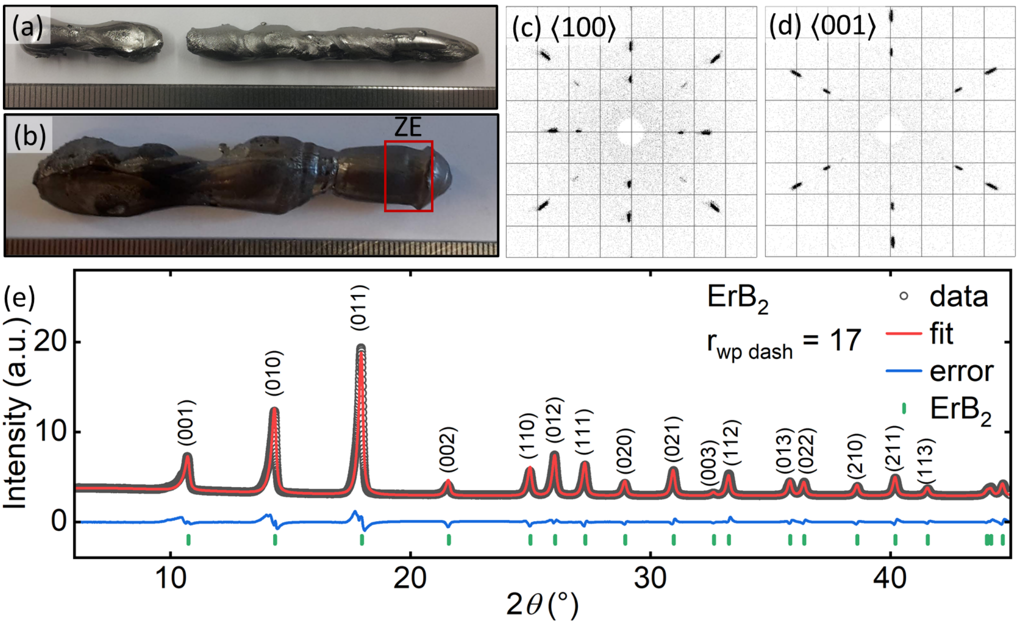

Figure 5.3: Single crystal growth and characterization of ErB_2. (a) Photograph of polycrystalline ErB_2 starting material. (b) Photograph of the float-zoned ErB_2 ingot. The single-crystal part is marked by the red box and labelled with "ZE". (c), (d) X-ray Laue diffraction pictures of the ⟨100⟩ and ⟨001⟩ direction. (e) X-ray powder diffraction pattern with Rietveld refinement. The powder was prepared from a single-crystal piece.

to that slab, another sample was cut for the preparation of powder for the x-ray powder diffraction measurements presented above. Furthermore, two platelets were cut, $2 \times 1 \times 0.2\ \mathrm{mm}^3$ and $1.2 \times 1 \times 0.2\ \mathrm{mm}^3$ oriented along $\langle 001\rangle \times \langle 210\rangle \times \langle 100\rangle$ and $\langle 100\rangle \times \langle 210\rangle \times \langle 001\rangle$, respectively, for measurements of the electrical resistivity and Hall effect.

The bulk and transport properties were measured in a Quantum Design PPMS and a Oxford Instruments VSM. The magnetization and ac susceptibility using an excitation $\mu_0 H_{\mathrm{ac}} = 1\,\mathrm{mT}$ and a frequency $f = 1000\,\mathrm{Hz}$ was determined in the temperature range from 2 K to 350 K under magnetic fields up to 14 T. Additionally, the temperature dependence of the specific heat in zero field and the electrical resistivity in fields up to 9 T were recorded. The temperature and field dependence of both the magnetization and ac susceptibility was measured after zero-field cooling and field-cooling, respectively. At the lowest temperature measured, namely 2 K and 4 K for magnetic field along ⟨100⟩ and ⟨001⟩, respectively, the field dependence was measured after zero-field cooling and a full five-point hysteresis loop was recorded for both directions.

For measurements of the magnetization and ac susceptibility in fields applied along the ⟨001⟩ direction we used a bespoke sample holder to prevent the sample from turning towards one of the easy directions ⟨100⟩ or ⟨210⟩. However, the large anisotropy between the hard axis ⟨001⟩ and the easy plane ⟨100⟩×⟨210⟩ resulted in a bending of the sample holder in high fields due to torque. This lead to an increase in temperature due to friction during the measurement of the field dependence of the magnetization and ac susceptibility for field along ⟨001⟩ at low temperatures. Measurements on a smaller sample which produces a smaller torque in high magnetic fields and hence allows for a stable temperature could not be completed during this thesis.

5.1.4 Remanent Field and Demagnetization Effects

Measurements of the magnetization and ac susceptibility in the Quantum Design PPMS with the 14 T superconducting magnet may be subject to remanent fields of up to approximately 10 mT. This is illustrated in Fig. 5.4 which shows the field dependence of the magnetization for increasing and decreasing fields along ⟨100⟩. The data was recorded after the superconducting magnet had been ramped to the maximum field of 14 T. This lead to a remanent field of about 10 mT at zero field. Similarly, a remanent field of about −10 mT was observed for increasing the field from −14 T. The field dependence of the magnetization presented below was corrected for this remanent field.

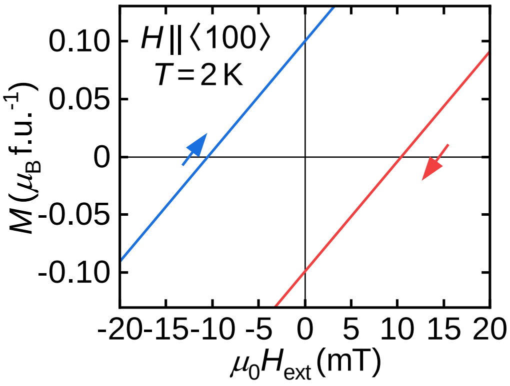

Figure 5.4: Field dependence of the magnetization at 2 K for field along the easy axis ⟨100⟩. The magnetization for increasing and decreasing field is coloured in blue and red, respectively.

To determine the demagnetization factors the cuboid sample was approximated as a rectangular prism with dimensions $2.5 \times 1.5 \times 0.96$ mm^3 and the factors were calculated from an analytic expression according to Ref. [132]. The resulting demagnetization factors were $D_{\langle 100 \rangle} = 0.32$ and $D_{\langle 001 \rangle} = 0.19$ for magnetic fields along the ⟨100⟩ and ⟨001⟩ direction, respectively.

The magnetization and susceptibility data shown below are presented as measured, i.e. as a function of the applied field. In the phase diagrams demagnetization effects were corrected. For comparison, the effect of the demagnetizing field on the measured data is illustrated in Fig. 5.5 which shows the field dependence of the magnetization at 2 K as a function of the external (black curve) and internal (red curve) field along the ⟨100⟩ direction. Applying the demagnetization correction leads to a compression of the field scale as can be seen by the change of slope between $M(H_{\mathrm{ext}})$ and $M(H_{\mathrm{int}})$.

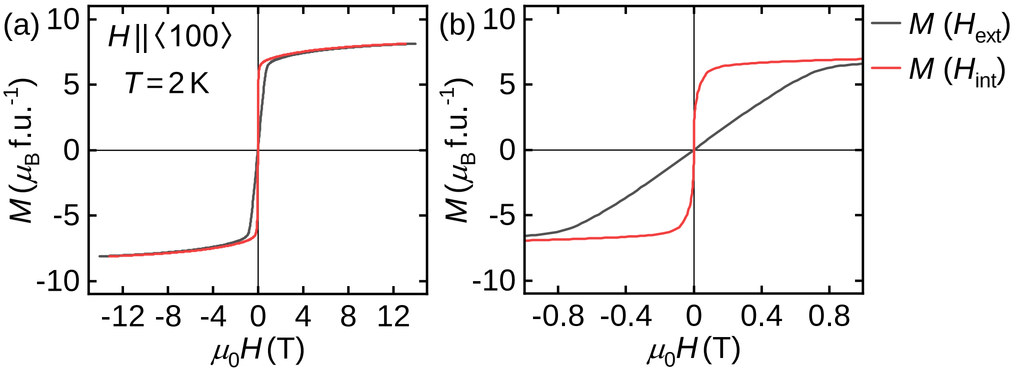

Figure 5.5: Illustration of demagnetization effects in single-crystal $\mathrm{ErB_2}$ for magnetic fields along ⟨100⟩. (a) Magnetization as a function of the external (black curve) and internal (red curve) field. (b) Close-up view in the range from -1 T to 1 T.

5.2 Characterization

This section is organized as follows. The real part of the zero-field ac susceptibility for the major crystallographic directions ⟨100⟩, ⟨210⟩, and ⟨001⟩ are presented first. The measurements indicate a low-temperature transition to an antiferromagnetic state below $T_N = 13.9$ K with a strong magnetocrystalline anisotropy between the easy plane ⟨100⟩ × ⟨210⟩ and the hard out-of-plane direction ⟨001⟩. Within the easy plane ferromagnetic interactions dominate, whereas characteristics of antiferromagnetic interactions along the hard out-of-plane direction are observed. Next magnetization and ac susceptibility measurements for magnetic fields along the easy axis ⟨100⟩ and the hard axis ⟨001⟩ are presented, summarized in forms of an internal field vs. temperature phase diagram. The data reveal additional crossover temperatures as well as a spin-flip transition at 4 K in a field of 11.8 T applied along the hard axis ⟨001⟩. This is followed by the zero-field specific heat which displays a distinct lambda anomaly at T_N and two additional anomalies. The electrical resistivity exhibits a clear kink at T_N and the Hall effect points to electron conduction in a good metal. For a summary of the magnetic parameters we refer to Tab. 5.1.

5.2.1 Zero-Field AC Susceptibility

Fig. 5.6(a) shows the temperature dependence of the real part of the ac susceptibility of $\mathrm{ErB_2}$ in zero magnetic field for the three crystallographic directions ⟨100⟩, ⟨210⟩,

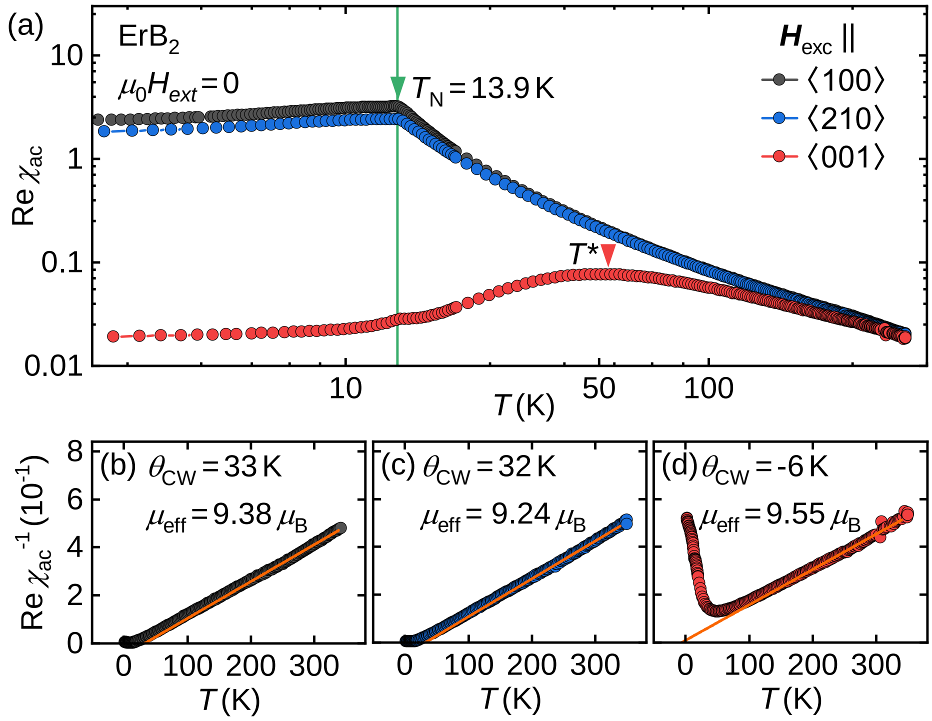

Figure 5.6: Real part of the ac susceptibility of single-crystal ErB$_2$ in zero magnetic field. (a) Double-logarithmic plot of the temperature dependence for excitation field along the three crystallographic directions ⟨100⟩, ⟨210⟩, and ⟨001⟩. (b) - (d) Inverse susceptibility and linear Curie-Weiss law fits for ⟨100⟩, ⟨210⟩, and ⟨001⟩. Anomalies are labelled and marked by coloured arrows.

and ⟨001⟩ on a double logarithmic scale.

For an excitation field along both ⟨100⟩ and ⟨210⟩, the ac susceptibility increases monotonically with decreasing temperature characteristic of a paramagnetic state. A distinct kink at the maximum, marked by the green arrow, indicates the transition to magnetic order at $T_N = 13.9$ K. Below the transition, the zero-field ac susceptibility remains at a comparatively high value decreasing only weakly with decreasing temperature.

For an ac excitation along ⟨001⟩, the ac susceptibility increases monotonically with decreasing temperature down to a broad maximum at $T^* \approx 50$ K, marked by the red arrow, followed by a decrease with decreasing temperature. A small cusp coincides with the transition temperature at $T_N = 13.9$ K. This cusp may be explained by a projection of the ac susceptibility along the easy plane due to a small misalignment of the sample. Compared to ⟨100⟩ and ⟨210⟩, the signal along ⟨001⟩ becomes distinctly smaller below approximately 100 K and is two orders of magnitude smaller in the limit of the lowest temperatures studied.

Based on these observations we conclude that the $\langle 100\rangle$ and $\langle 210\rangle$ directions are easy magnetic axis and hence the crystallographic basal plane of the hexagonal structure is an easy magnetic plane. In contrast, the $\langle 001\rangle$ direction is a hard magnetic axis. The broad maximum at T^* in the susceptibility for ac excitation along $\langle 001\rangle$ could characterize the onset of magnetic anisotropy well-above $T_\mathrm{N} = 13.9\,\mathrm{K}$. Similar maxima are observed in the magnetization and specific heat, as presented below.

Figs. 5.6(b) through (d) show the temperature dependence of the inverse ac susceptibility for an ac excitation along $\langle 100\rangle$, $\langle 210\rangle$, and $\langle 001\rangle$, respectively. Due to the additional contribution to the ac susceptibility at T^* along $\langle 001\rangle$, linear Curie-Weiss fits were applied in the range $200\,\mathrm{K} \leq T \leq 340\,\mathrm{K}$ well above T^*. These fits yield effective magnetic moments $\mu_{\mathrm{eff}\langle 100\rangle} = 9.38\,\mu_\mathrm{B}/\mathrm{f.u.}$, $\mu_{\mathrm{eff}\langle 210\rangle} = 9.24\,\mu_\mathrm{B}/\mathrm{f.u.}$, and $\mu_{\mathrm{eff}\langle 001\rangle} = 9.55\,\mu_\mathrm{B}/\mathrm{f.u.}$, as well as Weiss constants of $\Theta_{\mathrm{CW}\langle 100\rangle} = 33\,\mathrm{K}$, $\Theta_{\mathrm{CW}\langle 210\rangle} = 32\,\mathrm{K}$, and $\Theta_{\mathrm{CW}\langle 001\rangle} = -6\,\mathrm{K}$, as summarized in Tab. 5.1. The uncertainties of μ_eff and Θ_CW were estimated by varying the temperature range of the linear Curie-Weiss fits and comparing the results. However, the difference of approximately 30 K between Θ_CW for both in-plane directions and Θ_CW for the out-of-plane direction was found to be independent of the temperature range of the fit.

For all three directions, the value of the effective moment is close to the theoretical paramagnetic moment of Er^{3+}, $\mu_\mathrm{theo} = 9.58\mu_\mathrm{B}/\mathrm{Er}$ [133]. The Weiss constants for $\langle 100\rangle$ and $\langle 210\rangle$ have a positive sign, indicating ferromagnetic interactions, and are approximately double the transition temperature $T_\mathrm{N} = 13.9\,\mathrm{K}$. For $\langle 001\rangle$, the Weiss constant is approximately half the transition temperature and negative, characteristic of antiferromagnetic interactions.

Similar to other diborides [31], the hexagonal symmetry of the lattice raises the question whether geometric frustration plays a role [11]. This may be tested by means of the ratio $f = -\Theta_\mathrm{CW}/T_\mathrm{C}$, which is widely considered as a measure of the strength of geometric frustration. Values of f exceeding 10 imply a strong suppression of long-range order and strong geometric frustration. For the three directions we find $f_{\langle 100\rangle} = -2.37$, $f_{\langle 210\rangle} = -2.30$, and $f_{\langle 001\rangle} = 0.43$ implying that geometric frustration plays a minor role in this compound.

Table 5.1: Magnetic parameters of single-crystal ErB_2 inferred from the ac susceptibility and magnetization. $\mu_{2\,\mathrm{K},14\,\mathrm{T}}$ represents the value of the magnetization at 2 K in a field of 14 T. $f = -\Theta_\mathrm{CW}/T_\mathrm{C}$ is a measure for the strength of geometric frustration.

axis	μ_eff (μ_B/f.u.)	Θ_CW (K)	$\mu_{2\,\mathrm{K},14\,\mathrm{T}}$ (μ_B/f.u.)	$f = -\Theta_\mathrm{CW}/T_\mathrm{C}$
$\langle 100\rangle$	9.38 ± 0.3	33 ± 10	8.12	-2.37
$\langle 210\rangle$	9.24 ± 0.3	32 ± 10	-	-2.30
$\langle 001\rangle$	9.55 ± 0.3	-6 ± 10	9.13	0.43

5.2.2 Magnetization and AC Susceptibility in Finite Fields along ⟨100⟩

In the following, measurements of the magnetization and ac susceptibility as well as a magnetic phase diagram for magnetic fields along the easy axis ⟨100⟩ are presented.

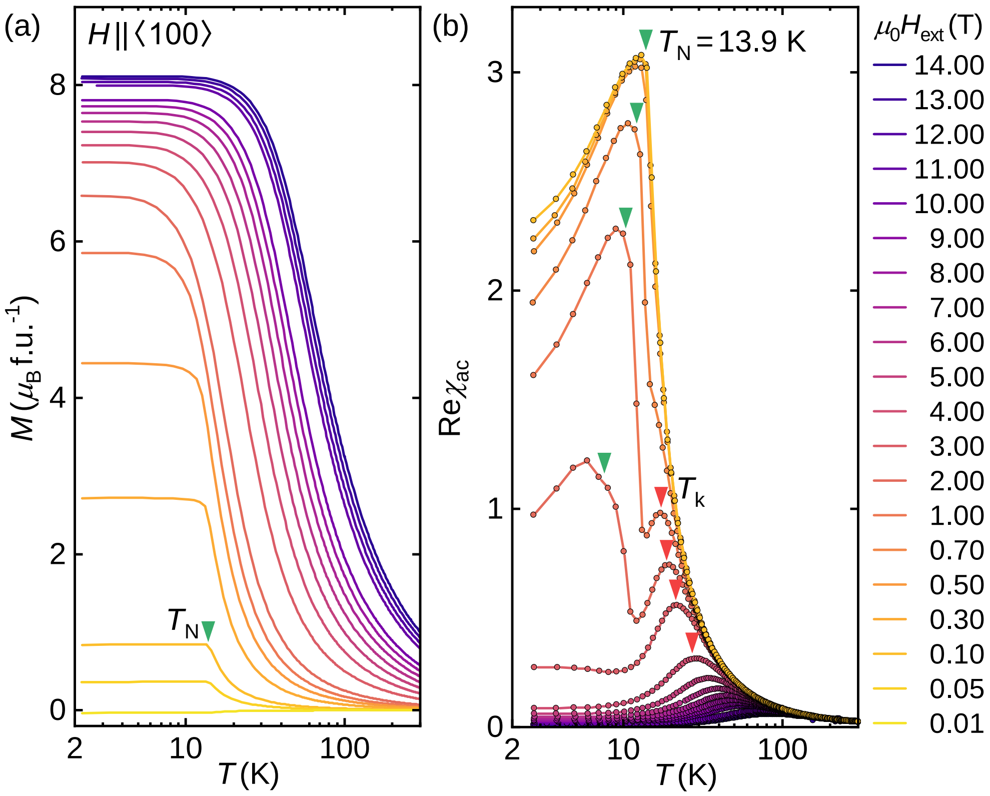

Figure 5.7: Temperature dependence of the magnetization and ac susceptibility of single-crystal ErB_2 for fields along the easy axis ⟨100⟩. (a) Magnetization and (b) real part of the ac susceptibility for selected magnetic fields. Features are labelled and marked with coloured arrows.

Figs. 5.7(a) and (b) show the temperature dependence of the magnetization and ac susceptibility of ErB_2 for selected magnetic fields up to 14 T along the easy axis ⟨100⟩.

For the small fields 0.01 T, 0.05 T and 0.10 T, the magnetization in Fig. 5.7(a) increases with decreasing temperature and a kink indicates the antiferromagnetic transition at $T_N = 13.9\,K$, marked by the green arrow. Below T_N, the magnetization remains constant. The same behaviour is observed for fields above 0.10 T, however, the magnetization increases and the kink at T_N smears out with increasing field until it may no longer be discerned for fields above 1 T. The magnetic moment reaches a value of approximately $8.12\,\mu_B$/f.u. at 14 T, which is below the Er^{3+} moment $9.0\,\mu_B$/f.u. [133].

The real part of the ac susceptibility, depicted in Fig. 5.7(b), increases up to a maximum at $T_{\mathrm{N}} = 13.9\,\mathrm{K}$ for small magnetic fields. Below T_{N}, the signal decreases. With increasing magnetic field, the ac susceptibility decreases, T_{N} shifts to lower temperatures, and a second maximum at T_{k} emerges, which is marked by the red arrow and first observed in a field of 0.7 T. T_{N} is no longer observable in fields above 1 T. With further increasing magnetic field, the overall signal decreases further and the ac susceptibility displays only a single maximum at T_{k}, which shifts to higher temperatures. T_{k} is ascribed to the crossover between the paramagnetic and the field-polarized state.

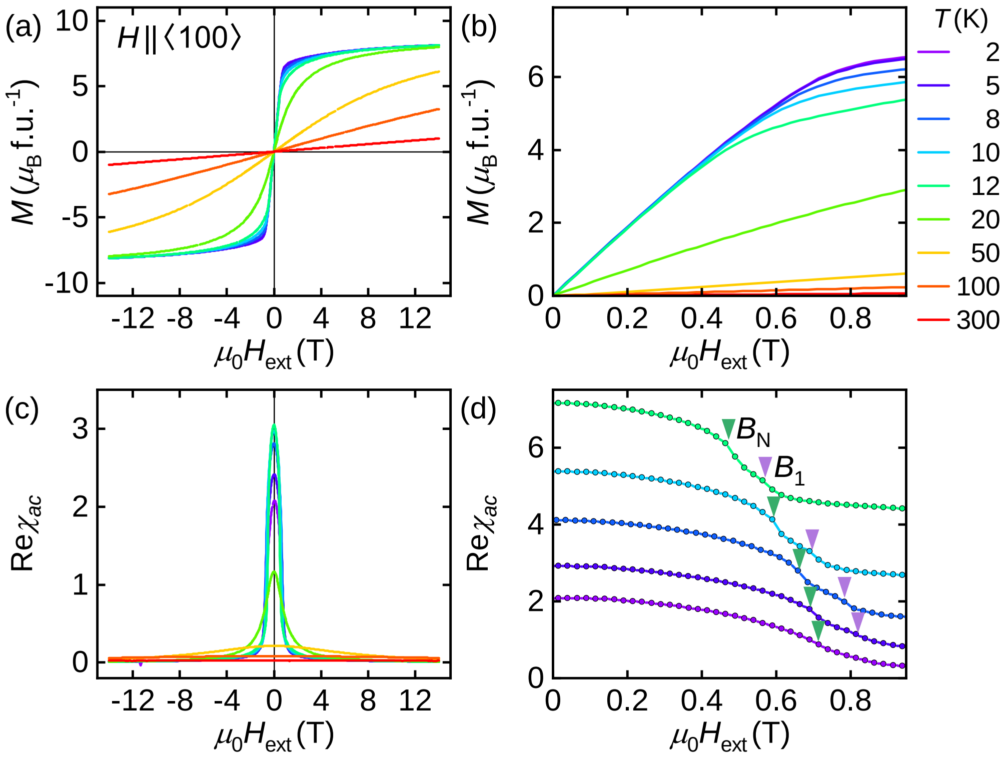

Figure 5.8: Magnetic field dependence of the magnetization and ac susceptibility of single-crystal $\mathrm{ErB_2}$ for fields along the easy axis $\langle 100 \rangle$. (a) Magnetization and (c) real part of the ac susceptibility over the entire field range, (b) magnetization and (d) real part of the ac susceptibility for positive fields below 1 T. For convenience, the ac susceptibility in (d) is shown with an offset between the curves. Features are labelled and marked with coloured arrows.

Next we present the magnetic field dependence of the magnetization and ac susceptibility for fields along the easy axis $\langle 100 \rangle$ in Fig. 5.8. The magnetization in Fig 5.8(a) is antisymmetric for all temperatures and decreases with increasing temperature. A close-up view for positive fields below 1 T is shown in Fig 5.8(b). In the following, we will only describe the behaviour for positive fields. At 2 K, starting at zero field, the magnetization displays a steep increase for increasing field below approximately 1 T. This is followed by a slow increase in the range from approximately 1 T to 14 T. The finite slope at 14 T may be due to crystal electric fields. A full 5-point loop recorded at 2 K showed no hysteresis, as presented above in Fig. 5.4 in Sec. 5.1. When increasing the temperature to 12 K, the s-shape of the curve remains and the signal tracks the 4 K curve for fields below approximately 0.5 T. Above approximately 0.5 T, the magnetization is smaller but approaches the 4 K curve with increasing field. At 20 K, the magnetization still displays an s-shape, although this temperature is above T_N. However, the slope at low fields is smaller and the magnetization remains well below the low-temperature value up to the highest field studied. At 50 K, signal and slope have decreased further and the magnetization still displays a small curvature. The evolution of decreasing signal and slope continues for 100 K and 300 K, but for those temperatures linear curves indicating paramagnetic behaviour are observed.

Fig 5.8(c) shows the field dependence of the real part of the ac susceptibility. At 2 K, a maximum is displayed at zero magnetic field. With increasing temperature, the height of this maximum increases and reaches a maximal value at 12 K. Further increasing the temperature, the maximum becomes broader and its height decreases until the ac susceptibility is essentially flat for temperatures above 100 K.

Fig 5.8(d) shows a close-up view of the field dependence of the ac susceptibility for fields below 1 T. For convenience, the curves are shown with an offset. At 2 K, with increasing field, a shoulder indicates a transition at B_N, marked by the green arrow. At 5 K, B_N is accompanied by a second shoulder observed at a higher field at B_1, marked by the purple arrow. With increasing temperature, both B_N and B_1 shift to lower magnetic fields. This double transition may be connected to the formation or transformation of magnetic domains but its precise nature and origin remains to be clarified.

Fig. 5.9 shows a magnetic phase diagram for fields along the easy axis $\langle 100 \rangle$, as inferred from the temperature and magnetic field dependence of the magnetization and ac susceptibility presented above. For the phase diagram data were corrected for demagnetization effects as discussed in Sec. 5.1. For high temperatures and magnetic fields, as shown in Fig. 5.9(a), a maximum in the ac susceptibility at T_K marks the crossover from a paramagnetic state (PM) in small magnetic fields to a field-polarized state (FP) in high magnetic fields. Fig. 5.9(b) depicts a close-up view for low temperatures and small magnetic fields. In zero magnetic field, ErB$_2$ exhibits a transition from a paramagnetic (PM, light grey shading) to an antiferromagnetic state (AFM, green shading) at $T_\mathrm{N} = 13.9\,\mathrm{K}$. For finite fields, the transition to the AFM is also observed at B_N. With increasing field, T_N and B_N shift to lower temperatures. Furthermore, an additional transition (X, light purple shading) is observed in the magnetic field dependence of the ac susceptibility at B_1, separating the AFM from the field polarized state (FP, light blue shading). Further investigations of this double-transition are in progress and beyond the scope of the work reported here.

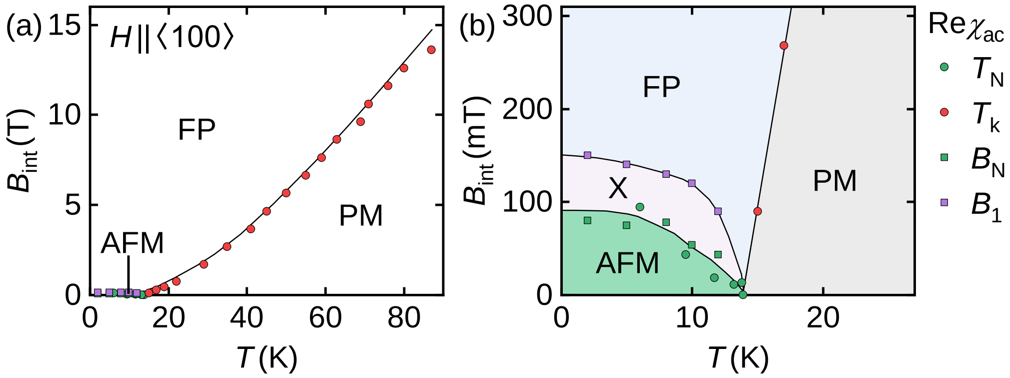

Figure 5.9: Magnetic phase diagram of single-crystal $\mathrm{ErB_2}$ for fields along the easy axis ⟨100⟩. The data are inferred from the real part of the ac susceptibility $\mathrm{Re}\chi_{\mathrm{ac}}$. The lines represent guides to the eye. Four regimes may be distinguished: The paramagnetic region (PM), the field-polarized region (FP), the antiferromagnet (AFM), and an unknown regime (X). (a) The crossover at T_{k} separates the paramagnetic (PM) from the field-polarized (FP) region. (b) Close-up view for low temperatures and small magnetic fields. The antiferromagnetic phase (AFM) and an additional unknown regime (X) are indicated by a double transition in the ac susceptibility.

5.2.3 Magnetization and AC Susceptibility in Finite Fields along ⟨001⟩

In the following, measurements of the magnetization and ac susceptibility as well as a magnetic phase diagram for magnetic fields along the hard axis ⟨001⟩ are presented.

The temperature dependence of the magnetization and ac susceptibility for selected magnetic fields up to 14 T along the hard axis ⟨001⟩ is depicted in Fig. 5.10(a) and (b), respectively. At 0.10 T, with decreasing temperature, the magnetization in Fig. 5.10(a) increases and exhibits a broad maximum at $T^* \approx 50\,\mathrm{K}$, marked by the red arrow, followed by a decrease below T^*. This behaviour is observed similarly for magnetic fields up to 11 T, but the magnetization increases and T^* shifts to lower temperatures with increasing magnetic field. At 11 T, a second anomaly is inferred from a kink at T_{s}, marked by the blue arrow. Since the magnetization represents the combination of both anomalies, T^* is now inferred from a shoulder instead of the maximum. At 12 T, the shoulder indicating T^* has shifted back to a higher temperature. The second anomaly T_{s} is now indicated by a maximum and has shifted to a lower temperature. For fields above 12 T, the magnetization increases monotonically with decreasing temperature. The shoulder indicating T^* shifts to higher temperatures with increasing field and T_{s} is no longer observable. Intriguingly, the maximum magnetization of $9.13\,\mu_{\mathrm{B}}/\mathrm{f.u.}$ at 14 T is larger than the observed value of $8.12\,\mu_{\mathrm{B}}/\mathrm{f.u.}$ for field along ⟨100⟩ and larger than the theoretical saturation moment of $9.0\,\mu_{\mathrm{B}}/\mathrm{f.u.}$ of Er^{3+}. This may be due to crystal field effects and requires further studies beyond the work reported here. T^* is ascribed to anisotropic magnetic

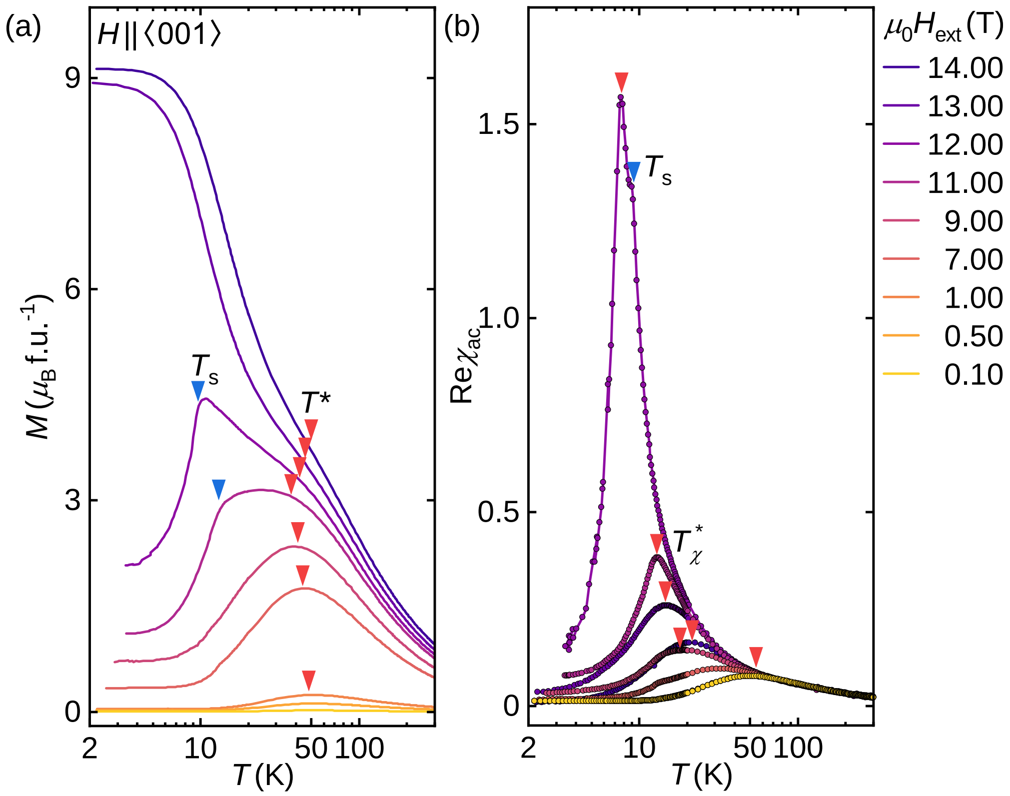

Figure 5.10: Temperature dependence of the magnetization and ac susceptibility of single-crystal ErB$_2$ for fields along the hard axis ⟨001⟩. (a) Magnetization and (b) real part of the ac susceptibility for selected magnetic fields. Features are labelled and marked with coloured arrows.

fluctuations that emerge with decreasing temperature. As presented above, a similar maximum at approximately 50 K was observed in the zero-field ac susceptibility for excitation field along ⟨001⟩. T_s agrees with a spin-flip transition observed in the field dependence of the magnetization and ac susceptibility as shown below.

Similar to the magnetization, the real part of the ac susceptibility, depicted in Fig. 5.10(b) increases and exhibits a broad maximum at $T^*_\chi \approx 50$ K, marked by the red arrow, followed by a decrease below T^*_χ for small magnetic fields. With increasing field, the ac susceptibility increases and the maximum at T^*_χ becomes sharper and shifts to lower temperatures. At 12 T a shoulder at T_s, marked by the blue arrow, emerges in addition to T^*_χ. For fields above 12 T, the ac susceptibility decreases and T^*_χ is inferred from a single maximum that shifts back to higher temperatures with increasing field. Interestingly T^*_χ as inferred from the ac susceptibility and T^* as inferred from the magnetization are observed at different temperatures. In contrast, T_s is observed at the same temperature in both the ac susceptibility and the magnetization in agreement with a spin-flip transition reported below.

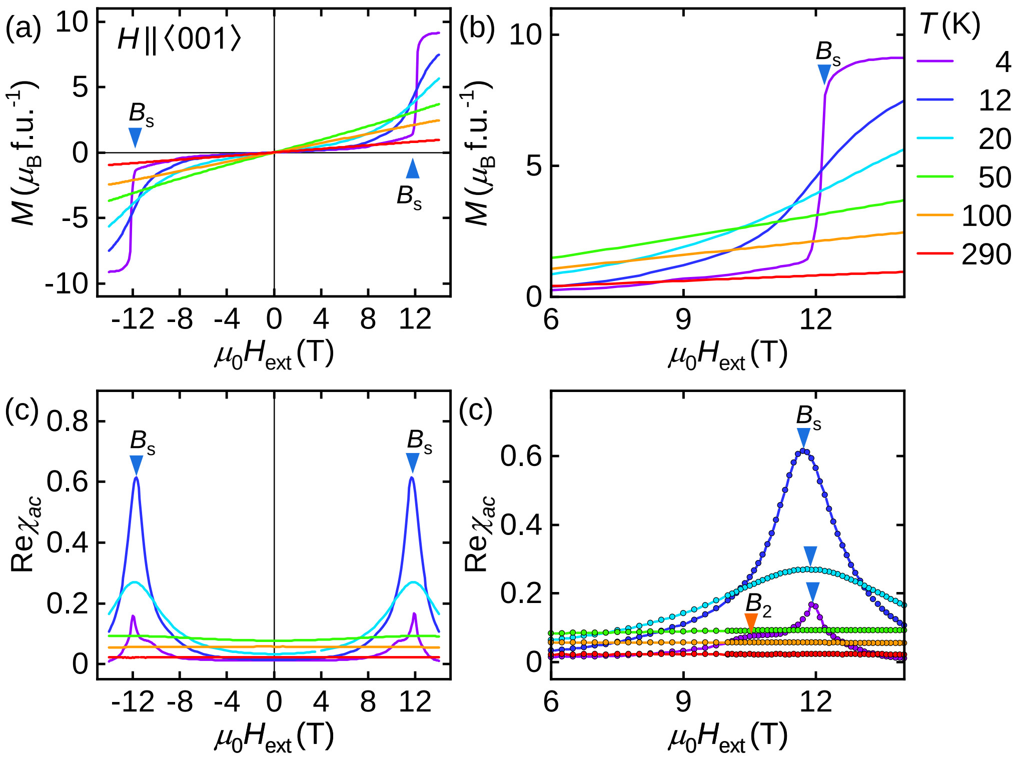

Figure 5.11: Magnetic field dependence of the magnetization and ac susceptibility of single-crystal $\mathrm{ErB_2}$ for fields along the hard axis $\langle 001 \rangle$. (a) Magnetization and (c) real part of the ac susceptibility over the entire field range, (b) magnetization and (d) real part of the ac susceptibility for positive fields in the range 6 T to 14 T. Features are labelled and marked with coloured arrows.

The field dependence of the magnetization for field along the hard axis $\langle 001 \rangle$ is shown in Fig. 5.11(a). In the following, we will discuss only positive fields as shown in Fig. 5.11(b). In contrast to field along the easy $\langle 100 \rangle$ direction, the curves for different temperatures cross each other with increasing fields. We start at 4 K in zero field, where the magnetization increases weakly with increasing field. At $B_\mathrm{s} = 11.8\,\mathrm{T}$, marked by the blue arrow, the curve displays a steep increase followed by a flattening at highest fields. The steep increase at $B_s = 11.8\,\mathrm{T}$ and the size of the change of the magnetization are characteristic of a spin-flip transition, rather than spin-flop, in agreement with the strong anisotropy in this compound. A hysteresis of the size of about 40 mT is observed in the 5-point field scan of the spin-flip transition at 4 K, as depicted in Fig. 5.12. At 12 K, 20 K, 50 K, 100 K, and 300 K, the steep increase that was observed at 4 K at $B_\mathrm{s} = 11.8\,\mathrm{T}$ smears out and the magnetization at 14 T

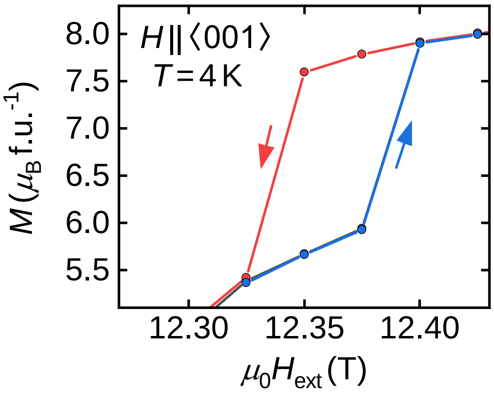

Figure 5.12: Magnetic field dependence of the magnetization of single-crystal ErB$_2$ for fields along the hard axis $\langle 001 \rangle$ at a temperature of 4 K. A hysteresis of about 40 mT is observed between scans for increasing (blue) and decreasing (red) magnetic field.

decreases with increasing temperature. The curves for 12 K and 20 K display a weak finite curvature, whereas the magnetization for 50 K, 100 K, and 300 K shows linear behaviour in agreement with the paramagnetic state.

The field dependence of the real part of the ac susceptibility is shown in Fig. 5.11(a) over the entire field range. Fig. 5.11(b) displays positive fields between 6 T and 14 T. At 4 K, with increasing field, an anomaly is observed at B_2, marked by the orange arrow, where the ac susceptibility exhibits an additional shoulder. The spin-flip transition at B_s, marked by the blue arrow, is inferred from a maximum at 11.8 T. At 12 K and 20 K, B_2 is not observable and the maximum at B_s displays a weak shift to lower temperatures and becomes broader in agreement with the smearing out of the magnetization as discussed above. At 50 K, 100 K, and 300 K, the ac susceptibility is essentially flat and exhibits no anomalies. Clarifying the origin of B_2 requires further investigation beyond the scope of the work reported here.

Fig. 5.13 shows a magnetic phase diagram for fields along the hard axis $\langle 001 \rangle$, as inferred from the temperature and magnetic field dependence of the magnetization and ac susceptibility presented above. Data in the phase diagram have been corrected for demagnetization effects as discussed in Sec. 5.1. For high temperatures and small magnetic fields, a signature in the magnetization at T^* marks the crossover from a paramagnetic state (PM, light grey shading) to an anisotropy-dominated region (AD, light red shading). With decreasing temperature, thermal fluctuations become weaker and the magnetic anisotropy emerges at approximately 50 K, well-above T_N. For high temperatures and large magnetic fields, T^* marks the crossover from the PM into the field-polarized (FP, light blue shading) region. The antiferromagnetic phase (AFM, green shading) is located at temperatures below $T_N = 13.9$ K and magnetic fields smaller than approximately 12 T. With increasing field a spin-flip transition occurs at $B_s = 11.8$ T marking the transition from the AFM to the FP. An additional

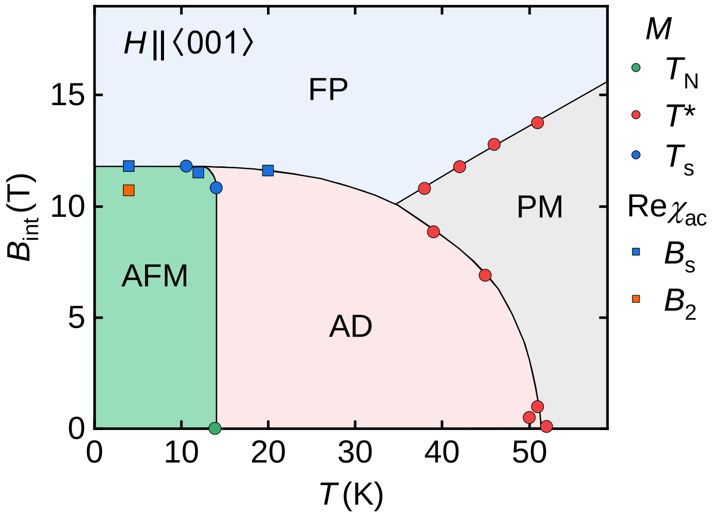

Figure 5.13: Magnetic phase diagram of single-crystal ErB_2 for fields along the hard axis ⟨001⟩. Points inferred from the magnetization M and the real part of the ac susceptibility $\mathrm{Re}\chi_{\mathrm{ac}}$. The lines represent guides to the eye. Four regimes may be distinguished: The paramagnetic region (PM), the field-polarized region (FP), the anisotropy-dominated region (AD) and the antiferromagnetic state (AFM). A crossover at T^* separates the PM from the AD or FP, depending on the applied magnetic field. A spin-flip transition at 4 K in a field of 11.8 T corroborates the strong magnetic anisotropy in ErB_2.

transition is observed in the magnetic field dependence of the ac susceptibility at B_1. Further investigations are in progress and beyond the work reported here.

5.2.4 Specific Heat

Fig. 5.14(a) shows the temperature dependence of the specific heat of ErB_2 in zero magnetic field. At high temperatures, $C(T)$ approaches the limit of Dulong-Petit at $74.83\,\mathrm{J\,mol^{-1}\,K^{-1}}$. The red line corresponds to a numerical evaluation of the Debye model with $\Theta_{\mathrm{Debye}} = 710\,\mathrm{K}$, displaying a large deviation at low temperatures and approaching the measured curve with increasing temperature. Similar to other transition-metal and rare-earth diborides [31, 35, 37], a simple Debye model is not sufficient to describe the lattice dynamics in ErB_2. Marked by the green arrow is the lambda anomaly at $T_{\mathrm{N}} = 13.9\,\mathrm{K}$ at the onset of long-range magnetic order in agreement with the ac susceptibility and magnetization. In addition, the specific heat curve displays an additional shoulder at $T_{\mathrm{h1}} \approx 50\,\mathrm{K}$ as marked by the red arrow. Similar to the broad maximum at T^* observed in the magnetization and ac susceptibility for field along the hard axis ⟨001⟩, this feature is empirically consistent with the emergence of anisotropic magnetic fluctuations well-above T_{N}.

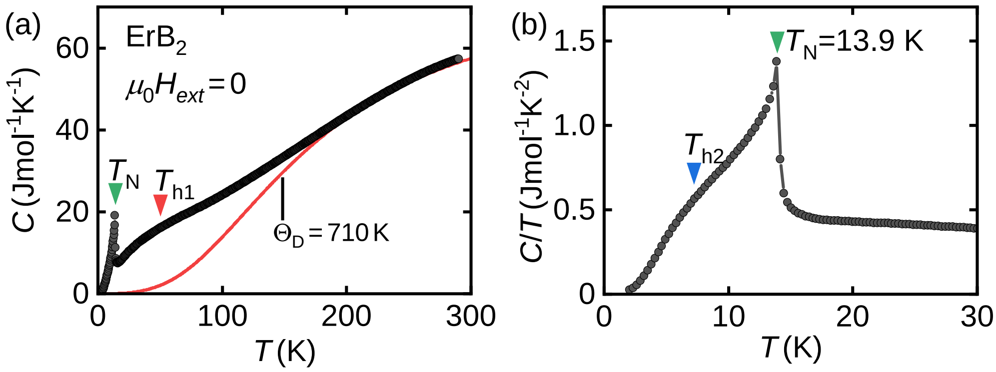

Figure 5.14: Specific heat of single-crystal ErB$_2$. (a) Temperature dependence of the specific heat with Debye model. (b) Low-temperature part of the specific heat divided by temperature. Anomalies are labelled and marked by coloured arrows.

The low-temperature part of the specific heat divided by the temperature is depicted in Fig. 5.14(b). The contribution linear in temperature approaches $C/T \rightarrow 24\,\mathrm{mJ\,mol^{-1}\,K^{-2}}$ at the lowest temperature, representing an upper limit of the Sommerfeld coefficient γ. In fact, the actual value of γ is likely to be lower since the specific heat divided by temperature still displays a pronounced slope at the lowest temperature measured. Moreover, the curve displays a shoulder around 8 K as marked by the blue arrow in Fig. 5.14(b). Similar behaviour of the specific heat below the magnetic transition has also been reported in antiferromagnetic CrB$_2$ [31], but the origin behind these observations in ErB$_2$ and CrB$_2$ remains to be clarified.

5.2.5 Electrical Resistivity and Hall Effect

The zero-field temperature dependence of the electrical resistivity $\rho_{xx}(T)$ of ErB$_2$ is shown in Fig. 5.15(a) for current along $\langle 100\rangle$ and $\langle 001\rangle$. The resistivity for current along the easy axis $\langle 100\rangle$ is smaller than for the hard axis, $\langle 001\rangle$. In contrast to the ac susceptibility and the magnetization, there is no qualitative difference between the two configurations. For both directions, the resistivity shows metallic behaviour, decreasing monotonically with decreasing temperature. Denoted by a green arrow is the magnetic transition where $\rho_{xx}(T)$ drops abruptly at $T_{\mathrm{N}} = 13.9\,\mathrm{K}$ in agreement with the ac susceptibility, magnetization, and specific heat.

The low-temperature resistivity is shown in Fig. 5.15(b). Below the transition, the resistivity may be fitted with a power law $\rho_{xx}(T) = \rho_0 + \mathrm{A} \cdot T^{\mathrm{c}}$ in good agreement with both crystallographic directions. As typical for metallic systems and in particular diborides [31, 69], we find residual resistivities ρ_0 of $3.62\,\mu\Omega\,\mathrm{cm}$ and $4.37\,\mu\Omega\,\mathrm{cm}$ for $\langle 100\rangle$ and $\langle 001\rangle$, respectively. The associated residual resistivity ratios are $\mathrm{RRR}_{\langle 100\rangle} = 6$ and $\mathrm{RRR}_{\langle 001\rangle} = 5.5$ for the $\langle 100\rangle$ and $\langle 001\rangle$ direction. The key parameters of the power law are $A_{\langle 100\rangle} = 45.8\,\mathrm{n\Omega cmK^{-c}}$ and $A_{\langle 001\rangle} = 41.9\,\mathrm{n\Omega cmK^{-c}}$

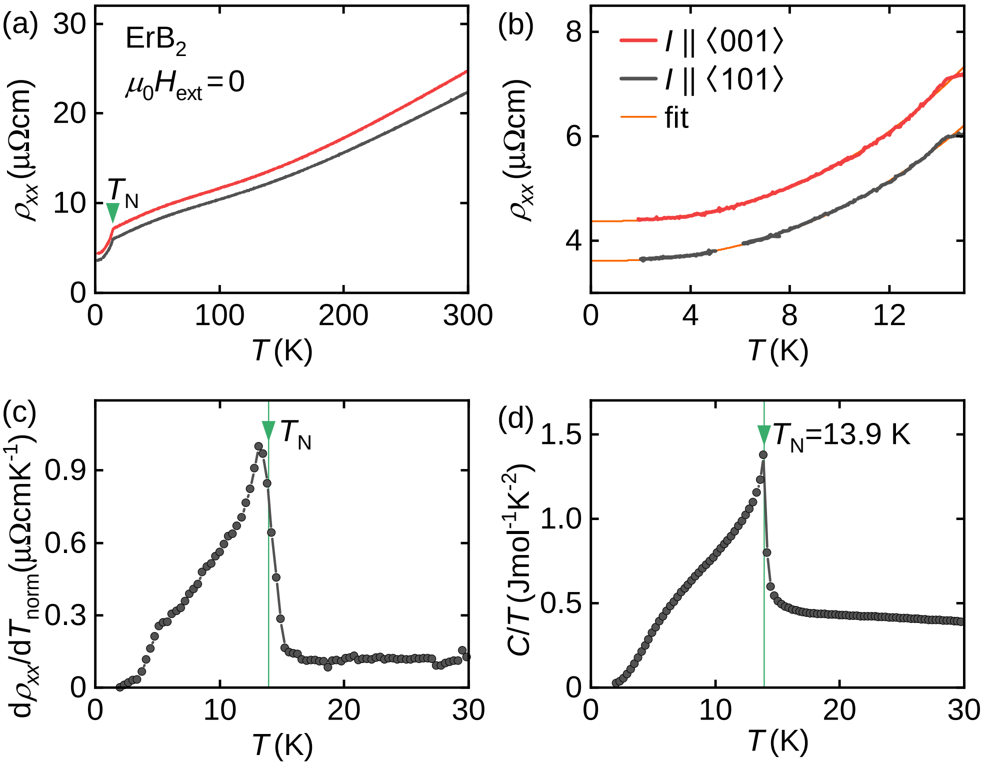

Figure 5.15: Temperature dependence of the zero-field resistivity and the specific heat divided by the temperature in single-crystal ErB$_2$. (a) Longitudinal electrical resistivity for current along $\langle 100\rangle$ and $\langle 001\rangle$ over the temperature range 2 K to 300 K. The green arrow marks the magnetic transition. (b) Close-up view of the low-temperature resistivity with power-law fits below the transition. (c) Normalized derivative of the resistivity by the temperature, and for comparison (d) low-temperature part of the specific heat divided by the temperature as presented above.

with exponents $c_{\langle 100\rangle} = 2.34$ and $c_{\langle 001\rangle} = 2.42$. The data is in good agreement with the results on polycrystalline ErB$_2$ in Ref. [69].

Fig. 5.15(c) shows the normalized derivative of the resistivity with respect to the temperature $\mathrm{d}\rho_{xx}/\mathrm{d}T$ for current along $\langle 100\rangle$ at low temperatures. A comparison between the specific heat divided by the temperature $C(T)/T$, shown in Fig. 5.15(d), with $\mathrm{d}\rho_{xx}/\mathrm{d}T$ in Fig. 5.15(c) shows that the temperature dependence of the specific heat follows qualitatively the derivative of the resistivity. This may be expected theoretically when the scattering observed in the resistivity follows Fermi's golden rule, where the density of states dominates the specific heat. Such a similarity between $C(T)/T$ and $\mathrm{d}\rho_{xx}/\mathrm{d}T$ was also observed in single-crystal CrB$_2$ [31].

Fig. 5.16(a) shows the relative transverse magnetoresistance $\rho_{xx}(T,B)/\rho_{xx}(T,0)$

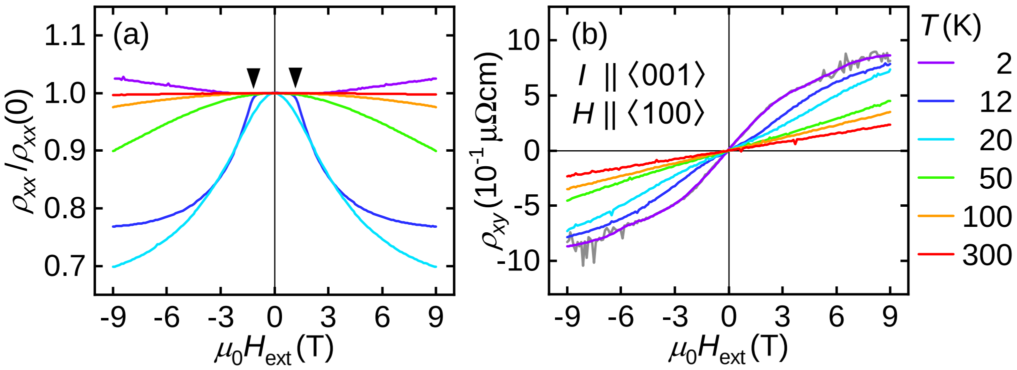

Figure 5.16: Field dependence of the electrical resistivity for current along the hard axis ⟨001⟩ and field along the easy axis ⟨100⟩ for selected temperatures in single-crystal ErB$_2$. (a) Transverse magnetoresistance. (b) Hall resistivity.

for current along the hard axis ⟨001⟩ and field along the easy axis ⟨100⟩ for selected temperatures. The signal displays symmetric behaviour under magnetic fields and the absolute values increase with temperature. At 2 K, the minimum of the resistivity is located at zero field and the curve shows a small monotonic increase in finite fields, i.e., positive magnetoresistance. At 12 K, the resistivity features a plateau in the range from approximately -1 T to 1 T, as marked by the black arrows in Fig. 5.16(a). For larger fields, the curve decreases monotonically, i.e. it exhibits a negative magnetoresistance. Above the magnetic transition, at 20 K, the signal shows a maximum in zero-field and a monotonic decrease under field. This behaviour is similar at 50 K and 100 K, but the decrease becomes weaker with increasing temperature. At 300 K, the resistivity is essentially constant.

Fig. 5.16(b) shows the field dependence of the Hall resistivity ρ_{xy} for current along the hard axis ⟨001⟩ and field along the easy axis ⟨100⟩ at selected temperatures. The signal is one order of magnitude smaller than the longitudinal resistivity. At 2 K, the curve shows an s-shape reminiscent of the anomalous Hall signal observed in ferromagnetic materials [134]. For fields larger than approximately 6 T, the signal is rather noisy but the general trend is still clearly visible. At 12 K and 20 K, the transverse resistivity is qualitatively similar to the 2 K curve, but curvature and signal size are decreasing with increasing temperature. At 50 K, 100 K, and 300 K, the Hall resistivity shows linear behaviour with a decreasing slope for increasing temperature.

Describing the Hall effect by

$$\rho_{\mathrm{Hall}} = \mathrm{R}_0 B \tag{5.1}$$

with the normal Hall constant $\mathrm{R}_0 = -1/ne$, and the elemental charge e, the charge carrier density n at 300 K is given by $n = 2.41 \times 10^{32}\,\mathrm{m}^{-3}$. This value is typical for electron conduction in a good metal, substantiating the metallic character of ErB$_2$.

5.3 Conclusions

A ^{11}B-enriched single crystal of $\mathrm{ErB_2}$ was prepared from stoichiometric polycrystalline starting material by self-adjusted flux travelling solvent optical floating zone under a dynamic high-purity argon atmosphere of 18 bar. The float-zoned ingot was analysed by x-ray Laue diffraction, confirming the presence of a single crystal with a length and diameter of approximately 5 mm and 6 mm, respectively. Using x-ray powder diffraction in combination with a Rietveld refinement, the expected hexagonal space group $P6/mmm$ was confirmed and lattice constants in good agreement with the literature were extracted.

Measurements of the magnetization and ac susceptibility indicate easy-plane antiferromagnetic order below a temperature of $T_{\mathrm{N}} = 13.9\,\mathrm{K}$, in agreement with the specific heat, resistivity and Hall effect. The susceptibility reveals a strong anisotropy between the easy in-plane directions $\langle 100\rangle$ and $\langle 210\rangle$ and the hard out-of plane direction $\langle 001\rangle$. Curie-Weiss fits of the zero field ac susceptibility yield large effective magnetic moments in all three directions and the Weiss constants indicate ferromagnetic and antiferromagnetic interactions in the easy plane and along the hard axis, respectively. Small ratios between the Weiss constants and the transition temperature point to a minor influence of geometric frustration.

Magnetic phase diagrams for field along $\langle 100\rangle$ and $\langle 001\rangle$ are inferred from the magnetization and ac susceptibility. For field along $\langle 100\rangle$, at high temperatures, a crossover between the paramagnetic state and the field-polarized region is observed at T_{k}. At low temperatures, antiferromagnetic order is observed below $T_{\mathrm{N}} = 13.9\,\mathrm{K}$ in zero field. In finite fields, B_{N} is observed in agreement with T_{N}. With increasing field, T_{N} and B_{N} shift to lower temperatures. The ac susceptibility displays a second transition at B_1 in higher fields which remains subject to further investigation. For fields along $\langle 001\rangle$, with decreasing temperature, anisotropic magnetic fluctuations emerge below $T^* \approx 50\,\mathrm{K}$, marking the crossover between the paramagnetic state and an anisotropy-dominated region. In large magnetic fields, T^* tracks the crossover between the paramagnetic and the field-polarized region. At low temperatures, antiferromagnetic order is observed below 13.9 K and approximately 11.8 T. With increasing field, a spin-flip transition is observed in a field of $B_s = 11.8\,\mathrm{T}$ which marks the transition from the antiferromagnet to the field-polarized region. At at 4 K, a shoulder at B_2 is observed in the ac susceptibility in higher fields which remains subject to further investigation.

The temperature dependence of the specific heat exhibits a distinct lambda anomaly at $T_{\mathrm{N}} = 13.9\,\mathrm{K}$ clearly marking the transition to long-range magnetic order. Furthermore, we observe two additional anomalies in the specific heat at approximately 8 K and 50 K, the latter in agreement with T^* observed in the magnetization and ac susceptibility. An upper limit for the Sommerfeld coefficient of $\gamma = 24\,\mathrm{mJ\,mol^{-1}\,K^{-2}}$ was established.

Measurements of the zero-field temperature dependence of the longitudinal electrical resistivity show a distinct drop below a temperature of 13.9 K indicating T_{N} in agreement with the bulk data. We find similar residual resistivity ratios $\mathrm{RRR}_{\langle 100\rangle} = 6$

and $\mathrm{RRR}_{\langle 001\rangle} = 5.5$ for the $\langle 100\rangle$ and $\langle 001\rangle$ direction. For field along the easy axis $\langle 100\rangle$, the Hall resistivity displays a characteristic shape reminiscent of the anomalous Hall effect. We extracted a charge carrier density of $n = 2.41 \times 10^{32}\,\mathrm{m}^{-3}$ from the normal Hall effect at room temperature pointing to electron conduction and a metallic state.

Our observations suggest that ErB_2 is an easy-plane antiferromagnet with a ferromagnetic alignment of magnetic moments along the in-plane directions and an antiferromagnetic alignment between alternating $\langle 100\rangle \times \langle 210\rangle$ planes along the $\langle 001\rangle$ direction. Future work concerns detailed measurements of the bulk properties for magnetic field along the hard axis $\langle 001\rangle$. Ultimately, neutron experiments could verify the easy-plane antiferromagnetism in ErB_2. The preparation and characterization of single crystals of the sibling rare-earth diborides DyB_2 and HoB_2 will follow in the near future.

CHAPTER 6

Itinerant Magnetism and Reentrant Spin-Glass Behavior in Fe$_x$Cr$_{1-x}$

This chapter reports the investigation of polycrystalline Fe$_x$Cr$_{1-x}$ alloys in the range $0 \leq x \leq 0.30$, representing the isostructural substitution between two archetypical forms of ferro- and antiferromagnetism accompanied by reentrant spin glass behaviour for intermediate concentrations. Comprehensive studies are presented that establish a rich phase diagram indicating a precursor regime between spin glass and the magnetic regions and report the concentration dependence of the spin glass state in this model system for statistical disorder.

This chapter is organized as follows. In Sec. 6.1 the binary phase diagram of the Fe-Cr-system is introduced and the preparation of the samples and their metallurgical characterization by means of x-ray powder diffraction is described. This is followed by a short overview about the measured samples and parameters of the bulk property and neutron depolarization measurements. Next, Sec. 6.2 reports the data and results. First, the compositional phase diagram is presented and magnetometry as well as neutron depolarization measurements are discussed. In particular it is demonstrated that the transition temperatures of the four different regimes, notably antiferromagnetism, ferromagnetism, spin glass, and a novel precursor regime, are most conveniently identified in the imaginary part of the ac susceptibility. A distinction between the four regimes is made by the characteristic behaviour of the bulk properties in finite magnetic fields. Neutron depolarization measurements corroborate these findings and help to establish the phase diagram. Lastly exemplaric measurements of the specific heat, the electrical resistivity, and the magnetization on $x = 0.15$ in high fields are presented. Subsequently, Sec. 6.3 comprises the evaluation of the spin glass type based on the Mydosh parameter, a Vogel–Fulcher analysis, and power law fits. It is shown that the nature of the spin glass state changes from a cluster-glass to a superparamagnet with increasing concentration x, accompanied by a decrease in characteristic times and a strong intercluster correlation. To conclude, Sec. 6.4 summarizes the central findings of this study and provides an outlook on open questions in $\mathrm{Fe}_x\mathrm{Cr}_{1-x}$.

The content of this chapter is complemented by the Ph.D. theses of Philip Schmakat [77], who measured the neutron depolarization data presented below and Steffen Säubert [90], who investigated the relaxation processes in $\mathrm{Fe}_x\mathrm{Cr}_{1-x}$ by neutron spin-echo techniques.

6.1 Experimental Methods

The following section reports the sample preparation followed by the characterization and an overview on the measurements. We refer to Chap. 3 for details on the techniques and apparatus.

6.1.1 Preparation of $\mathrm{Fe}_x\mathrm{Cr}_{1-x}$

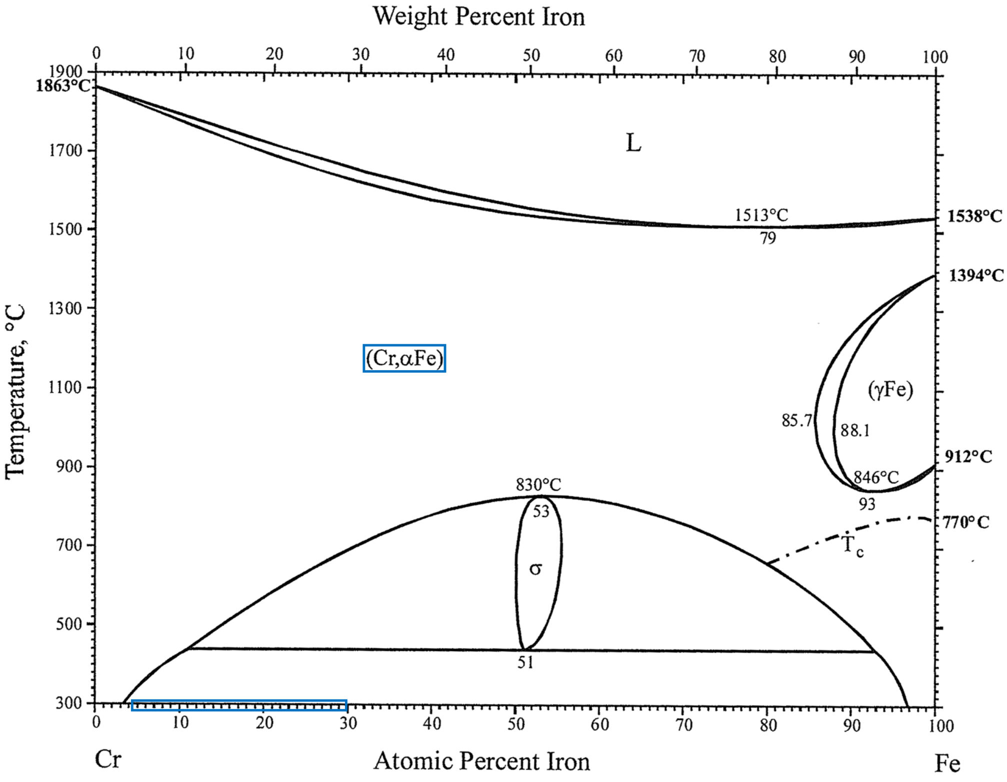

Figure 6.1: Binary phase diagram of the Cr-Fe-system. A solid solution with α-Fe structure is formed over almost the entire concentration range. At lower temperatures, exsolution into two α-Fe phases with different concentrations or α-Fe and σ-Fe occurs, depending on the temperature and concentration. Figure adapted from Ref. [42].

The binary phase diagram of the Fe-Cr-system is depicted in Fig. 6.1, where the region of composition of investigated alloys is marked by the blue box on the x-axis. Apart from the pocket with the γ-Fe phase for high Fe concentrations, Cr and Fe form a solid solution with α-Fe structure below the liquidus for all concentrations. However, at temperatures below 830 °C, the exsolution phenomenon occurs for concentrations between approximately 4 % to 97 % Fe. Here, the solid solution is no longer stable and begins to exsolve into two phases with α-Fe and σ-Fe structure. When further lowering the temperature, σ-Fe becomes unstable and the system forms two α-Fe phases with different concentrations. Nevertheless it is possible to conserve a single α-Fe phase by rapidly quenching, i.e. cooling the melt to room temperature. With this procedure, the system cannot reach the equilibrium in the short time of cooling down and hence the exsolution is prevented.

Polycrystalline samples of $\mathrm{Fe}_x\mathrm{Cr}_{1-x}$ for $0.05 \leq x \leq 0.30$ ($x = 0.05$, 0.10, 0.15, 0.16, 0.17, 0.18, 0.18, 0.19, 0.20, 0.21, 0.22, 0.25, 0.30) were prepared from 4N Fe (MaTecK GmbH) and 5N Cr (Alfa Aesar, Thermo Fisher Scientific Inc.) by radio-frequency induction melting in the rod casting furnace (see Chap. 3). Before the synthesis, the recipient was pumped down to ultra-high vacuum pressure and subsequently flooded to 1.4 bar with 6N argon via a point-of-use gas purifier to enhance the purity to nominally 9N. The starting elements were alloyed in a water-cooled Hukin crucible and after homogenization in the melt for approximately 10 min, the samples were quenched to room temperature. With this approach, the imminent exsolution of the compound into two phases upon cooling could be prevented. No losses in weight or signatures of evaporation were observed. In turn, the composition is denoted in terms of the weighed-in amounts of starting material. From the resulting ingots, smaller samples were cut with a diamond wire saw.

6.1.2 X-Ray Powder Diffraction

From a small piece of each ingot, powder was prepared using an agate mortar and x-ray powder diffraction at room temperature was carried out on a Huber G670 in Guinier geometry. Fig. 6.2(a) shows the diffraction pattern for $x = 0.15$ as a typical example. A Rietveld refinement based on the $Im\overline{3}m$ structure yields a lattice constant of $a = 2.883$ Å. Refinement and experimental data are in excellent agreement, indicating a high structural quality and homogeneity of the polycrystalline samples. With increasing x the diffraction peaks shift to larger angles, as shown for the (011) peak in Fig. 6.2(b), reflecting an essential linear decrease of the lattice constant, in accordance with Vegard's law.

6.1.3 Measurements

Bulk property and neutron depolarization measurements were carried out on thin slices with a thickness of ≈ 0.5 mm and a diameter of ≈ 10 mm. Specific heat and electrical transport measurements were conducted on a small cube with $2 \times 2 \times 2$ mm^3 and a platelet with $5 \times 2 \times 0.5$ mm^3, respectively, cut from the $x = 0.15$ ingot.

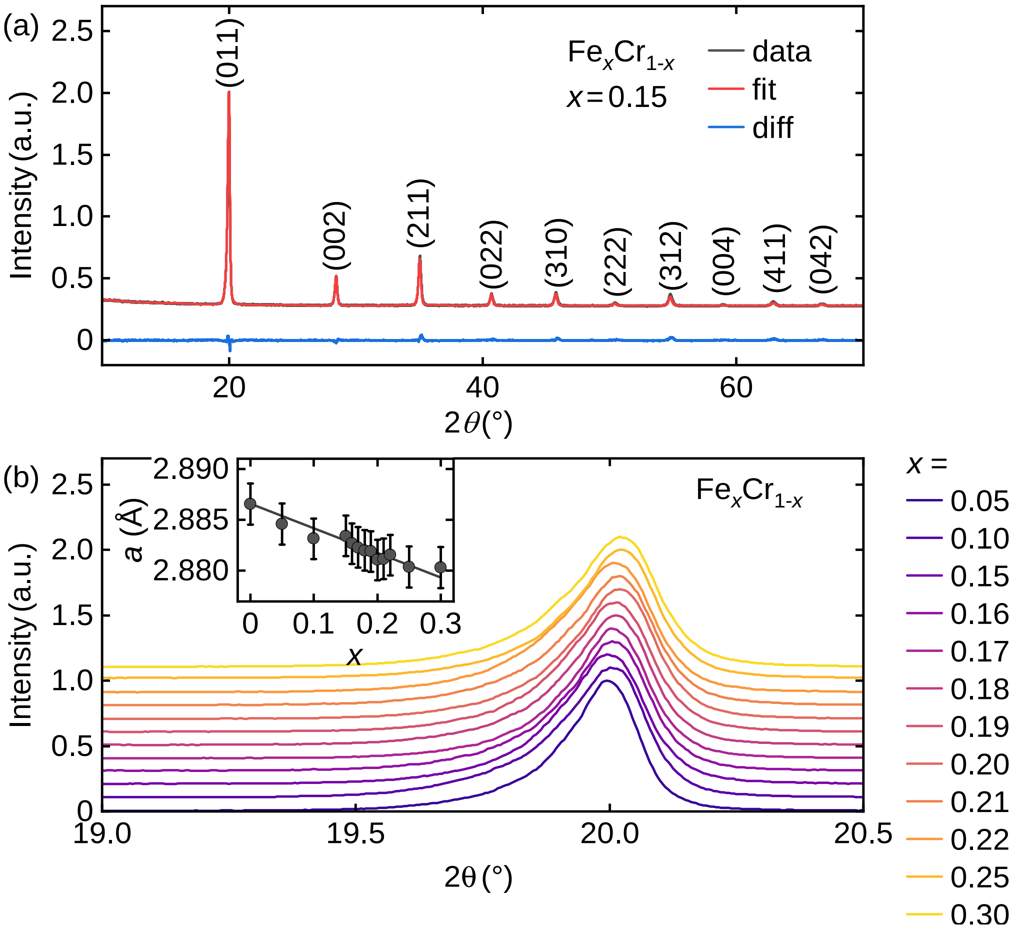

Figure 6.2: X-ray powder diffraction on Fe_xCr_{1-x}. (a) Diffraction pattern for $x = 0.15$. The Rietveld refinement (red curve) is in excellent agreement with the experimental data and confirms the $Im\bar{3}m$ structure. (b) Close-up view of the diffraction pattern around the (011) peak for all concentrations studied. For clarity, the intensities are normalized and the curves are offset by 0.1. Inset: Essential linear decrease of the lattice constant a with increasing x, the solid grey line represents a guide to the eye.

All bulk properties were measured in a Quantum Design PPMS. In general, magnetization and ac susceptibility with an excitation of $\mu_0 H_{ac} = 1\,mT$ and a frequency of $f = 1000\,Hz$ were recorded for temperatures from 2 K to 350 K in fields up to 250 mT. The zero field ac susceptibility was additionally measured at frequencies ranging from 10 Hz to 10 000 Hz. The high-field dependence of the magnetization and the ac susceptibility was measured exemplarily on $x = 0.15$ in fields up to 9 T for temperatures of 2 K, 10 K and 50 K. The temperature dependence of the specific heat in zero field and the electrical resistivity in fields up to 1 T were also studied exemplarily on $x = 0.15$.

Neutron depolarization was measured by Philipp Schmakat [77] at the instrument ANTARES [135] at the Heinz Maier-Leibniz Zentrum (MLZ). The incoming neutron beam had a wavelength $\lambda = 4.13$ Å and a wavelength spread $\Delta\lambda/\lambda = 10\%$. It was polarized using V-cavity supermirrors. The beam was transmitted through the sample and its polarization analyzed using a second polarizing V-cavity. With this method, an initially polarized neutron beam is analysed after transmission through a sample. In the case of a ferromagnetic sample, the domain structure leads to a change in the polarization and typically, a decrease in the polarization is observed which is referred to as depolarization. In contrast, a purely paramagnetic sample does not affect the polarization of the neutron beam in transmission. Low temperatures and magnetic fields for this experiment were provided by a closed-cycle refrigerator and water-cooled Helmholtz coils, respectively. A small guide field of 0.5 mT was generated by means of permanent magnets. For further information on the neutron depolarization setup, we refer to Refs. [77, 136, 137].

All data shown as a function of temperature in this chapter were recorded at a fixed magnetic field under increasing temperature. Prior to this, we distinguish three different cases of applied magnetic fields during cool-down. The sample was either cooled (i) in zero magnetic field (zero-field cooling, zfc), (ii) with the field at the value applied during the measurement (field cooling, fc), or (iii) in a field of 250 mT (high-field cooling, hfc). For the magnetization data as a function of field, the sample was cooled in zero field. Subsequently, data were recorded during the initial increase of the field to +250 mT corresponding to a magnetic virgin curve, followed by a decrease to −250 mT, and a final increase back to +250 mT.

6.2 Phase Diagram and Bulk Magnetic Properties

The following section addresses the magnetometry and neutron deopolarization measurements and illustrates how the zero-field concentration-temperature magnetic phase diagram is inferred. Fig. 6.3(a) shows the full view of the phase diagram, the dotted red box indicates the detailed view depicted in Fig. 6.3(b).

Within the accuracy of the measurements and the readout of the transition temperatures, the data is in good agreement with the literature and the established phase borders mostly match with those published by Burke et al. [74–76]. Comparing the different physical properties in our study, we find that the imaginary part of the ac susceptibility displays the most pronounced signatures at the various phase transitions and crossovers. Therefore, the imaginary part was used to define the characteristic temperatures as discussed in the following. The same values are then marked in the different physical properties to highlight the consistency with alternative definitions of the characteristic temperatures based on these properties.

We distinguish four different regimes in the phase diagram, namely paramagnetism at high temperatures (PM, no shading), antiferromagnetic order for small values of x (AFM, green shading), ferromagnetic order for larger values of x (FM, blue shading),

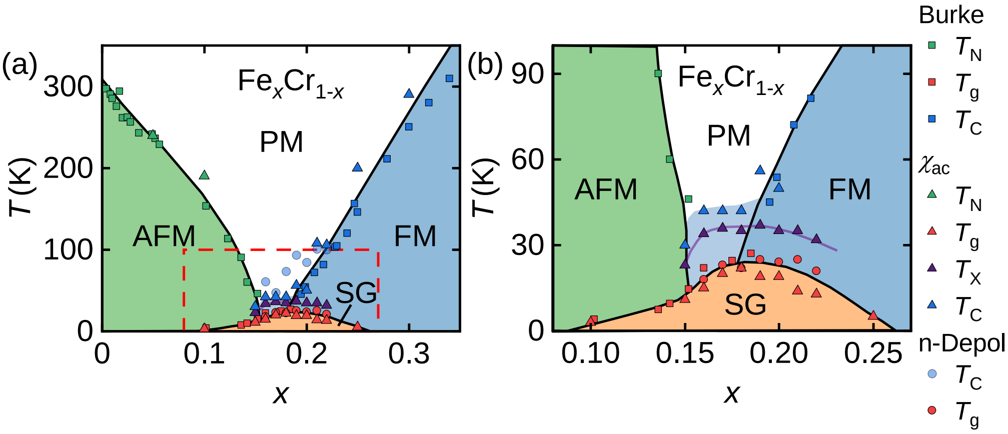

Figure 6.3: Zero-field concentration-temperature phase diagram of the Fe_xCr_{1-x} system, including data from Burke [74–76] as well as data from this thesis extracted from ac susceptibility and neutron depolarization. The following regimes are distinguished: paramagnetic (PM) antiferromagnetic (AFM), ferromagnetic (FM), spin glass (SG), and a precursor regime (purple line). (a) Overview. (b) Close-up view of the regime of spin-glass behavior as marked by the dashed box in panel (a).

and spin-glass behavior at low temperatures (SG, orange shading). Faint signatures reminiscent of those attributed to the onset of ferromagnetic order are observed in the susceptibility and neutron depolarization for $0.15 \leq x \leq 0.18$ (light blue shading). Furthermore, we observe a distinct precursor phenomenon preceding the spin-glass behavior at the temperature T_X (purple line) across a wide concentration range. Before presenting the underlying experimental data, we briefly summarize the key characteristics of the different regimes.

For the two samples $x = 0.05$ and $x = 0.10$, an antiferromagnetic transition is observed, which is exhibited by a sharp kink in the imaginary part of the ac susceptibility. Our values of T_N are consistent with previous reports [74, 80]. Furthermore, this transition is not sensitive to changes of the magnetic field, excitation frequency, or cooling history, as may be expected for magnetic transitions. The absolute value of the magnetization is small and it increases essentially linearly as a function of field in the parameter range studied.

For $0.18 \leq x$ ferromagnetic order is inferred from a maximum in the imaginary part of the ac susceptibility that shows a sensitivity to magnetic fields of the order of 10 mT. Moreover, similar to the antiferromagnetic transition discussed above, no shift of this feature with excitation frequencies is observed and hence it is identified as T_C. This interpretation is corroborated by the onset of neutron depolarization. Furthermore, the field dependence of the magnetization curves $M(H)$ for $0.18 \leq x$ displays hysteresis and a characteristic s-shaped form corroborating the indications for ferromagnetism. For $0.15 \leq x \leq 0.18$, we interpret faint signatures reminiscent of those observed for $0.18 \leq x$, such as a small shoulder instead of a maximum in the imaginary part of the ac susceptibility, in terms of an incipient onset of ferromagnetic order.

For $0.10 \leq x \leq 0.25$, spin glass behaviour is inferred from a pronounced maximum in the imaginary part of the ac susceptibility that is suppressed at intermediate magnetic fields of the order of 50 mT. This maximum displays a pronounced temperature shift with ac excitation frequencies, which is a common identifier for a glassy state and establishes this feature as the spin glass freezing temperature T_{g}. In addition, the temperature dependence of the magnetization and the neutron depolarization shows a branching between different cooling histories which is another well known indication for a glassy state.

In addition, we identify a precursor phenomenon in the range $0.15 \leq x \leq 0.22$ preceding the onset of spin-glass behavior at a temperature T_{X}. This phenomenon is inferred from a maximum in the imaginary part of the ac susceptibility that is suppressed in small magnetic fields reminiscent of the ferromagnetic transition. For concentrations $x \leq 0.20$, the rate of this shift is clearly less pronounced than the shift of the freezing temperature T_{g}. For concentrations $x \geq 0.21$, the shift of T_{X} becomes more pronounced than the shift of T_{g}. Interestingly, the magnetization and neutron depolarization exhibit no signatures at T_{X}.

6.2.1 Zero-Field AC Susceptibility

The real and imaginary parts of the zero-field ac susceptibility on a logarithmic temperature scale are shown in Figs. 6.4 and 6.5 for each sample studied.. The data were recorded with an excitation amplitude of $\mu_0 H_{\mathrm{ac}} = 1\,\mathrm{mT}$ at a frequency of 1000 Hz in zero magnetic field. Features and transition temperatures are marked by coloured arrows as well as lines and are most conveniently extracted from the imaginary part.

Starting at $x = 0.05$ in Fig. 6.4(a), the real part and the imaginary part are comparably small. In metallic specimens, such as $\mathrm{Fe}_x\mathrm{Cr}_{1-x}$, part of the dissipation detected via the imaginary part of the ac susceptibility arises from the excitation of eddy currents at the surface of the sample. Eddy current losses scale with the resistivity [138, 139] and in turn the kink at T_{N} reflects the distinct change of the electrical resistivity at the onset of long-range antiferromagnetic order. As will be shown below, this antiferromagnetic transition is identified by a high stability under magnetic field.

Increasing the Fe content to $x = 0.10$, shown in Fig. 6.4(b), leads to an increase in signal by one order of magnitude and the emergence of a maximum in the real part as well as two additional cusps at low temperatures in the imaginary part. The single maximum in the real part is observed for all following concentrations and can be explained by the broad overlap of the features from the various transitions, masking the underlying behaviour. Therefore, the imaginary part is used in the following to distinguish between features. In the imaginary part, the high-temperature maximum that tracks T_{N} has decreased to 190 K. The weak maximum at $\approx 40\,\mathrm{K}$ is attributed

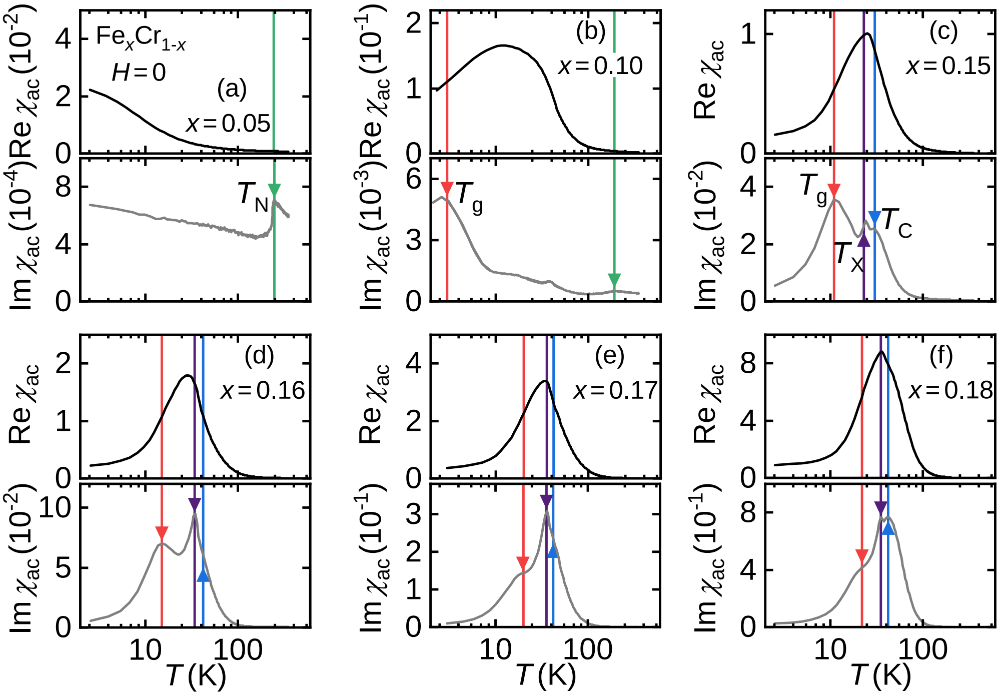

Figure 6.4: Temperature dependence of the zero field ac susceptibility for the six concentrations $0.05 \leq x \leq 0.18$ investigated in this work. For each concentration, the upper and lower panel shows the real part Reχ_{ac} and the imaginary part Imχ_{ac}, respectively. Green, blue, red, and purple arrows indicate features that track the antiferromagnetic, ferromagnetic, spin glass, and X transition temperatures.

to a small amount of ferromagnetic impurities in the sample based on the small magnitude of the signal. The low-temperature cusp at 3 K, indicated by the red arrow, is attributed to a spin glass freezing temperature T_g. As will be demonstrated below, this is accounted for by a pronounced frequency-dependent shift, a sensitivity of T_g in magnetic fields of the order of 250 mT, and a characteristic branching between zero-field cooled, field cooled, and high-field cooled magnetization curves below T_g.

Fig. 6.4(c) shows the concentration $x = 0.15$ where the signal size has increased further, but no qualitative change is observed in the real part. In the imaginary part, three cusps are identified. The feature at the highest temperature is attributed to a ferromagnetic transition $T_C = 30$ K as indicated by the blue arrow, which is distinguished from the antiferromagnetism in the previous concentrations as follows. In contrast to the antiferromagnetism, the feature that tracks the ferromagnetism is not stable but sensitive to small magnetic fields of the order of 10 mT and the magnetization curve exhibits a characteristic s-shape, as will be elaborated below. Moreover, there is a cusp at the intermediate temperature 23 K that is denoted with

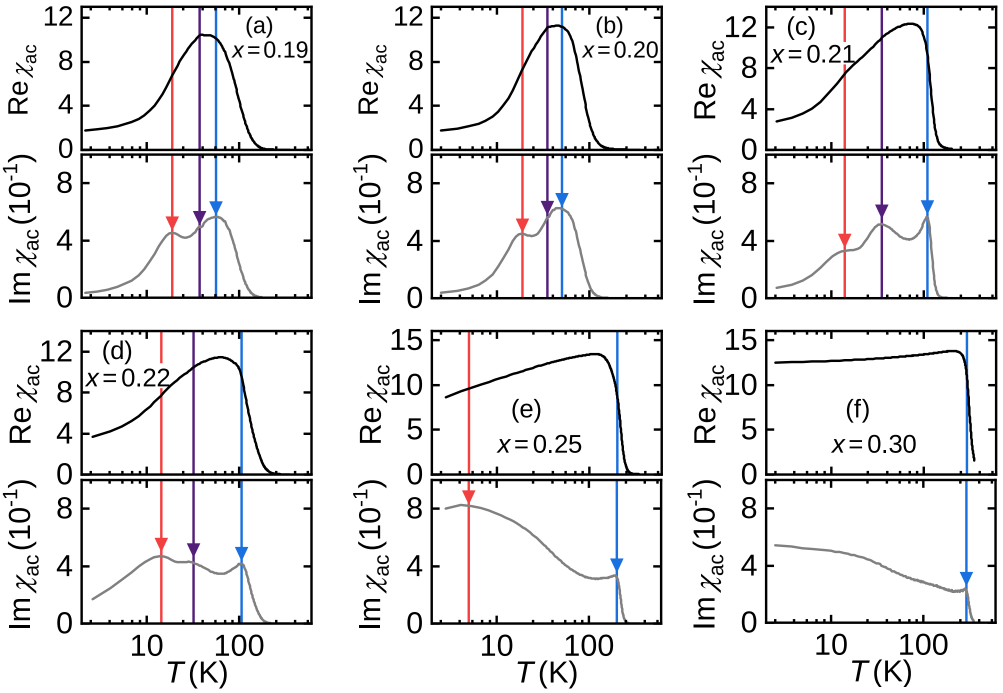

Figure 6.5: Temperature dependence of the zero field ac susceptibility for for the six concentrations $0.19 \leq x \leq 0.30$ investigated in this work. For each concentration, the upper and lower panel shows the real part Reχ_{ac} and the imaginary part Imχ_{ac}, respectively. Green, blue, red, and purple arrows indicate features that track the antiferromagnetic, ferromagnetic, spin glass, and X transition temperatures.

T_{X} and indicated by the purple arrow. This transition is characterized by a frequency dependency similar to T_{g} but a sensitivity to small magnetic fields of 10 mT similar to T_{C}, as will be shown below. For these reasons, it is argued that T_{X} tracks a separate transition. The third low temperature feature corresponds to the spin glass freezing temperature which has increased to $T_{\mathrm{g}} = 11\,\mathrm{K}$.

The qualitative shape of the real and imaginary parts remains unchanged in the concentration range $0.16 \leq x \leq 0.22$, shown in Figs. 6.4(d)-(e) and Figs. 6.4(a)-(d). The absolute signals increase with x and the positions of T_{C}, T_{X}, and T_{g} change. Within the experimental resolution T_{C} is steadily increasing with x. T_{X} shows a distinct increase from $x = 0.15$ to $x = 0.16$ followed by small changes in the range $0.16 \leq x \leq 0.22$. T_{g} increases with x to a maximum of 22 K, and at $x = 0.18$ decreases under further increasing x.

At $x = 0.25$, shown in Fig. 6.5(e), T_{X} can no longer be observed indicating that the precursor regime has vanished. The imaginary part exhibits a further increase of T_{C}, T_{g} is observed to have decreased further. Finally, Fig. 6.5(f) shows the highest measured concentration $x = 0.30$ where a pronounced ferromagnetic transition T_C is present and T_g can no longer be observed. It is concluded that the spin glass phase vanishes in the concentration region $x \gtrsim 25$, which is also in agreement with the percolation limit of 24.3 % in the present crystal structure. We refer to Tab. 6.1 for a summary of the transition temperatures including their error bars.

6.2.2 Magnetization and ac Susceptibility under Applied Magnetic Fields

In order to distinguish between the different regimes, the behaviour of the transition temperatures T_N, T_C, T_X, and T_g under magnetic fields up to 250 mT is studied.

Fig. 6.6 depicts the temperature dependence of (i) the real part $\mathrm{Re}\chi_\mathrm{ac}$, (ii) the imaginary part $\mathrm{Im}\chi_\mathrm{ac}$, and (iii) the magnetization M for selected magnetic fields up to 250 mT, for selected concentrations in the range $0.05 \leq x \leq 0.30$. In Figs. 6.6(iii), data after zero-field cooling, field-cooling and high-field cooling are depicted with continuous, dotted, and dashed lines, respectively. In addition, the field dependence of the magnetization at a temperature of 2 K is depicted in Fig. 6.7 for the same concentrations.

Starting at $x = 0.05$ in Fig. 6.6(a), both the real part and the imaginary part show no significant changes under magnetic fields. As mentioned above, the antiferromagetic transition is characterized by this stability and no change in T_N is observed under magnetic fields up to 250 mT. The temperature dependence of the magnetization exhibits a decrease in signal at low temperatures with increasing magnetic field and no splitting between zero-field cooled, field cooled, and high-field cooled branches is observed. The field dependence of the magnetization in Fig. 6.7(a) shows non-linear behaviour with a small curvature and no hysteresis.

At $x = 0.15$, shown in Fig. 6.6(b), in contrast the real part is gradually decreasing with increasing magnetic field. The imaginary part at T_g increases in fields up to 10 mT and decreases only for higher fields. The actual dependence of the different transitions T_C, T_X, and T_g on magnetic fields can be conveniently observed in the imaginary part. T_C and T_X are just observable at 10 mT and are completely unobservable at the latest at 50 mT. This characteristic field dependence is used to distinguish the ferromagnetic from the antiferromagnetic phase, which, in contrast, appears to be very robust under magnetic fields. The freezing temperature T_g is first increasing for fields from 0 mT to 10 mT and than decreasing gradually from 10 mT to 250 mT. This behaviour contrasts the concentrations $x = 0.17$, 0.18, 0.22, and 0.30, which all display a gradually decreasing signal over the entire temperature range. The feature marking T_g is still weakly present in the maximum field which is used to distinguish the spin glass from the antiferromagnetic, ferromagnetic, and precursor transitions. In general, the temperature dependence of the magnetization shows a similar behaviour as in Fig. 6.6(a) but there is a clear branching depending on the cooling history below T_g, which is a characteristic identifier for a glassy state. This phenomenon is observed for all concentrations in the range $0.10 \leq x \leq 0.25$ and hence corroborates the spin glass phase boundaries established from the ac susceptibility in Fig. 6.4 and Fig. 6.5. A characteristic s-shape accompanied by hysteresis is observed in the field dependence of the magnetization in Fig. 6.7(b), in agreement with ferromagnetic behaviour at $x = 0.15$.

For the three next higher concentrations $x = 0.17$, 0.18, 0.22, shown in Figs. 6.6(c)-(e), the field dependencies remain qualitatively the same. The absolute signals of the real part, the imaginary part, and the magnetization increase and the width of the hysteresis in the field dependence of the magnetization in Figs. 6.7(c)-(e) decreases with increasing x. The positions of T_{C}, T_{X}, and T_{g} change with x, consistent with the previous descriptions.

Lastly Fig. 6.6(f) depicts the highest concentration $x = 0.30$. Here, the real part and the imaginary part exhibit a pronounced kink at T_{C} that is sensitive too magnetic fields. Neither T_{X} nor T_{g} are observed. The temperature dependence of the magnetization shows no splitting in agreement with a vanished spin glass phase and the field dependence of the magnetization in Fig. 6.7(f) shows a pronounced s-shape without resolvable hysteresis in agreement with ferromagnetism.

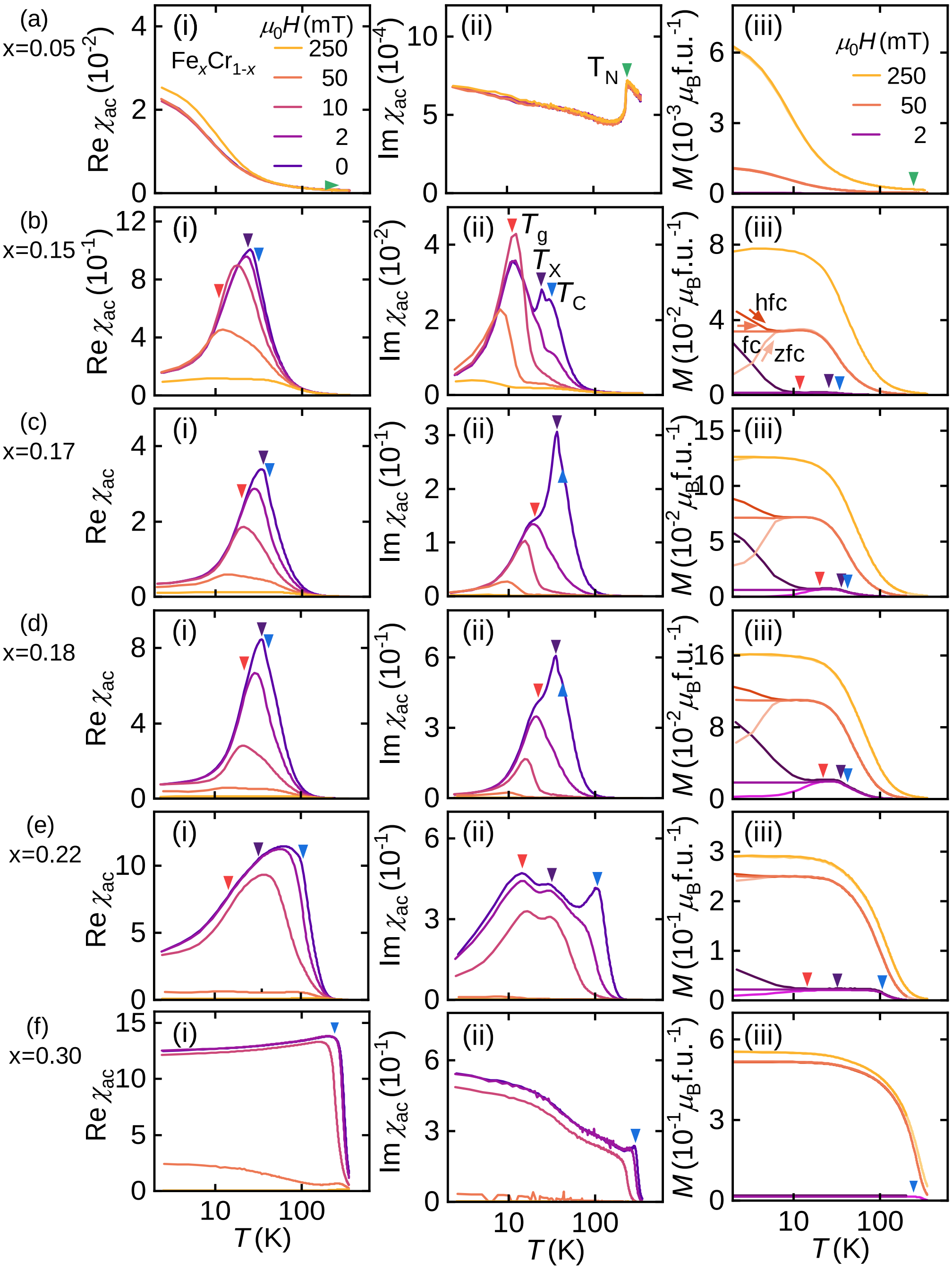

Figure 6.6: Temperature dependence of the magnetization and the ac susceptibility in fields up to 250 mT for selected concentrations. From top to bottom: (a) $x = 0.05$, (b) $x = 0.15$, (c) $x = 0.17$, (d) $x = 0.18$, (e) $x = 0.22$, (f) $x = 0.30$. From left to right: (i) the real part Reχ_{ac}, (ii) the imaginary part Imχ_{ac}, and (iii) the magnetization.

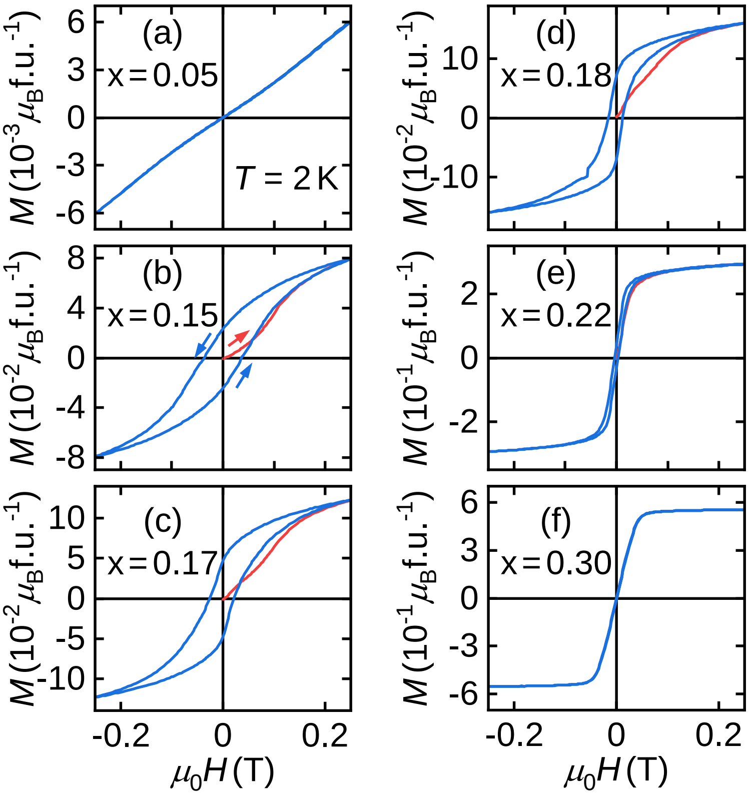

Figure 6.7: Field dependence of the magnetization at a temperature of 2 K in fields up to 250 mT for selected concentrations. (a) $x = 0.05$, (b) $x = 0.15$, (c) $x = 0.17$, (d) $x = 0.18$, (e) $x = 0.22$, (f) $x = 0.30$.

Table 6.1: Transition temperatures in Fe_xCr_{1-x} observed in ac susceptibility, magnetization, and neutron depolarization. Antiferromagnetic, ferromagnetic, precursor, and spin glass regions were found with corresponding transition temperatures T_N, T_C, T_X, and T_g, most conveniently extracted from the imaginary part of the ac susceptibility $\mathrm{Im}\chi_{ac}$. In neutron depolarization measurements the ferromagnetic and spin glass transitions denoted with $T_{f,D}$ and $T_{C,D}$ are observed. The errors in reading the exact transition temperatures are estimated.

x	T_N (K)	T_g (K)	T_X (K)	T_C (K)	$T_{f,D}$ (K)	$T_{C,D}$ (K)
0.05	240 ± 5	-	-	-	-	-
0.10	190 ± 5	3 ± 5	-	-	-	-
0.15	-	11 ± 2	23 ± 3	30 ± 10	-	-
0.16	-	15 ± 2	34 ± 3	42 ± 10	18 ± 5	61 ± 10
0.17	-	20 ± 2	36 ± 3	42 ± 10	23 ± 5	47 ± 2
0.18	-	22 ± 2	35 ± 3	42 ± 10	22 ± 5	73 ± 1
0.19	-	19 ± 2	37 ± 5	56 ± 10	25 ± 5	93 ± 1
0.20	-	19 ± 2	35 ± 5	50 ± 10	24 ± 5	84 ± 1
0.21	-	14 ± 2	35 ± 5	108 ± 5	25 ± 5	101 ± 1
0.22	-	13 ± 2	32 ± 5	106 ± 5	21 ± 5	100 ± 1
0.25	-	5 ± 5	-	200 ± 5	-	-
0.30	-	-	-	290 ± 5	-	-

6.2.3 Neutron Depolarization

Next, the neutron depolarization of samples in the central composition range $0.15 \leq x \leq 0.22$ is studied in order to infer further information on the microscopic nature of the different magnetic states.

Fig. 6.8 shows neutron depolarization measurements in a guidance field smaller than 0.5 mT for concentrations in the range $0.15 \leq x \leq 0.22$. The zero-field cooled and high-field cooled scans as well as the exponential fit to the zero-field cooled branch are coloured in black, grey, and orange, respectively. At $x = 0.15$ in Fig. 6.8(a), both zero-field cooled and high-field cooled depolarization curves are essentially at a constant value of 1 within the $\approx 1\,\%$ accuracy of the measurement. The lack of depolarization is due to this concentration being at the border to antiferrromagnetism. Only a small volume fraction of the $x = 0.15$ sample orders ferromagnetically and no drop in the average depolarization of the whole sample volume is observed. Nevertheless, a splitting between the zero-field cooled and high-field cooled branch may just be identified by about 1 %. For $x = 0.16$ in Fig. 6.8(b), a decrease of polarization below a temperature of $\approx 50\,\mathrm{K}$ is observed, suggesting the presence of ferromagnetic domains. T_C, indicated by the blue arrow, is extracted with the help of an exponential fit as described below. The incomplete drop to $P \approx 0.96$ suggests that only a fraction of the sample volume orders ferromagnetically. Furthermore, the smeared appearance of the transition suggests a broad distribution of transition temperatures that could be explained by different sized clusters and single spins in the sample. The detailed view in the inset shows an additional drop in polarization below 18 K that occurs in close proximity to the $T_\mathrm{g} = 15\,\mathrm{K}$ from the susceptibility data. To conclude, the spin glass transition can be identified in the depolarization data by an additional drop near the spin glass freezing temperature. Within the accuracy of the measurement no difference between the zero-field cooled and high-field cooled branch is observed.

Fig. 6.8(c) shows $x = 0.17$, where again two successive drops in the polarization are present. Similar to $x = 0.16$, the decrease at the higher temperature tracks T_C, and the decrease at the lower temperature is attributed to T_g. In agreement with the magnetometry data, both temperatures have increased. Moreover, the absolute size of the polarization loss has increased compared to $x = 0.16$ which suggests a larger ferromagnetic volume fraction. Furthermore, there is a pronounced difference between the high-field cooled and zero-field cooled polarization below T_g analogous to the splitting observed in the magnetization branches in Figs. 6.6(iii). The following two concentrations $x = 0.18$ and $x = 0.19$, shown in Figs. 6.8(d) and (e), display similar behaviour to $x = 0.17$ but a larger polarization loss, indicating a larger ferromagnetic volume fraction of the sample. Both T_C and T_g increase to higher temperatures with increasing x. For $x = 0.20$ in Fig. 6.8(f), the branching between the zero-field cooled and high-field cooled polarization is not observed and T_C has decreased again, in contrast to the observation that T_C increases with x. Apart from that, the decrease of T_g and the overall behaviour are in agreement with previous results.

Fig. 6.8(g) shows $x = 0.21$ where the splitting between the zero-field cooled and high-field cooled polarization is again observed. The deviation between the two branches already sets in at a higher temperature than T_g. Nevertheless, the increase in T_C and the decrease in T_g are in agreement with previously observed behaviour. The highest concentration $x = 0.22$ is depicted in Fig. 6.8(h). The polarization decreases almost to zero indicating a large volume fraction of ferromagnetic sample. T_C has increased to its highest value so far, T_g has decreased, and a splitting between the high-field cooled and zero-field cooled branch is not observed. The transition temperatures inferred from the neutron depolarization are summarized in Tab. 6.1.

In the following the fitting procedure to the zero-field cooled polarization, which was used to extract T_C and to estimate a mean size and characteristic time of ferromagnetic domains, is described. Consider the passage of polarized neutrons through an ensemble of randomly oriented domains for small spin rotations per domain $\omega_\mathrm{L}\tau \ll 2\pi$, where ω_L is the Larmor frequency and τ is the flight time of the neutron through the sample. As derived by Halpern and Holstein [140], in this case, the temperature dependence of the neutron polarization can be simplified to

$$P(T) = \exp\left[-\frac{1}{3}\gamma^2 B_0^2(T)\frac{d\delta}{v^2}\right]. \tag{6.1}$$

where γ is the gyromagnetic ratio of the neutron, $B_0(T)$ is the temperature dependent average magnetic flux per domain, d is the sample thickness in flight direction, δ is the mean domain size, and v is the speed of the neutrons. For $B_0(T)$, it is assumed that the temperature dependence can be described by the form known from the mean field approximation

$$B_0(T) = {\mu_0}^2 {M_0}^2 \left(1 - \frac{T}{T_\mathrm{C}}\right)^\beta \tag{6.2}$$

where μ_0 is the vacuum permeability and the critical exponent β is fixed to 0.5 corresponding to a mean field ferromagnet. M_0 is the spontaneous magnetization in each domain which is approximated with the value at 2 K under a field of 250 mT extracted from the magnetization measurements.

Fitting the temperature dependence of the polarization for temperatures above T_g according to Eq. 6.1, cf. solid orange lines in Fig. 6.8 nicely tracking the experimental data, yields mean values for the Curie temperature T_C and the domain size δ. The results of the fitting are summarized in Tab. 6.2.

The values of T_C inferred that way are typically slightly higher than those inferred from the ac susceptibility, cf. Tab. 6.1, but both values are in reasonable agreement. The mean size of ferromagnetically aligned domains or clusters, δ, increases with increasing x. As will be shown below, this general trend is corroborated also by an analysis of the Mydosh parameter indicating that $\mathrm{Fe}_x\mathrm{Cr}_{1-x}$ transforms from a cluster glass for small x to a superparamagnet for larger x.

Table 6.2: Summary of the Curie temperature, T_C, and the mean domain size, δ, in $\mathrm{Fe}_x\mathrm{Cr}_{1-x}$ as inferred from neutron depolarization studies. Also shown is the magnetization measured at a temperature of 2 K in a magnetic field of 250 mT, M_0.

x	T_C^D (K)	δ (μm)	M_0 (10^5A/m)
0.15	-	-	0.70
0.16	61 ± 10	0.61 ± 0.10	0.84
0.17	47 ± 2	2.12 ± 0.15	0.96
0.18	73 ± 1	3.17 ± 0.07	1.24
0.19	93 ± 1	3.47 ± 0.02	1.64
0.20	84 ± 1	4.67 ± 0.03	1.67
0.21	101 ± 1	3.52 ± 0.03	2.18
0.22	100 ± 1	5.76 ± 0.13	2.27

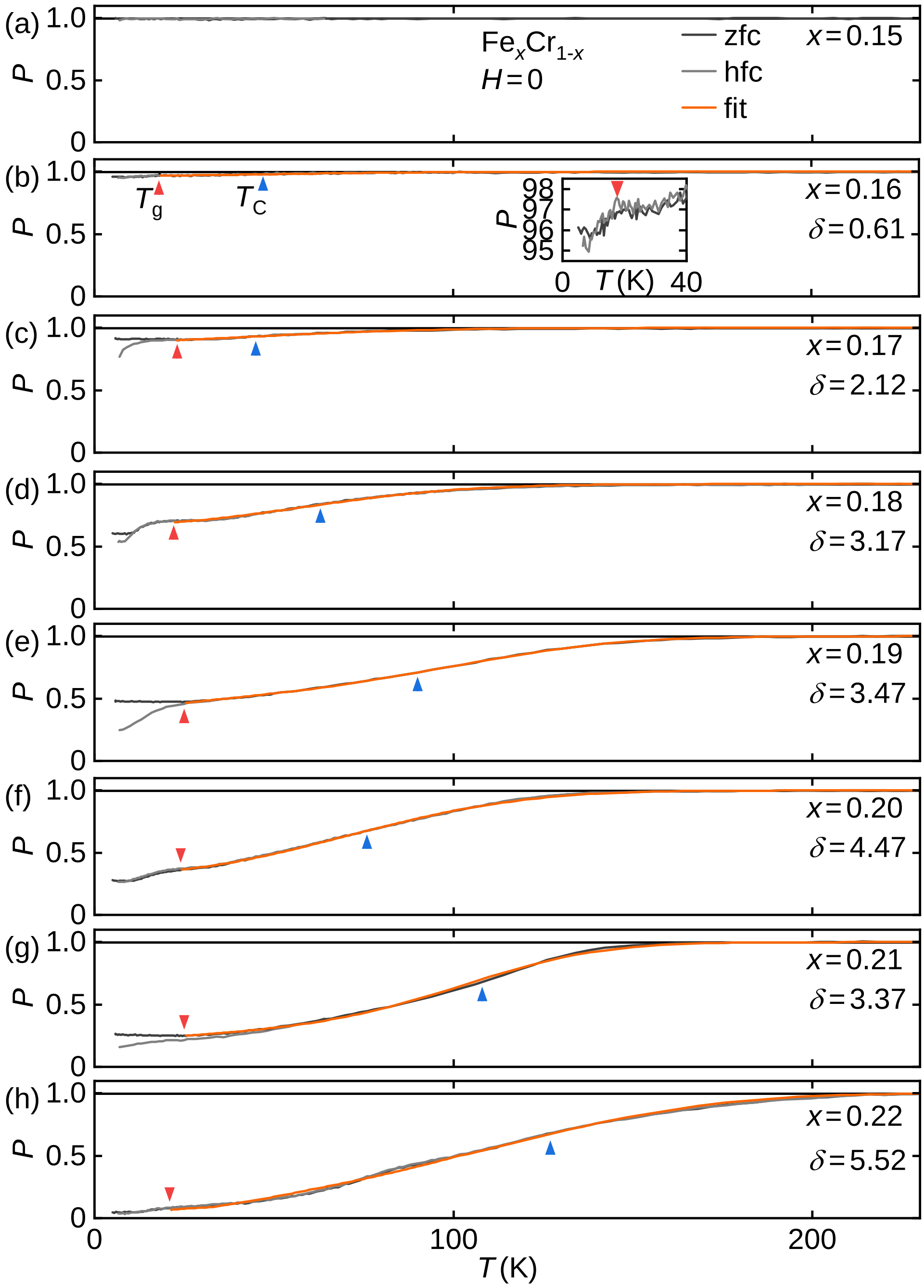

Figure 6.8: Neutron depolarization of Fe$_x$Cr$_{1-x}$ as a function of temperature for $0.15 \leq x \leq 0.22$. Data were measured in zero magnetic field under increasing temperature following initial zero-field cooling or high-field cooling in 250 mT. Colored arrows mark the Curie transition T_C and the freezing temperature T_g. Orange solid lines are fits to the experimental data, see text for details.

6.2.4 Specific heat, High-Hield Magnetometry, and Electrical Resistivity

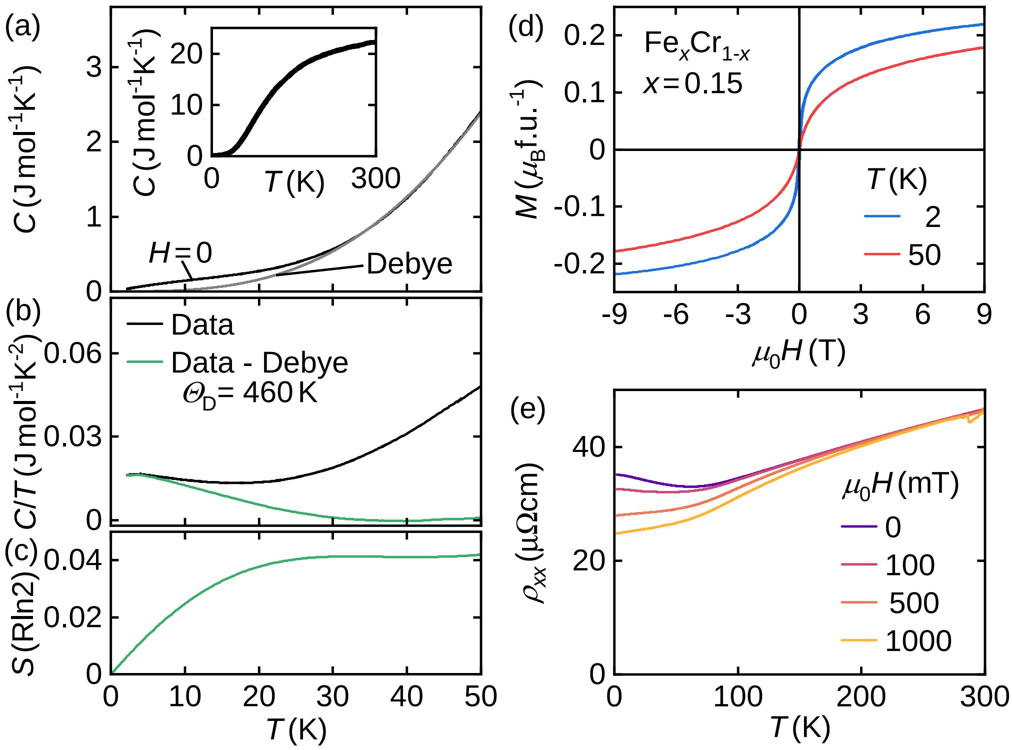

Figure 6.9: Specific heat, electrical transport and high-field magnetization for $x = 0.15$. (a) Temperature dependence of the heat capacity in zero field (black) and the Debye model (grey) for temperatures below 50 K. The inset shows the heat capacity over the entire temperature range. (b) Temperature dependence of the heat capacity divided by temperature $C(T)/T$ in zero field (black) and the difference of the former and the Debye model (green) for temperatures below 50 K. (c) Temperature dependence of the entropy obtained from integrating the difference of $C(T)/T$ and the Debye model along T. (d) Magnetization in magnetic fields up to 9 T for selected temperatures. (e) Electrical resistivity in selected magnetic fields.

The magnetic properties at low fields presented so far are complemented by exemplaric measurements of the specific heat, the high-field magnetization, and the electrical resistivity on $x = 0.15$.

The temperature dependence of the specific heat in zero field, coloured in black, is depicted in Fig. 6.9(a) in the range from 2 K to 50 K, the inset shows the entire temperature range from 2 K to 300 K. The curve displays no sharp features in the proximity of $T_C = 30\,K$, $T_X = 23\,K$ or $T_g = 11\,K$, where signatures in the imaginary part of the ac susceptibility are observed. A fit with the Debye model for $\Theta_D = 460\,K$, depicted in grey, shows a good agreement with the data for temperatures above $\approx 30\,\mathrm{K}$. Fig. 6.9(b) shows the specific heat divided by the temperature $C(T)/T$, depicted in black, and the difference between specific heat and Debye model divided by the temperature, depicted in green, which corresponds to the magnetic contribution. Below a temperature of $\approx 30\,\mathrm{K}$, the specific heat displays a broad increase in the vicinity of T_g, as commonly observed in spin glasses [95]. This additional contribution could stem from a broad overlap of the features of the three transitions T_C, T_X and T_g, similarly observed in the real part of the ac susceptibility. The entropy is depicted in Fig. 6.9(c) as calculated by means of extrapolating C/T to zero temperature and numerically integrating

$$S(T) = \int_0^T \frac{C(T)}{T}\,\mathrm{d}T. \tag{6.3}$$

The magnetic contribution to the entropy released up to 30 K amounts to about $0.04\,R\ln 2$, which corresponds to a small fraction of the total magnetic moment only.

Fig. 6.9(d) shows the field dependence of the magnetization for temperatures of $2\,\mathrm{K}$, $10\,\mathrm{K}$, and $50\,\mathrm{K}$ for $x = 0.15$. The overall signal decreases with increasing temperature and no saturation is observed. All curves show non-linear behaviour and a characteristic s-shape reminding of ferromagnetism, even at $50\,\mathrm{K}$ clearly above T_C. The s-shape at $50\,\mathrm{K}$ is attributed to magnetic correlations that emerge already well-above the onset of long-range ferromagnetic order at T_C.

The temperature dependence of the electrical resistivity in zero field and in fields of $10\,\mathrm{mT}$, $100\,\mathrm{mT}$, $500\,\mathrm{mT}$, and $1000\,\mathrm{mT}$ is depicted in Fig. 6.9(e). With increasing temperature, the zero-field curve displays a steady decrease to a minimum at approximately $60\,\mathrm{K}$ before the resistivity increases towards low temperatures. Such an incipient divergence of the resistivity with decreasing temperature due to magnetic impurities is reminiscent of single-ion Kondo systems [141–144]. When applying magnetic field, the increase below $60\,\mathrm{K}$ becomes less pronounced. The qualitative behaviour of our data is in agreement with investigations on $\mathrm{Fe}_x\mathrm{Cr}_{1-x}$ for $0 \leq x \leq 0.112$ reported by Arajs et al. [145].

6.3 Characterization of the Spin Glass State

The observed spin glass state in the concentration range $0.10 \leq x \leq 0.25$ at low temperatures is identified by a cusp in the imaginary part of the ac susceptibility that shifts to higher temperatures with increasing ac excitation frequency. In the following the analysis of this shift by means of the Mydosh parameter, the Vogel-Fulcher law and a power law fit is presented.

6.3.1 Mydosh Parameter

Fig. 6.10(a) shows the imaginary part of the ac susceptibility, $\mathrm{Im}\chi_{\mathrm{ac}}$, for $x = 0.15$ in zero magnetic field for temperatures between 2 K and 18 K measured with ac excitation frequencies ranging from 10 Hz to 10 000 Hz. As discussed above, the maximum in $\mathrm{Im}\chi_{\mathrm{ac}}$ is attributed to the freezing temperature T_{g} of the spin glass state. With increasing frequency, $\mathrm{Im}\chi_{\mathrm{ac}}$ increases and the maximum shifts to higher temperatures. From this dependence of the peak, the so-called Mydosh parameter ϕ can be calculated [93, 95]:

$$\phi = \left[\frac{T_{\mathrm{g}}(f_{\mathrm{high}})}{T_{\mathrm{g}}(f_{\mathrm{low}})} - 1\right]\left[\ln\left(\frac{f_{\mathrm{high}}}{f_{\mathrm{low}}}\right)\right]^{-1} \tag{6.4}$$

where $T_{\mathrm{g}}(f_{\mathrm{high}})$ and $T_{\mathrm{g}}(f_{\mathrm{low}})$ are the freezing temperatures as experimentally observed at high and low excitation frequencies, f_{high} and f_{low}, respectively. The Mydosh parameter is used to distinguish between spin glass, cluster glass and superparamagnet. Typical values for this parameter are $\phi \leq 0.01$ for canonical spin glasses like Mn_xCu_{1-x}, $0.01 \leq \phi \leq 0.1$ for cluster glasses and $\phi \geq 0.1$ for superparamagnets [93, 95, 146, 147].

Fig. 6.11 depicts the concentration dependence of the Mydosh parameter ϕ, the values are summarized in Tab. 6.3. An inaccuracy of T_{g} of up to 0.4 K depending on the concentration is estimated, which leads in turn to a considerable error of ϕ as displayed by the error bars in Fig. 6.11. In our Fe_xCr_{1-x} samples, ϕ increases from a cluster glass-like value to a superparamagnetic value with the concentration x. This evolution reflects the increase of the mean size of ferromagnetic clusters as inferred from the analysis of the neutron depolarization data presented above.

6.3.2 Characteristic Time and Power Law

Another approach for characterizing the spin glass state is the standard theory for dynamical scaling near a phase transition at T_{g}. Hohenberg et al. [148] established a power law which is frequently used for this analysis [93]:

$$\tau = \tau_0 \left[\frac{T_{\mathrm{g}}(f)}{T_{\mathrm{g}}(0)} - 1\right]^{z\nu} \tag{6.5}$$

with the decay time $\tau = \frac{1}{2\pi f}$, the characteristic time τ_0, the zero-frequency limit of the spin glass freezing temperature $T_{\mathrm{g}}(0)$, and the critical exponent $z\nu$. Typical values for canonical spin glasses such as $\mathrm{Mn}_x\mathrm{Cu}_{1-x}$ are $\tau_0 = 10^{-13}\,\mathrm{s}$, $T_\mathrm{g}(0) = 27.5\,\mathrm{K}$, and $z\nu = 5$ [149].

In order to analyse $\mathrm{Fe}_x\mathrm{Cr}_{1-x}$ with this power law, the logarithm of the decay time $\ln(\tau)$ is plotted versus the logarithm of the freezing temperature divided by the zero-frequency freezing temperature minus one $\ln(\frac{T_\mathrm{g}(f)}{T_\mathrm{g}(0)} - 1)$ for various $T_\mathrm{g}^\mathrm{est}(0)$. For each $T_\mathrm{g}^\mathrm{est}(0)$, a linear fit is performed and the statistically best fit yields $T_\mathrm{g}(0)$. In the next step, the characteristic time τ_0 and the critical exponent $z\nu$ are extracted from the linear fit with $T_\mathrm{g}(0)$. This process is shown exemplary in Fig. 6.10(b) for $x = 0.15$ where the goodness of fit R^2 is plotted versus varying $T_\mathrm{g}^\mathrm{est}(0)$ and the highest R^2, implying the best fit, is obtained for $T_\mathrm{g}(0) = 9.1\,\mathrm{K}$. With this value of $T_\mathrm{g}(0)$, $\ln(\tau)$ versus $\ln(\frac{T_\mathrm{g}(f)}{T_\mathrm{g}(0)} - 1)$ is depicted in Fig. 6.10(c). The linear fit, depicted in red, yields $z\nu \approx 5$ and $\tau_0 = 1.6 \times 10^{-7}\,\mathrm{s}$ for $x = 0.15$.

This analysis was performed for all concentrations and characteristic times τ_0 in the range $10^{-7}\,\mathrm{s} \leq \tau_0 \leq 10^{-5}\,\mathrm{s}$ were extracted, several orders of magnitude larger than for canonical spin glasses and in agreement with the presence of large clusters of magnetic moments. The critical exponents fall within the range $2 \leq z\nu \leq 7$ as expected for glassy systems [146, 149]. No systematic evolution of neither τ_0 nor $z\nu$ with the concentration x was observed. An overview of the parameters for all concentrations can be found in Tab. 6.3.

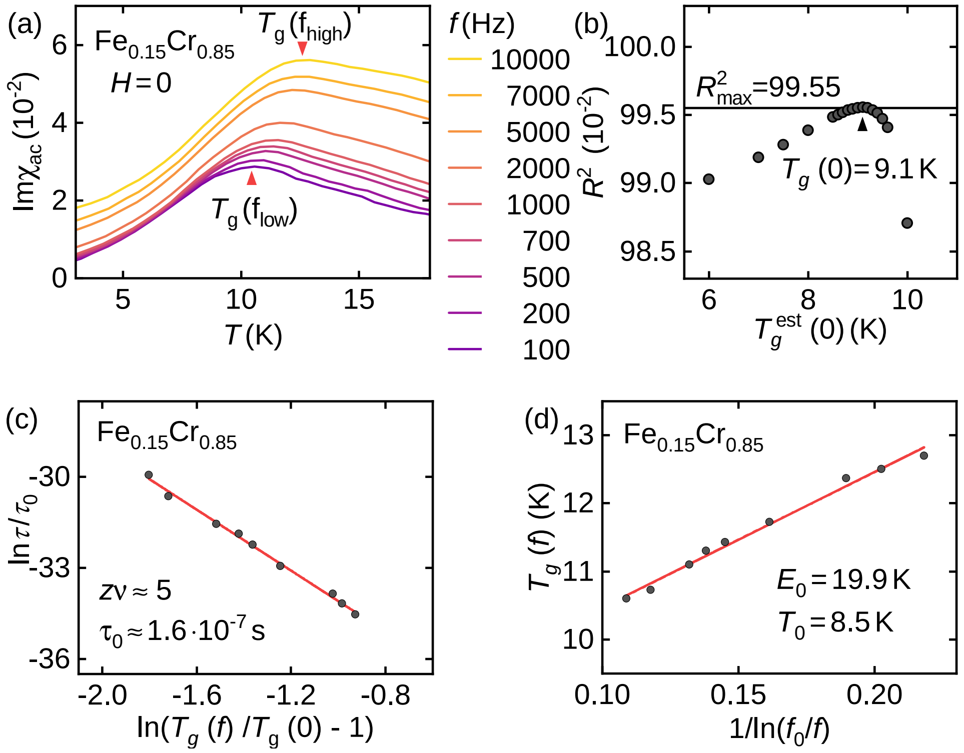

Figure 6.10: Frequency dependence of the spin glass transition, Vogel–Fulcher law and power law fit in $Fe_{0.15}Cr_{0.85}$. (a) Imaginary part of the zero-field ac susceptibility as a function of temperature measured at different excitation frequencies f. Analysis of the frequency-dependent shift of the spin freezing temperature T_g allows to gain insights on the microscopic nature of the spin-glass state. (b) Goodness of fit for different estimated zero-frequency extrapolations of the freezing temperature, $T_g^{est}(0)$. The value $T_g(0)$ used in (c) is defined as the temperature of highest R^2. (c) Logarithm of the relaxation time as a function of the logarithm of the normalized shift of the freezing temperature. The red solid line is a power law fit allowing to infer the characteristic relaxation time τ_0 and the critical exponent $z\nu$. (d) Spin freezing temperature as a function of the inverse of the logarithm of the ratio of characteristic frequency and excitation frequency. The red solid line is a fit according to the Vogel–Fulcher law allowing to infer the cluster activation energy E_a and the Vogel–Fulcher temperature T_0.

6.3.3 Vogel-Fulcher Analysis

The empirical Vogel-Fulcher law describes the viscosity of supercooled liquids, e.g. glasses, and can be applied in a spin-glass system to interpret the data near the freezing temperature T_g [93, 146, 150, 151]. With the relaxation times τ_0, determined via the power law fit as described above, the characteristic frequency $f_0 = 1/2\pi\tau_0$ may be calculated. The Vogel-Fulcher law may be written as:

$$f = f_0 \exp\left\{ -\frac{E_a}{k_\mathrm{B}[T_\mathrm{g}(f) - T_0]} \right\} \tag{6.6}$$

with k_B the Boltzmann constant and E_a the cluster activation energy, which has to be overcome in order to align the magnetic moments of the clusters with the external magnetic field. T_0 is the Vogel-Fulcher temperature which may be interpreted as a measure of the cluster interaction strength. Typical values for canonical spin glasses such as $\mathrm{Mn}_x\mathrm{Cu}_{1-x}$ are $E_a/k_B = 11.8\,\mathrm{K}$ and $T_0 = 26.9\,\mathrm{K}$ [149].

The Vogel-Fulcher analysis is performed by linear fitting the freezing temperature $T_\mathrm{g}(f)$ plotted against the inverse of the logarithm of the characteristic frequency divided by the frequency $1/\ln(f_0/f)$, as depicted in Fig. 6.10(d) for $x = 0.15$. From the slope and the intercept the parameters $E_0 = E_a/k_B = 19.9\,\mathrm{K}$ and $T_0 = 8.5\,\mathrm{K}$ are derived for $x = 0.15$. The analysis of all concentrations revealed positive values of T_0 indicating strongly correlated clusters [151–153] but no systematic evolution of neither E_0 nor T_0 with the concentration x. Tab. 6.3 summarizes the parameters for all concentrations.

Table 6.3: Parameters inferred from the analysis of the spin-glass behavior in Fe_xCr_{1-x}, namely the Mydosh parameter ϕ, the zero-frequency extrapolation of the spin freezing temperature $T_{\mathrm{g}}(0)$, the characteristic relaxation time τ_0, the critical exponent $z\nu$, the Vogel–Fulcher temperature T_0, and the cluster activation energy E_a. The errors were determined by means of Gaussian error propagation (ϕ), the distance of neighboring data points ($T_{\mathrm{g}}(0)$), and statistical deviations of the linear fits (τ_0, $z\nu$, T_0, and E_a).

x	ϕ	$T_{\mathrm{g}}(0)$ (K)	τ_0 (10^{-6} s)	$z\nu$	T_0 (K)	E_a (K)
0.05	-	-	-	-	-	-
0.10	0.064 ± 0.011	-	-	-	-	-
0.15	0.080 ± 0.020	9.1 ± 0.1	0.16 ± 0.03	5.0 ± 0.1	8.5 ± 0.1	19.9 ± 0.8
0.16	0.100 ± 0.034	13.4 ± 0.1	1.73 ± 0.15	2.2 ± 0.0	11.9 ± 0.1	14.4 ± 0.3
0.17	0.107 ± 0.068	18.3 ± 0.1	6.13 ± 1.52	1.5 ± 0.1	16.3 ± 0.3	12.8 ± 0.9
0.18	0.108 ± 0.081	14.5 ± 0.1	1.18 ± 0.46	7.0 ± 0.5	16.9 ± 0.5	24.2 ± 2.3
0.19	0.120 ± 0.042	14.2 ± 0.1	0.47 ± 0.15	4.5 ± 0.2	14.6 ± 0.4	16.3 ± 1.4
0.20	0.125 ± 0.043	13.5 ± 0.1	1.29 ± 0.34	4.1 ± 0.2	13.6 ± 0.3	18.8 ± 1.3
0.21	0.138 ± 0.048	9.5 ± 0.1	1.67 ± 0.21	4.7 ± 0.1	10.3 ± 0.4	12.0 ± 1.3
0.22	0.204 ± 0.071	11.7 ± 0.1	2.95 ± 0.80	2.6 ± 0.1	11.3 ± 0.4	11.3 ± 1.2
0.25	0.517 ± 0.180	2.8 ± 0.1	75.3 ± 5.34	1.8 ± 0.1	n.a.	n.a.
0.30	-	-	-	-	-	

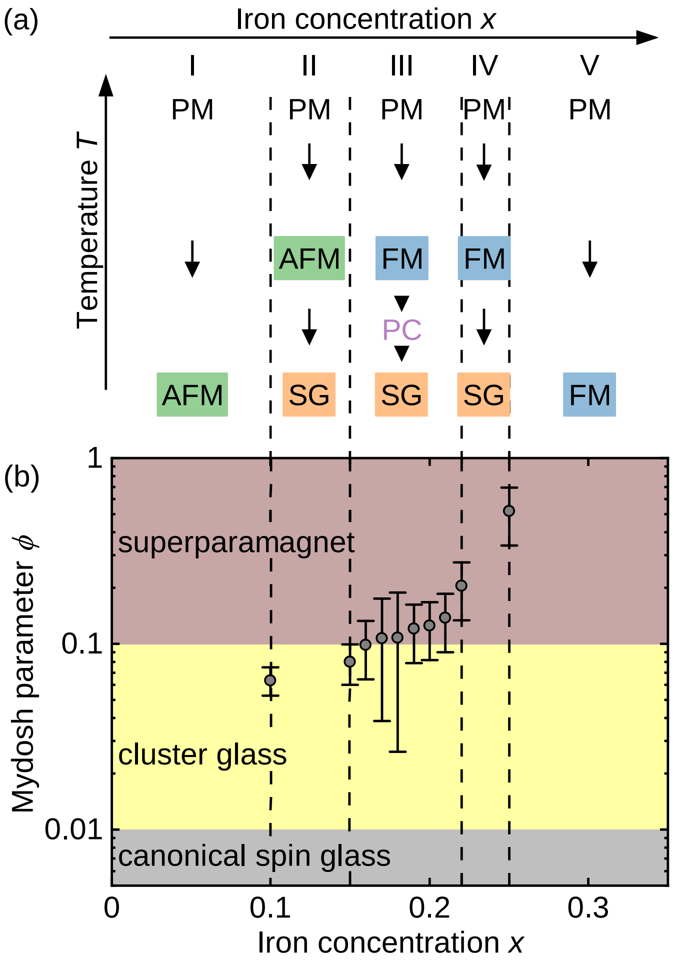

Figure 6.11: Evolution of the Mydosh-parameter in Fe_xCr_{1-x}. (a) Schematic depiction of the five different sequences of magnetic regimes observed as a function of temperature T and concentration x. The following regimes are distinguished: paramagnetic (PM), antiferromagnetic (AFM), ferromagnetic (FM), spin-glass (SG). A precursor phenomenon (PC) may be observed between FM and SG. (b) Mydosh parameter ϕ as a function of the iron concentration x, allowing to classify the spin-glass behavior as canonical ($\phi \leq 0.01$, gray shading), cluster-glass ($0.01 \leq \phi \leq 0.1$, yellow shading), or superparamagnetic ($\phi \geq 0.1$, brown shading).

6.4 Conclusions

Polycrystalline samples of $\mathrm{Fe}_x\mathrm{Cr}_{1-x}$ in the concentration range $0.05 \leq x \leq 0.30$ were investigated by means of ac susceptibility and magnetization, neutron depolarization, specific heat, and ac electrical transport measurements.

Under increasing Fe concentration a reduction followed by the disappearance of T_N at $x \approx 0.15$ is observed. In the vicinity of this concentration, a ferromagnetic transition emerges for $x \geq 0.15$ and T_C is increasing with increasing x. Furthermore, spin glass behaviour is observed in the range $0.10 \leq x \leq 0.25$ as identified by a frequency dependent cusp in the ac susceptibility and the splitting between zero-field cooled and high-field cooled branches of the magnetization and neutron depolarization. In addition indications for a precursor regime located between the antiferromagnetism, ferromagnetism, and the spin glass for concentrations $0.15 \leq x \leq 0.22$ are observed.

The zero-field concentration vs. temperature phase diagram, as inferred from the imaginary part of the ac susceptibility and the neutron depolarization, is in good agreement with previous reports [74–76]. Additionally our investigations indicate ferromagnetic behaviour for $0.15 \leq x \leq 0.19$, spin glass behaviour for $0.19 \leq x \leq 0.25$, and the precursor regime for $0.15 \leq x \leq 0.22$. The magnetization and ac susceptibility increase with increasing Fe content. The neutron depolarization displays broad ferromagnetic transitions and an additional drop at low temperatures indicating the spin glass freezing temperature T_g. Analysing the frequency dependence of the freezing temperature in the imaginary part of the ac susceptibility via the Mydosh paramter, a power law fit, and a Vogel-Fulcher approach reveals a change from cluster glass to superparamagnet and a strong intercluster correlation for all concentrations.

The results corroborate the picture proposed in the PhD thesis of Philipp Schmakat [77] that $\mathrm{Fe}_x\mathrm{Cr}_{1-x}$ alloys in the investigated range $0.10 \leq x \leq 0.25$ comprise of clusters of predominantly ferromagnetically coupled Fe spins in a background of single spins. With increasing Fe concentration, the Fe clusters increase in size. For concentrations of $0.05 \leq x \leq 0.15$ and temperatures in the range $T_\mathrm{g} < T < T_\mathrm{N}$, long-range antiferromagnetic order is present. When lowering the temperature towards T_g, the ferromagnetic coupling of the Fe spins becomes stronger. At T_g, the antiferromagnetic order is destroyed and the system freezes in a random configuration. Considering the evolution with temperature for $0.15 \leq x \leq 0.25$, for $T_\mathrm{g} < T < T_\mathrm{C}$, the Fe clusters form domains separated by fluctuating single spins. For $T < T_\mathrm{g}$, the coupling of the single spins with the clusters sets in, destroys the magnetic domains and the whole system freezes in a random state. For concentrations $x \geq 0.25$, around the percolation limit, long-range ferromagnetic order is stable down to the lowest temperatures.

CHAPTER 7

Summary and Outlook

The main results of this thesis are summarized as follows.

Chap. 3 covers the technical aspects, focussing on the preparation of high-purity intermetallic compounds and their characterization by x-ray diffraction as well as measurements of bulk and transport properties at low temperatures under high magnetic fields. The main technical accomplishment of this work concerned the setup and commissioning of the high-temperature high-pressure floating zone furnace, comprising multiple iterations of the sophisticated adjustment process and the growth of several test single crystals of various compounds. Finally, the optical configuration was adjusted such that large, high-quality single crystals of refractory compounds could be prepared, representing an important prerequisite for further exploration of exotic materials.

Chap. 4 reports the preparation and characterization of four ^{11}B-enriched single crystals of CrB_x with compositions $x = 1.90, 2.00, 2.05, 2.10$. The crystals were prepared with the optical floating zone technique in the high-pressure high-temperature optical floating zone furnace. X-ray Laue diffraction reveals one large single crystal with the expected hexagonal space group $P6/mmm$ in each float-zoned ingot. In the crystal with $x = 2.05$ a rotation of the crystal lattice by a few degrees along the growth direction is observed. For all concentrations, refined x-ray powder diffraction data indicate phase pure samples with lattice constants in agreement with the literature. The fact that the lattice dimensions are independent of the starting composition is attributed to the preparation with float-zoning, which promotes the crystallization of stoichiometric CrB_2. Measurements of the electrical resistivity and the specific heat are in agreement with the literature and indicate antiferromagnetic order.

Apart from the stoichiometric crystal with $x = 2.00$, samples from the beginning and the end of the single crystals show similar values of the RRR, pointing to a uniform crystalline quality. It is observed that samples with RRR $\gtrapprox 23$ display $T_{\mathrm{N}} \approx 88.5\,\mathrm{K}$, whereas samples with RRR ≈ 11 show $T_{\mathrm{N}} < 88.5\,\mathrm{K}$. The evolution of the RRR values as a function of the B portion x suggests that crystals with $x > 2.10$ might display even higher RRR values, potentially indicating a lowered amount of B vacancies. The reported work represents a basis for further studies concerning the diffuse scattering reported in stoichiometric $\mathrm{CrB_2}$ single crystals in the Ph.D. thesis of Alexander Regnat [25]. In particular, neutron diffraction experiments as well as the preparation of crystals with $x > 2.10$ in the near future will shed light on the relation between the starting composition and the distinct defect structure and superstructure as well as the influence of the starting composition on the magnetic structure of CrB_x.

Chap. 5 reports the preparation and investigation of a ^{11}B-enriched single crystal of $\mathrm{ErB_2}$ with the self-adjusted flux travelling solvent optical floating zone technique in the high-pressure high-temperature optical floating zone furnace. X-ray Laue and powder diffraction reveal a single crystal of high quality with the hexagonal space group $P6/mmm$ and lattice constants in good agreement with the literature.

Measurements of the ac susceptibility and magnetization indicate a transition to easy-plane antiferromagnetic order below a temperature of $T_{\mathrm{N}} = 13.9\,\mathrm{K}$, in agreement with the specific heat and electrical resistivity. The magnetization for field along the hard axis $\langle 001 \rangle$ displays a spin-flip transition in a field of $B_s = 11.8\,\mathrm{T}$ at $4\,\mathrm{K}$. The magnetization and ac susceptibility point to a strong anisotropy between the easy in-plane directions $\langle 100 \rangle$ and $\langle 210 \rangle$ and the hard out-of plane direction $\langle 001 \rangle$. This is corroborated by large effective magnetic moments in all three directions and indications for ferromagnetic and antiferromagnetic interactions in the easy plane and along the hard axis, respectively. Small ratios between the Weiss constants and the transition temperature point to a minor influence of geometric frustration.

Magnetic phase diagrams for field along $\langle 100 \rangle$ and $\langle 001 \rangle$ are inferred from the magnetization and ac susceptibility. For field along $\langle 100 \rangle$, four regimes may be distinguished: The paramagnetic region (PM) at high temperatures in small magnetic fields, the field-polarized region (FP) in high magnetic fields, the antiferromagnet (AFM) at low temperatures in small magnetic fields, and an unknown regime (X) separating the AFM from the FP at low temperatures. For fields along $\langle 001 \rangle$, four regimes may be distinguished: The paramagnetic region (PM) at high temperatures in small magnetic fields, the field-polarized region (FP) in high magnetic fields, the anisotropy-dominated region (AD) at temperatures below approximately 50 K and magnetic fields below approximately 12 T, and the antiferromagnetic state (AFM) at temperatures below 13.9 K and magnetic fields below approximately 12 T.

The temperature dependence of the specific heat shows a distinct lambda anomaly at $T_{\mathrm{N}} = 13.9\,\mathrm{K}$ clearly marking the transition to long-range order, in agreement with the magnetization and ac susceptibility. Measurements of the zero-field temperature dependence of the electrical resistivity show a distinct drop below a temperature of $13.9\,\mathrm{K}$, indicating T_{N} in agreement with the bulk data. Similar residual resistivity ratios $\mathrm{RRR}_{\langle 100 \rangle} = 6$ and $\mathrm{RRR}_{\langle 001 \rangle} = 5.5$ for the easy $\langle 100 \rangle$ and hard $\langle 001 \rangle$

direction, respectively, are extracted. For field along the easy axis ⟨100⟩, the Hall resistivity displays a characteristic shape reminiscent of the anomalous Hall effect. Moreover, indications for anisotropic fluctuations well-above T_N are observed in the bulk properties.

Taken together, the studies suggest that the magnetic structure of $\mathrm{ErB_2}$ is an easy-plane antiferromagnet, characterized by ferromagnetic order in the $\langle 100\rangle \times \langle 210\rangle$ planes, whereas alternating planes along the ⟨001⟩ direction are antiferromagnetically ordered. Future work will involve further measurements of the bulk properties over a broad temperature and magnetic field range, neutron scattering experiments to verify the proposed magnetic structure of $\mathrm{ErB_2}$, and the preparation and characterization of single crystals of the sibling rare-earth diborides $\mathrm{DyB_2}$ and $\mathrm{HoB_2}$.

Chap. 6 reports the investigation of polycrystalline samples of $\mathrm{Fe}_x\mathrm{Cr}_{1-x}$ in the concentration range $0.05 \leq x \leq 0.30$ by means of ac susceptibility, magnetization, neutron depolarization, specific heat, and electrical resistivity.

The zero-field concentration vs. temperature phase diagram, as inferred from the imaginary part of the ac susceptibility and the neutron depolarization, is in good agreement with previous reports [74–76]. The measurements indicate ferromagnetic behaviour for $0.15 \leq x \leq 0.19$, spin glass behaviour for $0.19 \leq x \leq 0.25$, and the emergence of a novel precursor regime for $0.15 \leq x \leq 0.22$, whose nature an origin remains to be clarified. With increasing Fe concentration, a decrease followed by the disappearance of T_N is observed at $x \approx 0.15$. In the vicinity of this concentration, a ferromagnetic transition emerges for $x \geq 0.15$ and T_C is increasing with increasing x. Furthermore, spin glass behaviour is observed in the range $0.10 \leq x \leq 0.25$ identified by a frequency dependent cusp in the ac susceptibility and the splitting between zero-field cooled and high-field cooled branches of the magnetization and neutron depolarization. Analysing the frequency dependence of the freezing temperature in the imaginary part of the ac susceptibility via the Mydosh parameter, a power law fit, and a Vogel-Fulcher approach reveals a change from cluster glass to superparamagnet and a strong intercluster correlation for all concentrations.

This study provides insight into the interplay of archetypical itinerant magnetism and complex spin glass behaviour, covering a putative quantum critical point, paving the way for understanding the fundamental relations between strong electronic correlations and disorder.

Publications

- **Interplay of itinerant magnetism and reentrant spin-glass behavior in $\mathbf{Fe}_x\mathbf{Cr}_{1-x}$**
  G. Benka, A. Bauer, P. Schmakat, S. Säubert, M. Seifert, P. Jorba, and C. Pfleiderer
  Submitted to Physical Review Materials
  arXiv:2007.10644 [cond-mat.str-el]

- **Determination of the hydrogen-bond network and the ferrimagnetic structure of a rockbridgeite-type compound $\mathbf{Fe^{2+}Fe^{3+}_{3.2}(Mn^{2+},Zn)_{0.8}(PO_4)_3(OH)_{4.2}(HOH)_{0.8}}$**
  B. Röska, S.-H. Park, D. Behal, K.-U. Hess, A. Günther, G. Benka, C. Pfleiderer, M. Hoelzel, and T. Kimura
  Journal of Physics: Condensed Matter **30**, 235401 (2018)

- **Neutron depolarization measurements of magnetite in chiton teeth**
  M. Seifert, M. Schulz, G. Benka, C. Pfleiderer, and S. Gilder
  Journal of Physics: Conference Series **862**, 012024 (2017)

- **Domain formation in the type-II/1 superconductor niobium: Interplay of pinning, geometry, and attractive vortex-vortex interaction**
  T. Reimann, M. Schulz, D. F. R. Mildner, M. Bleuel, A. Brûlet, R. P. Harti, G. Benka, A. Bauer, P. Böni, and S. Mühlbauer
  Physical Review B **96**, 144506 (2017)

- **The first study of antiferromagnetic eosphorite-childrenite series $\mathbf{(Mn_{1-x}Fe_x)AlP(OH)_2H_2O}$ (x=0.5)**
  D. Behal, B. Röska, S. H. Park, B. Pedersen, G. Benka, C. Pfleiderer, Y. Wakabayashi, and T. Kimura
  Journal of Magnetism and Magnetic Materials **428**, 17 (2017)

- **Low-temperature synthesis of $CuFeO_2$(delafossite) at 70°C: A new process solely by precipitation and ageing**
  M. John, S. Heuss-Aßbichler, S.-H. Park, A. Ullrich, G. Benka, N. Petersen, D. Rettenwander, and S. R. Horn
  Journal of Solid State Chemistry **233**, 390 (2016)

- **HT-solution growth and characterisation of $In_xNa_xMn_{1-2x}WO_4$ ($0<x\leq0.26$)**
  U. Gattermann, S. H. Park, C. Paulmann, G. Benka, and C. Pfleiderer
  Journal of Solid State Chemistry **244**, 140 (2016)

- **Magnetic properties of the In-doped $MnWO_4$-type solid solutions $Mn_{1-3x}In_{2x}\square_xWO_4$ [$\square$=vacancy; $0\leq x\leq0.11$]**
  U. Gattermann, G. Benka, A. Bauer, A. Senyshyn, and S. H. Park
  Journal of Magnetism and Magnetic Materials **398**, 167 (2016)

- **Ultra-high vacuum compatible induction-heated rod casting furnace**
  A. Bauer, A. Neubauer, W. Münzer, A. Regnat, G. Benka, M. Meven, B. Pedersen, and C. Pfleiderer
  Review of Scientific Instruments **87**, 063909 (2016)

- **Ultra-high vacuum compatible preparation chain for intermetallic compounds**
  A. Bauer, G. Benka, A. Regnat, C. Franz, and C. Pfleiderer
  Review of Scientific Instruments **87**, 113902 (2016)

- **Increasing the achievable state of order in Ni-based Heusler alloys via quenched-in vacancies**
  P. Neibecker, M. Leitner, G. Benka, and W. Petry
  Applied Physics Letters **105**, 261904 (2014)

Acknowledgements

"To see further, you must stand on the shoulders of a giant."

This section is dedicated to all who helped me along the road to a doctoral degree, be it directly or indirectly.

- I would like to start by expressing my gratitude towards my supervisor and Doktorvater, Christian Pfleiderer. Although I made my mistakes and experienced my ups and downs, you never let me down. With your supportive and charismatic character, your creative ideas and your talent to acquire funds, you manage to inspire your students and create a great scientific environment. I will miss those days.
- Next I would like to thank Andreas Bauer. Your comprehensive knowledge base and immense helpfulness, paired with manual skills and pragmatic approaches renders you a formidable experimentalist, teacher, and also friend. Thank you for always helping right away when asked and for your good humour and tasty cooking.
- The whole group at the chair E51 is definitely something special. In a typically nerdy environment such as physics, I count myself lucky to be or have been a member. In the sincere hope that I did not forget anyone, I would like to express my thankfulness to:
  - "Team Gisela": Andreas Bauer and Marc Wilde.
  - My current office mates: Andreas Wendl a.k.a. "Wendler", Franz X. Haslbeck a.k.a. "The Bavarian Gigolo", Christian Oberleitner a.k.a. "Seadawg", and Grace "Trouble-"Causer.
  - My former office mates: Felix Rucker, Christoph Schnarr, Stefan Giemsa, Jonas Kindervater, Patrick Ziegler and Steffen Säubert.
  - The Bachelor, Master and working students: Alexander Backs, Carolina Burger, Klaus Eibensteiner, Alexander Engelhardt, Leonhard Geilen, Maxi Horst, Nico Huber, Michelle Hollricher, Leo Maximov, Christian

    Oberleitner, Christoph Resch, Sebastian Schulte, Rudolf Schönmann, Christian Suttner, Anh Tong, Lukas Vogel, Lukas Worch, and Timur Yasko.
  - The Ph.D. candidates and post-doc researchers: Tim Adams, Alfonso Chacon, Christopher Duvinage, Christian Franz, Marco Halder, Pau Jorba, Markus Kleinhans, Denis Mettus, Alexander Regnat, Robert Ritz, Schorsch Sauther, Philipp Schmakat, Marc Seifert, Wolfgang Simeth, Jan P. Spallek, Michael Wagner, and Birgit Wiedemann.
  - The Secretaries: Martina Meven, Martina Michel, Astrid Mühlberg, and Lisa Seitz.

- The technicians Andi Mantwill and Stefan Giemsa, and the staff of the central workshop of the physics department Manfred Pfaller, Manfred Reiter, Gabriel Reingen, Lukas Winterhalter, and all the others who had the dubious honour to interpret my technical drawings and produce the parts.

- The Central crystal lab of the physics department: Andreas Erb, Katarzyna Danielewicz, Michael Stanger, Claudia Schweiger, and most notably Susi Mayr, for metric tons of oriented samples, whose preparation involved detailed small-scale tasks and requires a profound skills with the x-ray Laue diffraction camera.

- The colleagues from our sibling chair E21:
  - My special thanks to Peter Böni, for his relaxed Swiss resourcefulness and his spontaneous, extremely entertaining speeches at the Christmas party, all that from someone who does not like to give speeches, by his own account.
  - Stefan Giemsa, you are a special case. I obtained immense help from you in a large number of construction-related projects in the form of professional engineering approaches, great ideas, and acquisition of materials, as well as how to compile more or less proper technical drawings. Sadly, you did now want to get invited to our wedding, but I forgive you this one.
  - Henrik Gabold, for fancy "dripster" coffee, Jingfan Ye, Alexander Book, and Zarah Inanloo Maranloo.

- Andreas Schneider and Andreas Erb, with whom I had the honour of raiding II-VI in Newton Aycliffe. Loot was a as good as new optical floating zone furnace, christened with the name "Godzilla".

- Peter Gille, who kindly contributed his comprehensive knowledge of growing crystals with complex metallurgy and who provided his Bridgman furnaces "Romeo" and "Julia" to successfully prepare single crystals of metallurgically highly challenging Co-Zn-Mn compounds. Alas, this project is not reported here.

- Anatoliy Senyshyn and Volodymyr Baran, x-ray and neutron diffraction experts, both helped me immensely in recording, refining and interpreting diffraction data. In particular, they supervised our beamtime at SPODI on the (not reported) Co-Zn-Mn compounds.
- My collaborators Sohyun Park, Ulf Gattermann, David Behal, Melanie John, Beni Röska from the LMU and Pascal Neibecker from E12. Thank you for you professional, determined working attitude and plenty invigorating discussions.
- My dear friends: Ria Spallek, Albin Markwardt, and Wolfgang Wiedemann.
- My fellow students, who I met a long time ago at the beginning of my scientific journey: Marcel Brändlein, Tobias Simmet, Jan P. Spallek, Matthaeus Schwarz-Schilling, and Andreas Zeidler. Most of us manage to see each other regularly and I sincerely hope this continues for the years to come. I've had and keep on having the biggest fun and greatest times with you!
- The gym-bromance of my life: Marco Halder, supreme master of squat, deadlift, python coding, and dummschwätzing, as well as the brilliant Jan P. Spallek, successful business man, and gentleman of integrity.
- My whole family, in particular my mother Angelika, my father Rudolf, and my brother Christopher, a.k.a. Narph, for their unwavering and perennial support throughout the years.
- Finally, I want to express my eternal gratitude towards my wife, my dear Myrto.

M.V.M.

Bibliography

[1] E. Dagotto, Correlated electrons in high-temperature superconductors, Reviews of Modern Physics **66**, 763 (1994).

[2] L. F. Schneemeyer, J. V. Waszczak, T. Siegrist, R. B. van Dover, L. W. Rupp, B. Batlogg, R. J. Cava, and D. W. Murphy, Superconductivity in $YBa_2Cu_3O_7$ single crystals, Nature **328**, 601 (1987).

[3] C. Pfleiderer, Superconducting phases of f-electron compounds, Reviews of Modern Physics **81**, 1551 (2009).

[4] A. P. Mackenzie, R. K. W. Haselwimmer, A. W. Tyler, G. G. Lonzarich, Y. Mori, S. Nishizaki, and Y. Maeno, Extremely Strong Dependence of Superconductivity on Disorder in Sr_2RuO_4, Physical Review Letters **80**, 161 (1998).

[5] B. C. Sales, A. S. Sefat, M. A. McGuire, R. Y. Jin, D. Mandrus, and Y. Mozharivskyj, Bulk superconductivity at 14 K in single crystals of $Fe_{1+y}Te_xSe_{1-x}$, Physical Review B **79**, 094521 (2009).

[6] S. Sachdev, *Quantum Phase Transitions* (Cambridge University Press, 2011).

[7] Q. Si and F. Steglich, Heavy Fermions and Quantum Phase Transitions, Science **329**, 1161 (2010).

[8] P. Gegenwart, Q. Si, and F. Steglich, Quantum criticality in heavy-fermion metals, Nature Physics **4**, 186 (2008).

[9] A. J. Schofield, Non-Fermi liquids, Contemporary Physics **40**, 95 (1999).

[10] G. R. Stewart, Non-Fermi-liquid behavior in d- and f-electron metals, Reviews of Modern Physics **73**, 797 (2001).

[11] A. P. Ramirez, Strongly Geometrically Frustrated Magnets, Annual Review of Materials Science **24**, 453 (1994).

[12] L. Balents, Spin liquids in frustrated magnets, Nature **464**, 199 (2010).

[13] S. Mühlbauer, B. Binz, F. Jonietz, C. Pfleiderer, A. Rosch, A. Neubauer, R. Georgii, and P. Böni, Skyrmion Lattice in a Chiral Magnet, Science **323**, 915 (2009).

[14] X. Z. Yu, Y. Onose, N. Kanazawa, J. H. Park, J. H. Han, Y. Matsui, N. Nagaosa, and Y. Tokura, Real-space observation of a two-dimensional skyrmion crystal, Nature **465**, 901 (2010).

[15] X. Z. Yu, N. Kanazawa, Y. Onose, K. Kimoto, W. Z. Zhang, S. Ishiwata, Y. Matsui, and Y. Tokura, Near room-temperature formation of a skyrmion crystal in thin-films of the helimagnet FeGe, Nature Materials **10**, 106 (2011).

[16] S. Seki, X. Z. Yu, S. Ishiwata, and Y. Tokura, Observation of Skyrmions in a Multiferroic Material, Science **336**, 198 (2012).

[17] Y. Tokunaga, X. Z. Yu, J. S. White, H. M. Rønnow, D. Morikawa, Y. Taguchi, and Y. Tokura, A new class of chiral materials hosting magnetic skyrmions beyond room temperature, Nature Communications **6**, 7638 (2015).

[18] E. Dagotto, Complexity in Strongly Correlated Electronic Systems, Science **309**, 257 (2005).

[19] E. Morosan, D. Natelson, A. H. Nevidomskyy, and Q. Si, Strongly Correlated Materials, Advanced Materials **24**, 4896 (2012).

[20] R. S. Perry, L. M. Galvin, S. A. Grigera, L. Capogna, A. J. Schofield, A. P. Mackenzie, M. Chiao, S. R. Julian, S. I. Ikeda, S. Nakatsuji, Y. Maeno, and C. Pfleiderer, Metamagnetism and Critical Fluctuations in High Quality Single Crystals of the Bilayer Ruthenate $Sr_3R_2O_7$, Physical Review Letters **86**, 2661 (2001).

[21] S. Seo, X. Lu, J.-X. Zhu, R. R. Urbano, N. Curro, E. D. Bauer, V. A. Sidorov, L. D. Pham, T. Park, Z. Fisk, and J. D. Thompson, Disorder in quantum critical superconductors, Nature Physics **10**, 120 (2014).

[22] T. I. Sigfusson, N. R. Bernhoeft, and G. G. Lonzarich, The de Haas-van Alphen effect, exchange splitting and Curie temperature in the weak itinerant ferromagnetic Ni_3Al, Journal of Physics F: Metal Physics **14**, 2141 (1984).

[23] B. Fåk, C. Vettier, J. Flouquet, F. Bourdarot, S. Raymond, A. Vernière, P. Lejay, P. Boutrouille, N. R. Bernhoeft, S. T. Bramwell, R. A. Fisher, and N. E. Phillips, Influence of sample quality on the magnetic properties of URU_2Si_2, Journal of Magnetism and Magnetic Materials **154**, 339 (1996).

[24] A. Bauer, *Investigation of Itinerant Antiferromagnets and Cubic Chiral Helimagnets*, Ph.D. thesis, Technische Universität München, Physik Department (2014).

[25] A. Regnat, *Low-Temperature Properties and Magnetic Structure of CrB_2, MnB_2, and CuMnSb*, Ph.D. thesis, Technische Universität München, Physik Department (2019).

[26] K. H. J. Buschow, Magnetic Properties of Borides, in *Boron and Refractory Borides*, edited by V. I. Matkovich (Springer Berlin Heidelberg, 1977) p. 494.

[27] J. Castaing and P. Costa, Properties and Uses of Diborides, in *Boron and Refractory Borides*, edited by V. I. Matkovich (Springer Berlin Heidelberg, 1977) p. 390.

[28] W. Gordon and S. B. Soffer, A galvanomagnetic investigation of TiB_2, NbB_2 and ZrB_2, Journal of Physics and Chemistry of Solids **36**, 627 (1975).

[29] J. Nagamatsu, N. Nakagawa, T. Muranaka, Y. Zenitani, and J. Akimitsu, Superconductivity at 39 K in magnesium diboride, Nature **410**, 63 (2001).

[30] G. R. Barnes and R. B. Creel, Chromium-like antiferromagnetic behavior of CrB_2, Physics Letters A **29**, 203 (1969).

[31] A. Bauer, A. Regnat, C. G. F. Blum, S. Gottlieb-Schönmeyer, B. Pedersen, M. Meven, S. Wurmehl, J. Kuneš, and C. Pfleiderer, Low-temperature properties of single-crystal CrB_2, Physical Review B **90**, 064414 (2014).

[32] M. A. Avila, S. L. Bud'ko, C. Petrovic, R. A. Ribeiro, P. C. Canfield, A. V. Tsvyashchenko, and L. N. Fomicheva, Synthesis and properties of YbB_2, Journal of Alloys and Compounds **358**, 56 (2003).

[33] M. Kasaya and T. Hihara, Magnetic Structure of MnB_2, Journal of the Physical Society of Japan **29**, 336 (1970).

[34] G. Will and W. Schafer, Neutron diffraction and the magnetic structures of some rare earth diborides and tetraborides, Journal of the Less Common Metals **67**, 31 (1979).

[35] V. V. Novikov and A. V. Matovnikov, Low-temperature heat capacity and magnetic phase transition of TbB_2, Inorganic Materials **44**, 134 (2008).

[36] V. V. Novikov and A. V. Matovnikov, Low-temperature heat capacity of dysprosium diboride, Journal of Thermal Analysis and Calorimetry **88**, 597 (2007).

[37] T. Mori, T. Takimoto, A. Leithe-Jasper, R. Cardoso-Gil, W. Schnelle, G. Auffermann, H. Rosner, and Y. Grin, Ferromagnetism and electronic structure of TmB_2, Physical Review B **79**, 104418 (2009).

[38] V. A. Gasparov, N. S. Sidorov, I. I. Zver'kova, and M. P. Kulakov, Electron transport in diborides: Observation of superconductivity in ZrB_2, Journal of Experimental and Theoretical Physics Letters **73**, 532 (2001).

[39] H. Takeya, A. Matsumoto, K. Hirata, Y. S. Sung, and K. Togano, Superconducting phase in niobium diborides prepared by combustion synthesis, Physica C: Superconductivity **412-414**, 111 (2004).

[40] J. Castaing, P. Costa, M. Heritier, and P. Lederer, Spin fluctuation effects in nearly antiferromagnetic vanadium and chromium diborides, Journal of Physics and Chemistry of Solids **33**, 533 (1972).

[41] D. M. Broun, What lies beneath the dome? Nature Physics **4**, 170 (2008).

[42] H. Okamoto, *Desk Handbook: Phase Diagrams for Binary Alloys* (ASM International, 2010).

[43] S. H. Liu, L. Kopp, W. B. England, and H. W. Myron, Energy bands, electronic properties, and magnetic ordering of CrB_2, Physical Review B **11**, 3463 (1975).

[44] D. R. Armstrong, The electronic structure of the first-row transition-metal diborides, Theoretica chimica acta **64**, 137 (1983).

[45] P. Vajeeston, P. Ravindran, C. Ravi, and R. Asokamani, Electronic structure, bonding, and ground-state properties of AlB_2-type transition-metal diborides, Physical Review B **63**, 045115 (2001).

[46] A. V. Fedorchenko, G. E. Grechnev, A. S. Panfilov, A. V. Logosha, I. V. Svechkarev, V. B. Filippov, A. B. Lyashchenko, and A. V. Evdokimova, Anisotropy of the magnetic properties and the electronic structure of transition-metal diborides, Low Temperature Physics **35**, 862 (2009).

[47] M. Brasse, L. Chioncel, J. Kuneš, A. Bauer, A. Regnat, C. G. F. Blum, S. Wurmehl, C. Pfleiderer, M. A. Wilde, and D. Grundler, De Haas-van Alphen effect and Fermi surface properties of single-crystal CrB_2, Physical Review B **88**, 155138 (2013).

[48] M. C. Cadeville, Proprietes magnetiques des diborures de manganese et de chrome: MnB_2 et CrB_2, Journal of Physics and Chemistry of Solids **27**, 667 (1966).

[49] Y. Kitaoka, H. Yasuoka, T. Tanaka, and Y. Ishizawa, Nuclear magnetic resonance of ^{11}B in CrB_2, Solid State Communications **26**, 87 (1978).

[50] Y. Kitaoka and H. Yasuoka, NMR Investigations on the Spin Fluctuations in Itinerant Antiferromagnets III. CrB_2, Journal of the Physical Society of Japan **49**, 493 (1980).

[51] J. Castaing, R. Caudron, G. Toupance, and P. Costa, Electronic structure of transition metal diborides, Solid State Communications **7**, 1453 (1969).

[52] Y. Nishihara, M. Tokumoto, Y. Yamaguchi, and S. Ogawa, Magneto-Volume Effect of the Interant-Electron Antiferromagnet CrB_2, Journal of the Physical Society of Japan **56**, 1562 (1987).

[53] C. N. Guy, The electronic properties of chromium borides, Journal of Physics and Chemistry of Solids **37**, 1005 (1976).

[54] T. Tanaka, H. Nozaki, E. Bannai, Y. Ishizawa, S. Kawai, and T. Yamane, Preparation and properties of CrB_2 single crystals, Journal of the Less Common Metals **50**, 15 (1976).

[55] G. Balakrishnan, S. Majumdar, M. R. Lees, and D. M. Paul, Single crystal growth of CrB_2 using a high-temperature image furnace, Journal of Crystal Growth **274**, 294 (2005).

[56] G. Grechnev, A. Fedorchenko, A. Logosha, A. Panfilov, I. Svechkarev, V. Filippov, A. Lyashchenko, and A. Evdokimova, Electronic structure and magnetic properties of transition metal diborides, Journal of Alloys and Compounds **481**, 75 (2009).

[57] J. Castaing, J. Danan, and M. Rieux, Calorimetric and resistive investigation of the magnetic properties of CrB2, Solid State Communications **10**, 563 (1972).

[58] C. Michioka, Y. Itoh, K. Yoshimura, Y. Watabe, Y. Kousaka, H. Ichikawa, and J. Akimitsu, NMR studies of single crystal chromium diboride, Journal of Magnetism and Magnetic Materials **310**, e620 (2007).

[59] S. Funahashi, Y. Hamaguchi, T. Tanaka, and E. Bannai, Helical magnetic structure in CrB_2, Solid State Communications **23**, 859 (1977).

[60] E. Kaya, Y. Kousaka, K. Kakurai, M. Takeda, and J. Akimitsu, Spherical neutron polarimetry studies on the magnetic structure of single crystal $Cr_{1-x}Mo_xB_2$ (x=0, 0.15), Physica B: Condensed Matter **404**, 2524 (2009).

[61] P. A. Sharma, N. Hur, Y. Horibe, C. H. Chen, B. G. Kim, S. Guha, M. Z. Cieplak, and S.-W. Cheong, Percolative Superconductivity in $Mg_{1-x}B_2$, Physical Review Letters **89**, 167003 (2002).

[62] G. Venturini, I. Ijjaali, and B. Malaman, Vacancy ordering in AlB_2-type RGe_{2-x} compounds (R=Y, Nd, Sm, Gd–Lu), Journal of Alloys and Compounds **284**, 262 (1999).

[63] E. S. Penev, S. Bhowmick, A. Sadrzadeh, and B. I. Yakobson, Polymorphism of Two-Dimensional Boron, Nano Letters **12**, 2441 (2012).

[64] M. Dahlqvist, U. Jansson, and J. Rosen, Influence of boron vacancies on phase stability, bonding and structure of MB_2 (M = Ti, Zr, Hf, V, Nb, Ta, Cr, Mo, W) with AlB_2 type structure, Journal of Physics: Condensed Matter **27**, 435702 (2015).

[65] J. Etourneau and P. Hagenmuller, Structure and physical features of the rare-earth borides, Philosophical Magazine B **52**, 589 (1985).

[66] A. V. Matovnikov, V. S. Urbanovich, T. A. Chukina, A. A. Sidorov, and V. V. Novikov, Two-step syntheses of rare-earth diborides, Inorganic Materials **45**, 366 (2009).

[67] V. V. Novikov, T. A. Chukina, and A. A. Verevkin, Anomalies in thermal expansion of rare-earth diborides in the temperature range of magnetic phase transformations, Physics of the Solid State **52**, 364 (2010).

[68] V. Novikov and T. Chukina, Anomalies of thermal expansion and change of entropy of rare-earth diborides at the temperatures of magnetic transitions, physica status solidi (b) **248**, 136 (2011).

[69] J. B. Kargin, C. R. S. Haines, M. J. Coak, C. Liu, A. V. Matovnikov, V. V. Novikov, A. N. Vasiliev, and S. S. Saxena, Low Temperature Resistivity of the Rare Earth Diborides (Er, Ho, Tm)B_2, in *2nd International Multidisciplinary Microscopy and Microanalysis Congress*, edited by E. Polychroniadis, A. Y. Oral, and M. Ozer (Springer International Publishing, 2015) p. 183.

[70] R. N. Castellano, Crystal growth of TmB_2 and ErB_2, Materials Research Bulletin **7**, 261 (1972).

[71] E. Fawcett, Spin-density-wave antiferromagnetism in chromium, Reviews of Modern Physics **60**, 209 (1988).

[72] E. Fawcett, H. L. Alberts, V. Y. Galkin, D. R. Noakes, and J. V. Yakhmi, Spin-density-wave antiferromagnetism in chromium alloys, Reviews of Modern Physics **66**, 25 (1994).

[73] H. v. Löhneysen, A. Rosch, M. Vojta, and P. Wölfle, Fermi-liquid instabilities at magnetic quantum phase transitions, Reviews of Modern Physics **79**, 1015 (2007).

[74] S. K. Burke and B. D. Rainford, The evolution of magnetic order in CrFe alloys. I. Antiferromagnetic alloys close to the critical concentration, Journal of Physics F: Metal Physics **13**, 441 (1983).

[75] S. K. Burke, R. Cywinski, J. R. Davis, and B. D. Rainford, The evolution of magnetic order in CrFe alloys. II. Onset of ferromagnetism, Journal of Physics F: Metal Physics **13**, 451 (1983).

[76] S. K. Burke and B. D. Rainford, The evolution of magnetic order in CrFe alloys. III. Ferromagnetism close to the critical concentration, Journal of Physics F: Metal Physics **13**, 471 (1983).

[77] P. Schmakat, *Neutron Depolarisation Measurements of Ferromagnetic Quantum Phase Transitions & Wavelength-Frame Multiplication Chopper System for the Imaging Instrument ODIN at the ESS*, Ph.D. thesis, Technische Universität München, Physik Department (2015).

[78] Y. Ishikawa, S. Hoshino, and Y. Endoh, Antiferromagnetism in Dilute Iron Chromium Alloys, Journal of the Physical Society of Japan **22**, 1221 (1967).

[79] B. Babic, F. Kajzar, and G. Parette, Magnetic properties and magnetic interactions in chromium-rich Cr-Fe alloys, Journal of Physics and Chemistry of Solids **41**, 1303 (1980).

[80] S. K. Burke and B. D. Rainford, Determination of the antiferromagnetic phase boundary in Cr-Fe alloys, Journal of Physics F: Metal Physics **8**, L239 (1978).

[81] T. Suzuki, Magnetic Phase Transition of Chromium-Rich Chromium-Iron Alloys, Journal of the Physical Society of Japan **41**, 1187 (1976).

[82] M. V. Nevitt and A. T. Aldred, Ferromagnetism in V-Fe and Cr-Fe Alloys, Journal of Applied Physics **34**, 463 (1963).

[83] B. Loegel, Magnetic transitions in the chromium-iron system, Journal of Physics F: Metal Physics **5**, 497 (1975).

[84] C. R. Fincher, S. M. Shapiro, A. H. Palumbo, and R. D. Parks, Spin-Wave Evolution Crossing from the Ferromagnetic to Spin-Glass Regime of $\mathrm{Fe}_x\mathrm{Cr}_{1-x}$, Physical Review Letters **45**, 474 (1980).

[85] S. M. Shapiro, C. R. Fincher, A. C. Palumbo, and R. D. Parks, Anomalous spin-wave behavior in the magnetic alloy $\mathrm{Fe}_x\mathrm{Cr}_{1-x}$, Physical Review B **24**, 6661 (1981).

[86] J. O. Strom-Olsen, D. F. Wilford, S. K. Burke, and B. D. Rainford, The coexistence of spin density wave ordering and spin glass ordering in chromium alloys containing iron, Journal of Physics F: Metal Physics **9**, L95 (1979).

[87] V. Cannella and J. A. Mydosh, Magnetic Ordering in Gold-Iron Alloys, Physical Review B **6**, 4220 (1972).

[88] R. D. Shull, H. Okamoto, and P. A. Beck, Transition from ferromagnetism to mictomagnetism in Fe—Al alloys, Solid State Communications **20**, 863 (1976).

[89] R. D. Shull and P. A. Beck, Mictomagnetic to ferromagnetic transition in Cr-Fe alloys, AIP Conference Proceedings **24**, 95 (1975).

[90] S. Säubert, *Experimental Studies of Ultraslow Magnetisation Dynamics*, Ph.D. thesis, Technische Universität München, Physik Department (2018).

[91] K. Motoya, S. M. Shapiro, and Y. Muraoka, Neutron scattering studies of the anomalous magnetic alloy $Fe_{0.7}Al_{0.3}$, Physical Review B **28**, 6183 (1983).

[92] D. L. Stein and C. M. Newman, *Spin Glasses and Complexity* (Princeton University Press, 2013).

[93] J. A. Mydosh, *Spin Glasses: An Experimental Introduction* (CRC Press, 1993).

[94] P. J. Ford, Spin glasses, Contemporary Physics **23**, 141 (1982).

[95] J. A. Mydosh, Spin glasses: Redux: An updated experimental/materials survey, Reports on Progress in Physics **78**, 052501 (2015).

[96] A. P. Murani, G. Goeltz, and K. Ibel, Evidence for freezing of spins in binary alloys, Solid State Communications **19**, 733 (1976).

[97] B. Martínez, X. Obradors, L. Balcells, A. Rouanet, and C. Monty, Low Temperature Surface Spin-Glass Transition in γ- Fe_2O_3, Physical Review Letters **80**, 181 (1998).

[98] T. Zhu, B. G. Shen, J. R. Sun, H. W. Zhao, and W. S. Zhan, Surface spin-glass behavior in $La_{2/3}Sr_{1/3}MnO_3$ nanoparticles, Applied Physics Letters **78**, 3863 (2001).

[99] S. Süllow, G. J. Nieuwenhuys, A. A. Menovsky, J. A. Mydosh, S. A. M. Mentink, T. E. Mason, and W. J. L. Buyers, Spin Glass Behavior in URh_2Ge_2, Physical Review Letters **78**, 354 (1997).

[100] J. G. Soldevilla, J. C. G. Sal, J. A. Blanco, J. I. Espeso, and J. R. Fernández, Phase diagram of the $CeNi_{1-x}Cu_x$ Kondo system with spin-glass-like behavior favored by hybridization, Physical Review B **61**, 6821 (2000).

[101] J. Dho, W. S. Kim, and N. H. Hur, Reentrant Spin Glass Behavior in Cr-Doped Perovskite Manganite, Physical Review Letters **89**, 027202 (2002).

[102] J. N. Reimers, J. R. Dahn, J. E. Greedan, C. V. Stager, G. Liu, I. Davidson, and U. Von Sacken, Spin Glass Behavior in the Frustrated Antiferromagnetic $LiNiO_2$, Journal of Solid State Chemistry **102**, 542 (1993).

[103] H. Maletta and W. Felsch, Insulating spin-glass system $Eu_xSr_{1-x}S$, Physical Review B **20**, 1245 (1979).

[104] M. Ishii and M. Kobayashi, Single crystals for radiation detectors, Progress in Crystal Growth and Characterization of Materials **23**, 245 (1992).

[105] J. S. Neal, N. C. Giles, X. Yang, R. A. Wall, K. B. Ucer, R. T. Williams, D. J. Wisniewski, L. A. Boatner, V. Rengarajan, J. Nause, and B. Nemeth, Evaluation of Melt-Grown, ZnO Single Crystals for Use as Alpha-Particle Detectors, IEEE Transactions on Nuclear Science **55**, 1397 (2008).

[106] A. A. Kaminskii, *Laser Crystals: Their Physics and Properties*, Vol. 14 (Springer, 2013).

[107] X.-L. Qi and S.-C. Zhang, Topological insulators and superconductors, Reviews of Modern Physics **83**, 1057 (2011).

[108] Y. L. Chen, J. G. Analytis, J.-H. Chu, Z. K. Liu, S.-K. Mo, X. Qi, L., H. J. Zhang, D. H. Lu, X. Dai, Z. Fang, S. C. Zhang, I. R. Fisher, Z. Hussain, and Z.-X. Shen, Experimental Realization of a Three-Dimensional Topological Insulator, Bi_2Te_3, Science **325**, 178 (2009).

[109] J. Bohm, K.-T. Wilke, P. Görnert, M. Jurisch, and M. Ritschel, *Kristallzüchtung* (J. A. Barth, Leipzig, 1993).

[110] C. E. Campbell and U. R. Kattner, Assessment of the Cr-B system and extrapolation to the Ni-Al-Cr-B quaternary system, Calphad **26**, 477 (2002).

[111] G. Dhanaraj, K. Byrappa, V. Prasad, and M. Dudley, eds., *Springer Handbook of Crystal Growth* (Springer-Verlag, 2010).

[112] P. Rudolph, 8 - Floating Zone Growth of Oxides and Metallic Alloys, in *Handbook of Crystal Growth (Second Edition)* (Elsevier, 2015) p. 281.

[113] H. A. Dabkowska and A. B. Dabkowski, Crystal Growth of Oxides by Optical Floating Zone Technique, in *Springer Handbook of Crystal Growth*, edited by G. Dhanaraj, K. Byrappa, V. Prasad, and M. Dudley (Springer Berlin Heidelberg, 2010) p. 367.

[114] G. A. Wolff and A. I. Mlavsky, Travelling Solvent Techniques, in *Crystal Growth: Theory and Techniques Volume 1*, edited by C. H. L. Goodman (Springer US, 1974) p. 193.

[115] A. Neubauer, *Single Crystal Growth of Intermetallic Compounds with Unusual Low Temperature Properties*, Ph.D. thesis, Technische Universität München, Physik Department (2010).

[116] W. Münzer, *Einkristallzüchtung Und Magnetische Eigenschaften von MnSi Und* $Fe_{1-x}Co_xSi$, Diploma thesis, Technische Universität München, Physik Department (2008).

[117] G. Benka, *UHV-Compatible Arc Melting Furnace and Annealing Oven for Materials with Exotic Electronic Properties*, M.Sc. thesis, Technische Universität München, Physik Department (2013).

[118] A. Bauer, G. Benka, A. Regnat, C. Franz, and C. Pfleiderer, Ultra-high vacuum compatible preparation chain for intermetallic compounds, Review of Scientific Instruments **87**, 113902 (2016).

[119] A. Bauer, A. Neubauer, W. Münzer, A. Regnat, G. Benka, M. Meven, B. Pedersen, and C. Pfleiderer, Ultra-high vacuum compatible induction-heated rod casting furnace, Review of Scientific Instruments **87**, 063909 (2016).

[120] D. Souptel, W. Löser, and G. Behr, Vertical optical floating zone furnace: Principles of irradiation profile formation, Journal of Crystal Growth **300**, 538 (2007).

[121] M. Palme, S. Riehemann, A. Horst, D. Souptel, and G. Behr, *Optische Simulation Einer Strahlungsheizung*, Annual Report (Fraunhofer IOF, 2004).

[122] A. Guinier, La diffraction des rayons X aux très petits angles : Application à l'étude de phénomènes ultramicroscopiques, Annales de Physique **11**, 161 (1939).

[123] M. Mendenhall, Powder Diffraction SRMs, https://www.nist.gov/programs-projects/powder-diffraction-srms (2016).

[124] A. A. Coelho, TOPAS and TOPAS-Academic: An optimization program integrating computer algebra and crystallographic objects written in C++, Journal of Applied Crystallography **51**, 210 (2018).

[125] Inorganic Crystal Structure Database: General Information, http://www2.fiz-karlsruhe.de/icsd_general_information.html (2019).

[126] B. H. Toby, R factors in Rietveld analysis: How good is good enough? Powder Diffraction **21**, 67 (2006).

[127] Quantum Design Application Note: Palladium Reference Samples ,https://www.qdusa.com/sitedocs/appNotes/mpms/1041-001.pdf, (2016).

[128] D.-X. Chen, V. Skumryev, and B. Bozzo, Calibration of ac and dc magnetometers with a Dy_2O_3 standard, Review of Scientific Instruments **82**, 045112 (2011).

[129] M. Halder, *Thermodynamic and Kinetic Stability of Magnetic Skyrmions*, Ph.D. thesis, Technische Universität München, Physik Department (2018).

[130] P. K. Liao, K. E. Spear, and M. E. Schlesinger, The B-Er (boron-erbium) system, Journal of Phase Equilibria **17**, 326 (1996).

[131] A. Bauer and C. Pfleiderer, Generic Aspects of Skyrmion Lattices in Chiral Magnets, in *Topological Structures in Ferroic Materials: Domain Walls, Vortices and Skyrmions* (Springer International Publishing, 2016).

[132] A. Aharoni, Demagnetizing factors for rectangular ferromagnetic prisms, Journal of Applied Physics **83**, 3432 (1998).

[133] J. Jensen and A. R. Mackintosh, ELEMENTS OF RARE EARTH MAGNETISM, in *Rare Earth Magnetism: Structures and Excitations* (Clarendon Press, 1991).

[134] N. Nagaosa, J. Sinova, S. Onoda, A. H. MacDonald, and N. P. Ong, Anomalous Hall effect, Reviews of Modern Physics **82**, 1539 (2010).

[135] M. Schulz and B. Schillinger, ANTARES: Cold neutron radiography and tomography facility, Journal of large-scale research facilities JLSRF **1**, 17 (2015).

[136] M. Seifert, M. Schulz, G. Benka, C. Pfleiderer, and S. Gilder, Neutron depolarization measurements of magnetite in chiton teeth, Journal of Physics: Conference Series **862**, 012024 (2017).

[137] P. Jorba, M. Schulz, D. S. Hussey, M. Abir, M. Seifert, V. Tsurkan, A. Loidl, C. Pfleiderer, and B. Khaykovich, High-resolution neutron depolarization microscopy of the ferromagnetic transitions in Ni3Al and HgCr2Se4 under pressure, Journal of Magnetism and Magnetic Materials **475**, 176 (2019).

[138] J. D. Jackson, *Classical Electrodynamics*, 3rd ed. (Wiley, 1998).

[139] S. Samarappuli, A. Schilling, M. A. Chernikov, H. R. Ott, and T. Wolf, Comparative study of AC susceptibility and resistivity of a superconducting $YBa_2Cu_3O_7$ single crystal in a magnetic field, Physica C: Superconductivity **201**, 159 (1992).

[140] O. Halpern and T. Holstein, On the Passage of Neutrons Through Ferromagnets, Physical Review **59**, 960 (1941).

[141] W. J. de Haas, J. de Boer, and G. J. van dën Berg, The electrical resistance of gold, copper and lead at low temperatures, Physica **1**, 1115 (1934).

[142] J. Kondo, Resistance Minimum in Dilute Magnetic Alloys, Progress of Theoretical Physics **32**, 37 (1964).

[143] C. L. Lin, A. Wallash, J. E. Crow, T. Mihalisin, and P. Schlottmann, Heavy-fermion behavior and the single-ion Kondo model, Physical Review Letters **58**, 1232 (1987).

[144] A. P. Pikul, U. Stockert, A. Steppke, T. Cichorek, S. Hartmann, N. Caroca-Canales, N. Oeschler, M. Brando, C. Geibel, and F. Steglich, Single-Ion Kondo Scaling of the Coherent Fermi Liquid Regime in $\mathrm{ce}_{1-x}\mathrm{la}_x\mathrm{ni}_2\mathrm{ge}_2$, Physical Review Letters **108**, 066405 (2012).

[145] S. Arajs and G. R. Dunmyre, Electrical Resistivity of Chromium-Rich Chromium-Iron Alloys between 4° and 320°K, Journal of Applied Physics **37**, 1017 (1966).

[146] J. L. Tholence, On the frequency dependence of the transition temperature in spin glasses, Solid State Communications **35**, 113 (1980).

[147] K. Binder and A. P. Young, Spin glasses: Experimental facts, theoretical concepts, and open questions, Reviews of Modern Physics **58**, 801 (1986).

[148] P. C. Hohenberg and B. I. Halperin, Theory of dynamic critical phenomena, Reviews of Modern Physics **49**, 435 (1977).

[149] J. Souletie and J. L. Tholence, Critical slowing down in spin glasses and other glasses: Fulcher versus power law, Physical Review B **32**, 516 (1985).

[150] G. S. Fulcher, Analysis of Recent Measurements of the Viscosity of Glasses, Journal of the American Ceramic Society **8**, 339 (1925).

[151] E. Svanidze and E. Morosan, Cluster-glass behavior induced by local moment doping in the itinerant ferromagnet $Sc_{3.1}In$, Physical Review B **88**, 064412 (2013).

[152] V. K. Anand, D. T. Adroja, and A. D. Hillier, Ferromagnetic cluster spin-glass behavior in $PrRhSn_3$, Physical Review B **85**, 014418 (2012).

[153] Y. Li, Q. Cheng, D.-W. Qi, J.-L. Wang, J. Zhang, S. Wang, and J. Guan, Effects of Fe doping on ac susceptibility of $Pr_{0.75}Na_{0.25}MnO_3$, Chinese Physics B **20**, 117502 (2011).